

University of Alabama in Huntsville

LOUIS

Dissertations

UAH Electronic Theses and Dissertations

2024

A new, intuitive method for the design and analysis of multi-pass cavities

Adam S. Mansor

Follow this and additional works at: <https://louis.uah.edu/uah-dissertations>

Recommended Citation

Mansor, Adam S., "A new, intuitive method for the design and analysis of multi-pass cavities" (2024).
Dissertations. 406.

<https://louis.uah.edu/uah-dissertations/406>

This Dissertation is brought to you for free and open access by the UAH Electronic Theses and Dissertations at LOUIS. It has been accepted for inclusion in Dissertations by an authorized administrator of LOUIS.

**A NEW, INTUITIVE METHOD FOR THE DESIGN AND ANALYSIS OF
MULTI-PASS CAVITIES**

Adam S Mansor

A DISSERTATION

**Submitted in partial fulfillment of the requirements
for the degree of Doctor of Philosophy
in
Optical Science and Engineering Program
to
The Graduate School
of
The University of Alabama in Huntsville
May 2024**

Approved by:

Dr. Patrick J. Reardon, Research Advisor and Committee Chair
Dr. Hongrok Chang, Committee Member
Dr. Lingze Duan, Committee Member
Dr. James Hadaway, Committee Member
Dr. Robert Lindquist, Committee Member
Dr. Don A Gregory, Department Chair
Dr. Jon Hakkila, College Dean
Dr. Jon Hakkila, Graduate Dean

Abstract

A NEW, INTUITIVE METHOD FOR THE DESIGN AND ANALYSIS OF MULTI-PASS CAVITIES

Adam S Mansor

**A dissertation submitted in partial fulfillment of the requirements
for the degree of Doctor of Philosophy**

Optical Science and Engineering Program

**The University of Alabama in Huntsville
May 2024**

This dissertation develops a new analytical approach for designing and analyzing multi-pass cavities like the Herriott cell by employing the graphical $y\bar{y}$ diagram approach. The new technique can be deployed in spectroscopy absorption detection, femtoseconds laser cavities, or any off-axis spherical mirror interferometers applications. Such a system can be uniquely designed and evaluated by entering a few parameters that define the required physics for the cell, the packaging size limits for the system and the probe beam size, plus two user selected parameters. The existing design method, developed by Herriott, is discussed and then the $y\bar{y}$ diagram method is presented and applied, showing several design solutions that meet the spectroscopic absorption system requirements. The adaptability of the $y\bar{y}$ diagram approach is then shown, presenting several design solutions with mirrors of arbitrary curvatures and a new approach of rapid calculations of 3rd order astigmatism, the dominant aberration in these systems. This dissertation also employs the $y\bar{y}$ diagram of Gaussian beams to illustrate detailed design parameters of a gas spectrometer sensor and develops an enhanced Gaussian beam decomposition technique that could be used for physical optics and diffraction analysis for this system or any other optical system.

Acknowledgements

I would like to thank my parents for their prayers and support throughout my studies. I also would like to thank my advisor Dr. Patrick J. Reardon for providing his guidance and expertise in developing this dissertation. I truly enjoyed our discussions of theory and problem solving throughout this process. A special thanks to the members of my committee and the center for applied optics members as well for ensuring a high quality of work. I have respect for and have learned much valuable information from each of them.

I must also thank Dr. Don Gregory and Dr. James Miller for allowing me to work and study at the Physics Department and Astronomy.

Table of Contents

Abstract	ii
Acknowledgements	iv
Table of Contents	v
List of Figures	vii
List of Tables	xi
List of Symbols	xiii
Chapter 1. Introduction	1
Chapter 2.	5
2.1 Gaussian Beam Theory	5
2.2 The $y\bar{y}$ Techniques of Paraxial Optics	6
2.3 Paraxial $y\bar{y}$ Diagram Characterizations	7
2.4 The $y\bar{y}$ Techniques of Gaussian Beam (Complex Ray Tracing)	9
Chapter 3.	11
3.1 Simulation of Diffraction Using the Huygens-Fresnel Technique	11
3.2 Gaussian Beam Decomposition Method.....	13
Chapter 4.	15
4.1 Modeling the Diffraction Pattern of Square Aperture by Overlap Factor 1.5 and FFT Using the IMP and TSF	15
4.2 Hybrid Overlap Factor Configuration.....	19
Chapter 5.	23
5.1 Introduction.....	23
5.2 Herriott Cell Background and Design Analysis.....	23
5.3 The Multi-Passes Consecutive Re-entrant Condition.....	28
5.4 The Interlaced Re-entrant Condition	34
5.5 Step by Step of Designing Absorbance Herriott's MPC	39
5.6 Using Ray Tracing Software (Zemax) to Analyze the Herriot Cell	43
5.7 Using the (xn, yn) Values as $y\bar{y}$ Values to Design First Order Herriott Cell	50
Chapter 6.	53

6.1	The MPC $y\bar{y}$ Diagram Methodology Introduction.....	53
6.2	Defining MPC Absorbance Parameters	55
6.3	The $y\bar{y}$ Diagram Methodology of Gut Ray with Numerical Example.....	57
6.4	Consecutive $y\bar{y}$ Diagram Gut Ray Design of MPC Absorbance Spectrometer.....	58
6.5	Interlaced $y\bar{y}$ Diagram Gut Ray Design of MPC	62
6.6	Invalid $y\bar{y}$ Diagram Gut Ray Design of MPC.....	65
6.7	Uneven and Unstable Intercepts for $y\bar{y}$ Diagram Gut Ray Design of MPC	69
6.8	Collimated Injected Beam $y\bar{y}$ Diagram Design of MPC	71
6.8.1	Collimated Input Beam Consecutive $y\bar{y}$ Diagram Design of MPC	74
6.8.2	Collimated Input Beam Interlaced $y\bar{y}$ Diagram Design of MPC.....	79
6.8.3	Collimated Input Beam Invalid $y\bar{y}$ Diagram Design of MPC	83
6.9	Designing a MPC with Two Different Mirror Radii of Curvatures.....	88
6.9.1	Concave-Concave $y\bar{y}$ Diagram Design with Different Radii of Curvatures of MPC Design	88
6.9.2	Concave-Plano $y\bar{y}$ Diagram Design with Different Radii of Curvatures of MPC Design	93
6.9.3	Concave-convex $y\bar{y}$ Diagram Design with different Radii of Curvatures of MPC Design	97
Chapter 7.	103
7.1	MPC off-Axis Astigmatism Aberration Background	103
7.2	Off-Axis MPC Seidel and Zernike Polynomials Astigmatism Aberration Background.....	106
7.3	Off-Axis MPC Astigmatism Aberration using $y\bar{y}$ Diagram Calculation.....	108
Chapter 8.	118
8.1	Summary and Conclusions	118
8.2	Future Work	119
References	121
Appendix A.	125
Appendix B.	128
Appendix C.	133
Appendix D.	134
Appendix E.	137

List of Figures

Figure 2.1 Laser Gaussian beam layout	5
Figure 2.2 $y\bar{y}$ Diagram of a simple optical System for gut ray	7
Figure 2.3 $y\bar{y}$ Diagram of a simple positive and negative optical system for collimated ray	8
Figure 2.4 Layout of complex ray tracing for Gaussian laser beam propagation.	9
Figure 3.1 Sommerfeld geometry for normal incident collimated source and Observation planes	11
Figure 3.2 Column (a) normalized 3D irradiance at $Z=0$ showing ripples and roll off slope, column (b) normalized field magnitude cross section at $Z=0$ and column (c) $1/e^2$ map radii of 11X11 beamlets	14
Figure 4.1 (a) comparison of irradiance, magnitude and phase (b) a base-10 logarithmic scale of the irradiance and magnitude	16
Figure 4.2 (a) comparison of irradiance, magnitude and phase among TSF, IMP and GBD, respectively for 20x20 mm square aperture with 15X15 beamlets and row (b) a base-10 logarithmic scale on the irradiance and magnitude of TSF, IMP and GBD respectively for 20x20 mm square aperture with 15X15 beamlets.	17
Figure 4.3 (a) normalized 3D field irradiance showing ripples and roll off slope, column (b) normalized field magnitude cross section and column (c) $1/e^2$ map radii of 11x11 beamlets.	20
Figure 4.4 (a) comparison of irradiance between HGB, GBD17x17 and GBD respectively (b) comparison of magnitude, between HGBD and GBD respectively.	21
Figure 4.5 (a) comparison of irradiance between HGB, GBD17x17 and GBD respectively (b) comparison of magnitude, between HGBD and GBD17X17, GBD respectively.	22

Figure 5.1 A schematic of a Herriot type multi-pass cavities MPCs	25
Figure 5.2 A round trip through the multi-pass cavities (MPCs)	25
Figure 5.3 Consecutive confocal cavity and correspond (xn, yn) diagram plot.	29
Figure 5.4 Consecutive focal cavity and correspond (xn, yn) diagram $2\mu=6$ plot.	30
Figure 5.5 Consecutive multi-pass cavity and correspond (xn, yn) diagram plot.	31
Figure 5.6 Distinctive interlaced confocal cavity and correspond (xn, yn) diagram plot.....	35
Figure 5.7 Distinctive interlaced focal cavity and correspond (xn, yn) $2\nu =6$ and $\mu=5$ plot....	36
Figure 5.8 Interlaced multi-pass cavity and correspond (xn, yn) diagram plot.....	37
Figure 5.9 Layout of front and back mirrors beam bounces.....	42
Figure 5.10 Layout of combined front and back mirrors beam bounces.	42
Figure 5.11 (a) Layout of gut ray Herriot cell design in Zemax (b) merit function (c) lens data editor (d) Zemax real ray tracing, FOV and EPD	45
Figure 5.12 (a) Layout of Herriot collimated input design in Zemax (b) merit function (c) lens data editor (d) Paraxial real ray tracing, FOV and EPD	48
Figure 5.13 An image of rotated gut ray real solution to be matched with the Zemax collimated design.	48
Figure 5.14 Shows the Rotation of the gut ray (green) to facilitate the collimated ray (orange). 49	
Figure 5.15 (a) The $y\bar{y}$ diagram of collimated input design, (b) The $y\bar{y}$ diagram of gut ray design	49
Figure 6.1 a) Correct size of mirror semi-diameter for absorbance spectrometer Mirror b) Undersized mirror semi-diameter for absorbance spectrometer.....	56
Figure 6.2 Consecutive gut ray $y\bar{y}$ diagram MPC.....	60
Figure 6.3 Consecutive gut ray $y\bar{y}$ diagram MPC intercepts on M1, M2.....	61

Figure 6.4 Interlaced gut ray $y\bar{y}$ diagram MPC.	62
Figure 6.5 Interlaced gut ray $y\bar{y}$ diagram MPC intercepts on M1, M2.....	64
Figure 6.6 Invalid gut ray $y\bar{y}$ diagram MPC.	67
Figure 6.7 Invalid gut ray $y\bar{y}$ diagram MPC intercepts on M1, M2.	68
Figure 6.8 Uneven distribution gut ray $y\bar{y}$ diagram MPC.....	69
Figure 6.9 Invalid gut ray $y\bar{y}$ diagram MPC intercepts on M1, M2.	70
Figure 6.10 Unstable gut ray $y\bar{y}$ diagram MPC.	71
Figure 6.11 Consecutive collimated input $y\bar{y}$ diagram MPC.....	76
Figure 6.12 Consecutive collimated Input $y\bar{y}$ Diagram MPC intercepts M1, M2 plot.....	77
Figure 6.13 Consecutive collimated input ray tracing simulation	78
Figure 6.14 An image of consecutive collimated input ray tracing simulation data	78
Figure 6.15 Interlace collimated input $y\bar{y}$ diagram MPC.....	79
Figure 6.16 Interlace Collimated input $y\bar{y}$ diagram MPC intercepts M1, M2.	81
Figure 6.17 Interlace Collimated input ray tracing simulation	82
Figure 6.18 An image of interlaced collimated input ray tracing simulation data	82
Figure 6.19 Invalid collimated input $y\bar{y}$ diagram MPC.	84
Figure 6.20 Invalid collimated input $y\bar{y}$ diagram MPC intercepts M1, M2.....	86
Figure 6.21 Invalid Collimated input ray tracing simulation.....	86
Figure 6.22 An image of invalid collimated input ray tracing simulation data	87
Figure 6.23 Concave-concave interlace $y\bar{y}$ diagram MPC plot.	89
Figure 6.24 Interlace concave-concave $y\bar{y}$ diagram MPC intercepts M1, M2.	91
Figure 6.25 Concave-concave ray tracing simulation	92
Figure 6.26 An image of concave-concave ray tracing simulation data	92

Figure 6.27 Concave-concave interlace $y\bar{y}$ diagram MPC plot.	95
Figure 6.28 Interlace concave-plano $y\bar{y}$ diagram MPC intercepts M1, M2.....	96
Figure 6.29 Concave-plano ray tracing simulation	96
Figure 6.30 An image of concave-Plano ray tracing simulation data	97
Figure 6.31 Concave-convex ray tracing simulation.	99
Figure 6.32 Interlace concave-convex $y\bar{y}$ diagram MPC intercepts M1, M2.....	100
Figure 6.33 Concave-convex ray tracing simulation	101
Figure 6.34 An image of concave-convex ray tracing simulation data.	101
Figure 7.1 a) Spot diagram b) Wavefront function c) Wavefront map of Zemax design	104
Figure 7.2 Astigmatism 3-D plot and corresponding spot diagram [6] [40] [41]......	105
Figure 7.3 Astigmatism 3-D plot using Seidel W222 for circular exit pupil aperture.....	107
Figure 7.4 Column (a) Rotated Field of view (b) symmetric field of view magnitude (c) decomposition of W222.....	110
Figure 7.5 Z5 comparison between calculated Zernike's coefficients and ray tracing data.....	115
Figure 7.6 Z6 comparison between calculated Zernike's coefficients and ray tracing data.....	115
Figure 7.7 RSS comparison between calculated Zernike's coefficients and ray tracing data. ..	116

List of Tables

Table 2.1 The paraxial properties of an optical system represented by the $y\bar{y}$ diagram.	8
Table 2.2 The properties of the complex ray tracing of Gaussian beam.....	10
Table 5.1 Consecutive Confocal cavity passes (a) (x_n, y_n) values (b) design parameters.....	29
Table 5.2 Consecutive focal cavity passes (a) (x_n, y_n) values (b) design parameters.	30
Table 5.3 Consecutive multi-pass cavity passes (a) (x_n, y_n) values (b) design parameters	32
Table 5.4 Comparison among three different cavities.	33
Table 5.5 Interlaced Confocal passes (a) correspond (x_n, y_n) (b) design parameters values...	35
Table 5.6 Distinctive interlaced focal passes (a) correspond (x_n, y_n) (b) design parameters values.	36
Table 5.7 Interlaced multi-passes cavity 32 (a) corresponded (x_n, y_n) values (b) design parameters.	38
Table 5.8 Comparison among three different interlaced cavities.....	39
Table 5.9 The displacement beam coordinates on front and back mirrors, respectively.	40
Table 5.10 Description of first order design of Herriot cell.....	41
Table 5.11 Deploy the displacement (x_n, y_n) values as initial $y\bar{y}$ value description.....	51
Table 5.12 Results of deploy the displacement values as initial $y\bar{y}$ values.....	52
Table 6.1 Description of First Order Consecutive gut ray $y\bar{y}$ Diagram MPC.....	59
Table 6.2 Consecutive gut ray $y\bar{y}$ diagram MPC.	61
Table 6.3 Description of first order Interlaced gut ray $y\bar{y}$ diagram MPC.	63
Table 6.4 Interlaced gut ray $y\bar{y}$ diagram MPC Design.....	64
Table 6.5 Description of first order Interlaced gut ray $y\bar{y}$ diagram MPC.	66
Table 6.6 Invalid gut ray $y\bar{y}$ diagram MPC design.	68

Table 8.7 Description of first order consecutive collimated ray $y\bar{y}$ diagram MPC.	75
Table 6.8 Consecutive collimated Input $y\bar{y}$ Diagram MPC intercepts M1, M2 data.	77
Table 6.9 Description of first order interlaced collimated ray $y\bar{y}$ diagram MPC.....	80
Table 6.10 Interlace collimated input $y\bar{y}$ diagram MPC design.....	81
Table 6.11 Description of first order invalid collimated ray $y\bar{y}$ diagram MPC.	83
Table 6.12 Invalid collimated interlaced $y\bar{y}$ diagram MPC design.....	85
Table 6.13 Four different solutions of collimated MPCs using the $y\bar{y}$ diagram.	87
Table 6.14 Description of first order interlaced concave-concave $y\bar{y}$ diagram MPC.....	90
Table 6.15 Concave-concave interlaced $y\bar{y}$ diagram MPC design data.	91
Table 6.16 Description of first order interlaced concave-plano $y\bar{y}$ diagram MPC.	94
Table 6.17 Concave-plano interlaced $y\bar{y}$ diagram MPC design.....	95
Table 6.18 Description of first order interlaced concave-plano $y\bar{y}$ diagram MPC.	98
Table 6.19 Concave-convex interlaced $y\bar{y}$ diagram MPC design.	100
Table 6.20 Four different designs of gut ray MPCs including ROCs and FOVs using the $y\bar{y}$ diagram.	102
Table 7.1 Description of first order step-by-step Zernike’s coefficient calculation for the first bounce on M2.	111
Table 7.2 Step-by- step Z5 and Z6 calculation.	113
Table 7.3 Comparison between calculated Zernike’s coefficients and ray tracing data.	114
Table 7.4 Comparison between calculated Zernike’s coefficients for m1,3 and 5.	117

List of Symbols

Symbols	Description
GBD	Gaussian beam decomposition
HGBD	Hybrid Gaussian beam decomposition
HCMPCs	Herriott multi-pass cavities
MTF	Modulation transfer function
FFT	Fast Fourier transform
OF	Overlap factor
\mathcal{F}	Fourier transformer
\mathcal{F}^{-1}	Inverse Fourier transformer
$H(x, y)$	The transfer function (TSF)
$h(x, y)$	The impulse response (IMP)
$U_2(x, y; Z)$	Gaussian Laser Beam electric field
$R(Z)$	Gaussian Laser beam Radius of curvature
Z_R	Gaussian Laser beam Rayleigh range
Θ	Gaussian Laser beam divergence angle
$I(x, y; Z)$	Irradiance
ω_0	Gaussian Laser beam waist
λ	Wavelength
K	Wave number
L_g	LaGrange invariant
$U_1(\xi, \eta)$	Source plan

$U_2(x, y)$	Observation plan
FOV	Field of view
Z	Optical propagation distance in z-direction
EPD	Zemax entrance pupil diameter operand
EFFL	Zemax effective focal length operand
EFLY	Zemax element focal length operand
LINV	Zemax LaGrange invariant operand
EXPP	Zemax exit pupil diameter operand
EXPD	Zemax exit pupil diameter operand
MPCs	Multi-pass cavities
OAL	Overall length of absorbance MPC
D	Laser beam probe beam diameter
ROC	Radius of curvature
ROCs	Radii of curvatures
g_1 & g_2	Stability parameters of MPC
ν	Number of passes in MPC
N	Number of intercepts on the mirrors
S/N	Signal to noise ratio
θ_m	Angle between two for consecutive bounces
α	Constant value
β	Constant value
x'_0	Input beam slope in x-direction
A	Maximum x-semi-diameters of beam bounces on the mirrors

B	Maximum y-semi-diameters of beam bounces on the mirrors
x'_0	Input beam slope in y-direction
K_m	K- parameter- the number of rotations around axis
m	The number of rotations around axis
h	Object height
h'	Image height
Φ	Geometrical optical power(diopter)
Φ_{OB}	Oblique optical Power
W_{222}	Seidel wavefront coefficient
ρ	Radial normalized coordinate
θ_c	Counterclockwise angle between two sequences intercept
EPD_g	Gut ray entrance pupil diameter
EPD_r	Rotated design entrance pupil diameter
XPD_g	Gut ray design exit pupil diameter
XPD_r	Rotated design exit pupil diameter
A_s	Seidel chief ray incidence angle
B_s	Seidel marginal ray incidence angle
Z5	Sagittal Zernike's coefficient
Z6	Tangential Zernike's coefficients
AOI	Angle of incident
RSS	Root sum square
Φ_z	Measured counterclockwise angle from the local x axis

Chapter 1. Introduction

This research was initially conceived to provide an intuitive and rapid approach for the design and analysis of multi-pass cavities such as a Herriott cell. A Herriott cell is a two concave mirrors optical system where the optical path bounces back and forth multiple times between the two mirrors before exiting the cell. These have been used as resonant cells for interferometer or laser cavities [1] and, more commonly now, in spectroscopy as a method of providing a long path length in a short optical package [2]. The design of these systems has been based on a method first published by J. R. Pierce [3], which is a paraxial based method for electron beam systems. Once designed, analyzing and adjusting these systems can be readily performed using geometrical optics approaches, however, the beams propagating through them are generally small beams, sometimes small gaussian laser beams. The geometrical analysis is therefore incomplete, especially when one desires to analyze the beam after arbitrary numbers of reflections through the cavity. Thus, this dissertation research effort not only will provide a better means of designing, understanding and analyzing the performance of these systems, but also will provide a rapid way for designing multi-pass cavities (MPC) with different radii of curvatures. Additionally, a modified physical optics approach is being developed that can be used for the intracavity beam analysis of Herriott cells, for any optical system or for any optical beam propagation calculations. Lastly, a novel approach to calculate the third order aberrations of Astigmatism, the dominant aberration in these cells, is provided.

Methods for the design and analysis of optical systems have undergone huge advances over the centuries [4] [5] [6] [7] [8]. From an analytical perspective, these advances include the development of paraxial optics, then aberration theories such as Seidel's 3rd order methods and then integrating advances in the understanding and derivations of physical optics methods which enabled computation of the true diffraction-based performance of these systems as well as understanding of fundamental light propagation. As digital computers advanced, this enabled real ray tracing of effectively limitless numbers of rays and calculation of highly complex diffraction problems. Today, lens design and analysis programs on standard computers are able to trace 100's of millions of ray-surfaces per second and compute and display 2048x2048 FFT-based monochromatic diffraction patterns, point spread functions, in a few seconds.

However, there are still challenges at the most basic level for optical design and analysis, including setting up the initial optical design (first order design). One method for simplifying the process of designing the optical system was presented by Delano [9], the y \bar{y} diagram, which enables a highly graphical and intuitive means for laying out the optical design based on paraxial optics. This method was extended to enable the tracing of gaussian beams throughout an optical system, thus coupling the method to physical optics calculations.

For physical optics modeling, Huygens-Fresnel and Fraunhofer methods of propagation calculation using numerical Fourier transform methods are applied extensively in physical optics modeling of many situations including coronagraph analysis, laser beam propagation, digital holography, interferometry and modeling of the diffraction patterns of many optical components and systems [10] [11] [12]. Most software simulation packages use these fast Fourier transform (FFT)-based methods to model the physical optics including interference and diffraction. Employing these diffraction algorithm calculations can dramatically increase the computation time

for different applications. For example, optimizing or tolerancing of an optical system using modulation transfer function (MTF) or encircled energy criteria can be 1000x slower than ray tracing calculations. However, this method is often the approach of choice since it applies to a broad range of propagation scenarios and is relatively straightforward, although, it has constraints for calculating the sampling regimes correctly which, if not followed, could lead to erroneous artifacts and when followed can require intractably large and long calculations. Another common challenge is calculating long-range large beam propagation by using FFT based methods. The constraints of sampling can conflict with reasonable execution times of the algorithm; avoiding computational aliasing can require prohibitively massive data arrays which limit the processing to large, specialized computer systems.

An alternative method to FFT-based diffraction calculations is Gaussian beamlet decomposition (GBD) [8] [12] [13] [14] [15] [16] [17] [18] [19] [20] [21] [22]. Waves, truncated by any aperture, are represented by a set of Gaussian beamlets with appropriate amplitude, radii beam waist and constant phase, which can then be linearly added at any plane of interest. There are, of course, parameters that impact the accuracy of the model. Since a field is being represented by an array of Gaussian beamlets, there can be undesired ripples in the fit and edge rounding at what should be sharp cutoffs. How much the adjacent Gaussian beamlets overlap and the total number of Gaussian beamlets employed drive these errors.

The research dissertation will couple some of these elements to provide a simple and graphically intuitive method for designing and analyzing multi-pass cavity cells. In this research dissertation, these individual components will be described more fully and then their proposed coupling will be discussed.

Chapter 2 will present the necessary details and our nomenclature for Gaussian beams, the $y\bar{y}$ techniques for paraxial and complex ray tracing of Gaussian beam optics [23] [24]. Chapter 3 will present the Gaussian Beam decomposition (GBD) method and current FFT-based approaches for calculating beam propagation focusing on the diffraction of a square aperture as it contains two conflicting challenges: a smooth field amplitude and a sharp edge. In this Chapter 4 we have developed a modification of GBD or hybrid Gaussian beam decomposition (HGBD) and comparison of GBD and HGBD is also presented. The HGBD method with results that show its effectiveness. Chapter 5 is a detailed discussion of the Herriott cell background, including the current method of design that is employed to the Orion space capsule. The research dissertation author and Dr. Patrick Reardon were involved in the analysis, redesign, fabrication and testing of a Herriott cell-based multi-Pass Cavity (MPC) system for measuring the O₂, CO₂ and H₂O levels aboard the Orion space capsule [25] [26] [27] [28] [29]. The design provided to the authors was created following the methods published by Pierce and extended by Herriott [1] [3].

The Chapter 6 then goes through the process of we've initially developed to find a method by which one can design a Herriott cell in the $y\bar{y}$ diagram framework, for gut ray, collimated input beam and different radii of curvatures. Chapter 7 presents a novel approach for numerical calculation of dominate 3rd order aberration in MPC "Astigmatism". Finally, Chapter 8 discusses the future work.

Chapter 2.

2.1 Gaussian Beam Theory

Gaussian beams have long been used and defined in optics as they are the fundamental mode of a cylindrical laser cavity [30] and they are one of the special case of functions that do not alter their amplitude profile as they propagate, although their phase does change. As Gaussian beams propagate, diffraction causes the Gaussian beamlets to broaden and diverge. The properties of a Gaussian beam field are listed below [31]. Equation 2.1 and 2.2 are the field and intensity of a single Gaussian beam. Equations 2.3 and 2.4 are the beam semi-diameter and field radius of curvature, while Equations 2.5 and 2.6 define the Rayleigh range and divergence angle, parameters used primarily to simplify the previous equations.

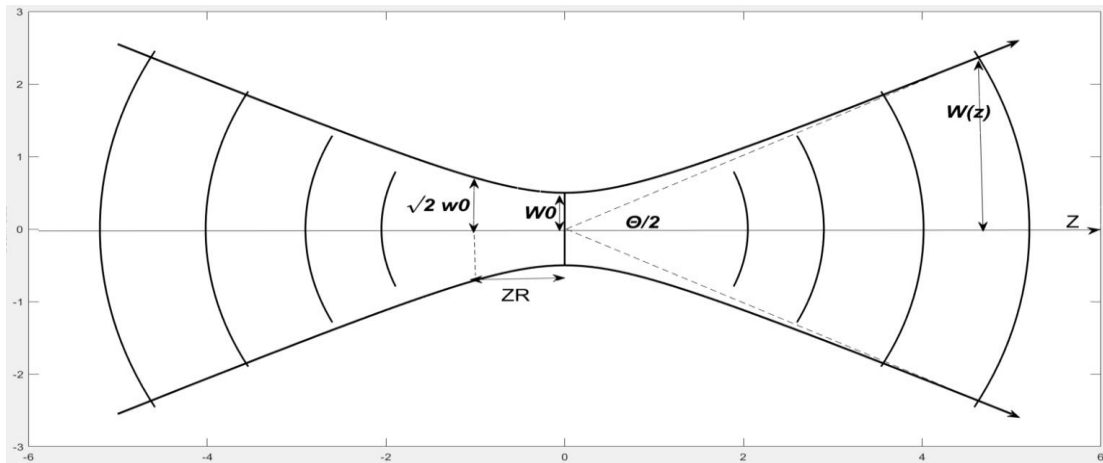


Figure 2.1 Laser Gaussian beam layout [31].

$$U_2(x,y;Z) = A \frac{\omega_0}{W(Z)} e^{-i[(KZ - \tan^{-1}(\frac{Z}{Z_R})] e^{ik(x^2+y^2)/2R(Z)} e^{-(x^2+y^2)/W(Z)} , \quad (2.1)$$

$$I(x,y;Z) = |U_2(x,y;Z)|^2 , \quad (2.2)$$

$$W(Z) = \omega_0 \sqrt{1 + \frac{Z^2}{Z_R^2}} , \quad (2.3)$$

$$R(Z) = Z + \frac{Z_R^2}{Z} , \quad (2.4)$$

$$Z_R = \frac{\pi \omega_0^2}{\lambda} , \quad (2.5)$$

$$\Theta = \frac{\lambda}{\pi \omega_0} . \quad (2.6)$$

We denote Z , k , $\tan^{-1}(\frac{Z}{Z_R})$ and A as the axial propagation distance from the beam waist, the wave number, the Gouy phase and the electric field amplitude respectively. From the paraxial wave solution, there is one restriction [31] on ω_0 , namely $\omega_0 > \lambda$.

2.2 The $y\bar{y}$ Techniques of Paraxial Optics

The $y\bar{y}$ diagram is a representation of geometrical paraxial optics, developed by Delano [9]. It proceeds by plotting the paraxial chief and marginal ray heights at each surface as they are sequentially encountered through the optical system. The marginal ray passes through the center of the object and its images, where $y=0$ and it clips the edge of the stop and the stop's images. The paraxial chief ray starts at the edge of the object and passes through the center of the stop where $\bar{y}=0$ and the stop's images. A simple $y\bar{y}$ diagram layout for single lens is illustrated in Fig2.2 a $y\bar{y}$ diagram requires the LaGrange Invariant of the system to be properly scaled.

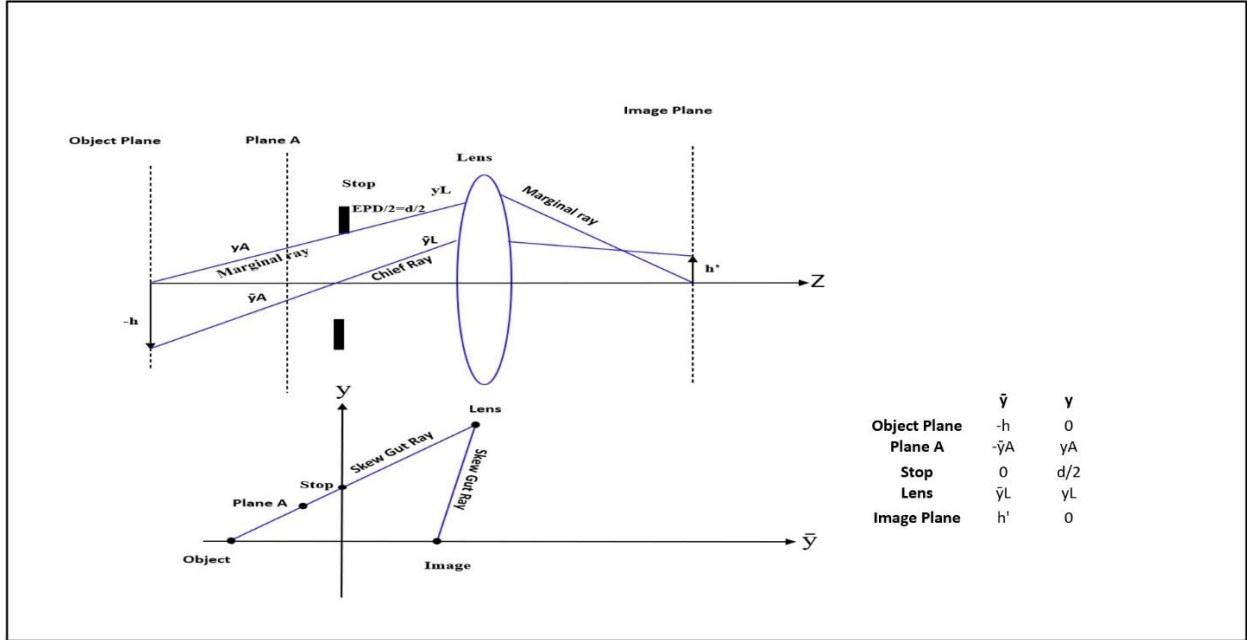


Figure 2.2 \bar{y} Diagram of a simple optical System for gut ray [24].

2.3 Paraxial \bar{y} Diagram Characterizations

The \bar{y} diagram requires scaling factor or LaGrange invariant (L_g) to keep the linearity of paraxial optics calculation between the heights and angles. In case of positive geometrical optical power, (Φ) such as concave mirrors, convex lenses the \bar{y} segment bends toward the origin, but, for negative geometrical optical power such as convex mirrors and concave lenses the \bar{y} segment bends away from the original. Alternately, flat optics such as plano mirrors reflect the \bar{y} segment without any bending. Collimated input ray or infinite conjugate input \bar{y} diagram is presented by parallel segment to \bar{y} axis, where $(\bar{y}, y) = (0, y)$ as illustrated in Fig2.3, consequently, skew input ray or finite conjugate input \bar{y} diagram is presented as by-passing segment to \bar{y} axis, where $(\bar{y}, y) = (\bar{y}, 0)$ as illustrated in Fig2.2.

The \bar{y} LaGrange invariant typically has positive sign when moving clockwise around the origin and negative sign when moving counterclockwise. The distance between two points is

related to the area swept out by a vector whose base is at the origin, from each sequential optical element. All real and virtual images and pupil can be specified by y and \bar{y} axis crossing. Some properties of the $y\bar{y}$ techniques of paraxial optics are listed in table 2.1.

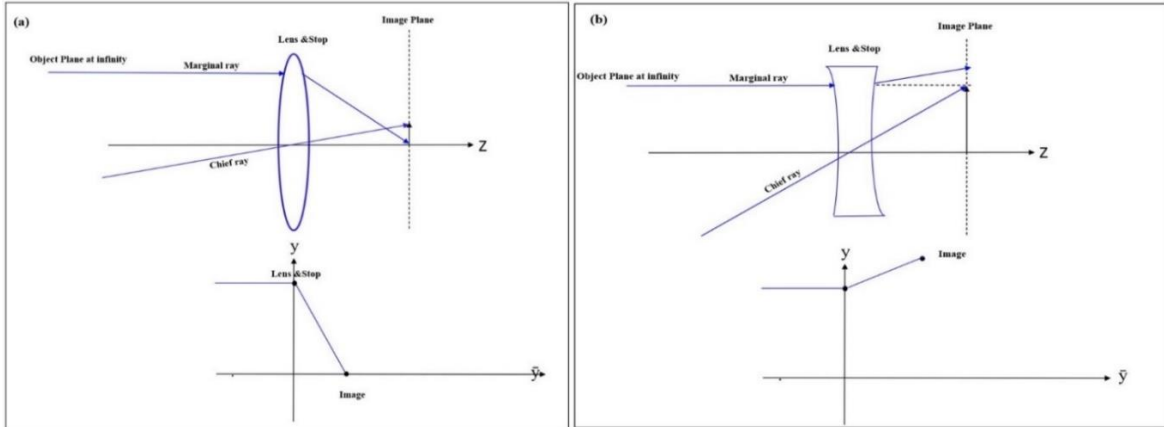


Figure 2.3 $y\bar{y}$ Diagram of a simple positive and negative optical system for collimated ray [32].

Table 2.1 The paraxial properties of an optical system represented by the $y\bar{y}$ diagram.

Properties	Brief description
$Lg = yn\bar{u} - \bar{y}nu$	LaGrange invariant or the scaling factor
$t1 = \frac{1}{Lg} \begin{bmatrix} y0 & \bar{y}0 \\ yl & \bar{y}l \end{bmatrix}$	Axial distance between locations represented by two points in the $y\bar{y}$ diagram
$\Phi = \frac{1}{Lg} \begin{bmatrix} u0 & \bar{u}0 \\ ul & \bar{u}l \end{bmatrix}$	Optical power at a bend on the $y\bar{y}$ diagram
$\bar{U} = \frac{\bar{y}i+1 - \bar{y}i}{t1}$	Chief ray angle after element 1 with the optical surface
$U = \frac{yi+1 - yi}{t1}$	Marginal ray angle after element 1 with the optical surface
$\bar{U} = \frac{Lg}{\bar{y}n}$	Chief ray angle when $y = 0$
$U = \frac{-Lg}{yn}$	Marginal ray angle when $\bar{y} = 0$

2.4 The $y\bar{y}$ Techniques of Gaussian Beam (Complex Ray Tracing)

Kessler and Shack first presented the $y\bar{y}$ method of laser beam propagation [24]. A simple explanation for their development is to consider that two rays can represent a Gaussian beam, as divergence ray and a waist ray, as shown in Fig .2.4.

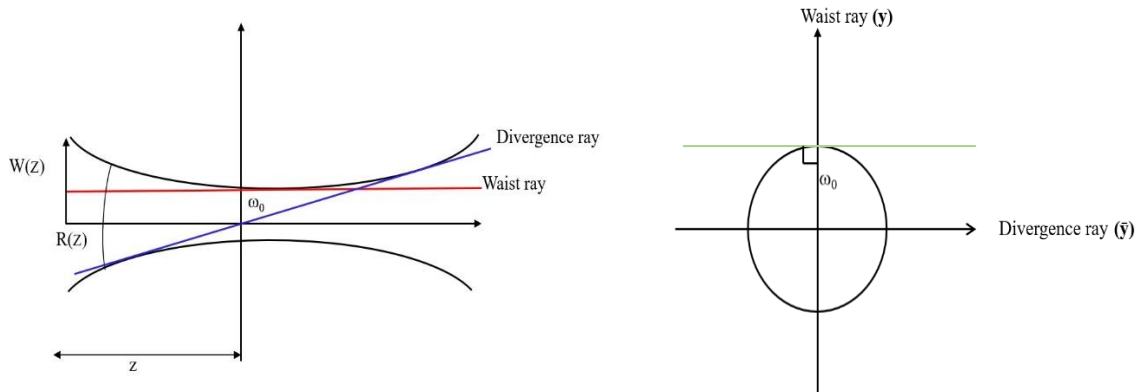


Figure 2.4 Layout of complex ray tracing for Gaussian laser beam propagation.

The blue line represents the divergence ray of the propagating Gaussian beam. The red line is a waist ray, a height ω_0 from the optical axis. In the $y\bar{y}$ method, the green line represents these two rays, with \bar{y} associated with the divergence ray and y associated with the waist ray-for this particular state. These rays are then traced just as paraxial rays. The beam waist size ω_0 is defined by the smallest distance from the traced line to the $y\bar{y}$ diagram origin, Or the beam waist is located where the line is tangent to a circle centered on the origin and its size is the radius of the circle. The properties of the complex ray tracing technique of Gaussian beam are tabulated in table 2.2.

Table 2.2 The properties of the complex ray tracing of Gaussian beam.

Properties	Brief description
$Lg = \frac{\lambda}{\pi}$	LaGrange invariant or the complex ray tracing scaling factor
$t1 = \frac{1}{Lg} \begin{bmatrix} y0 & \bar{y}0 \\ y1 & \bar{y}1 \end{bmatrix}$	Distance between 2 points in the complex ray tracing
$W = \sqrt{\bar{y}^2 + y^2}$	Beam semi-diameter
$\bar{U} = \frac{\bar{y}2 - \bar{y}1}{t1}$	Chief ray angle with the optical surface
$U = \frac{y2 - y1}{t1}$	Marginal ray angle with the optical surface
$R = \frac{-(y^2 + \bar{y}^2)}{(yu + \bar{y}\bar{u})}$	Radius of curvature of Gaussian beam
$Z0 = \frac{\pi y0^2}{\lambda} = \frac{y0^2}{L}$	Rayleigh range (only for lines of $y = a$)
$\Theta = \frac{\lambda}{\pi y0} = \frac{L}{y0}$	Divergence angle.

Chapter 3.

3.1 Simulation of Diffraction Using the Huygens-Fresnel Technique

Huygens posited that a wavefront could be represented as a large number of point sources, properly phased, where each of these point sources acts as a secondary emitter of spherical wavefronts [33] [34]. As the wavefronts pass through an aperture, some of the wavefront is clipped, bounding the set of point sources and changing the shape of the wavefront in the vicinity of and beyond the aperture edge. Interference effects are seen in the regions where overlap between the spherical wavelets occurs resulting in constructive or destructive interference.

For several decades, numerical Huygens-Fresnel diffraction propagation methods have been used extensively in research and industry for simulating beam propagation in many applications. The digital version of Fresnel equations is based on the fast Fourier transform (FFT), assuming monochromatic light. Fresnel propagation regimes and criteria can be expressed by a 2D source area $U_1(\xi, \eta)$ and 2D observation area $U_2(x, y)$, on parallel planes and arbitrary propagation distance r_{12} as shown in Figure 3.1 [12] [34].

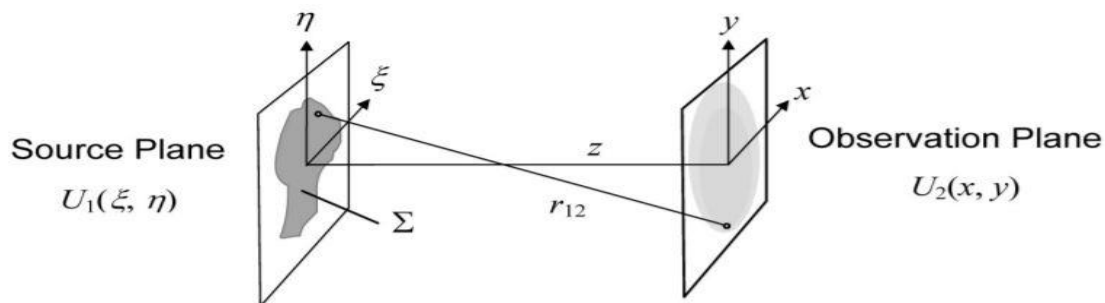


Figure 3.1 Sommerfeld geometry for normal incident collimated source and Observation planes [12] [35].

The Fresnel diffraction expression as shown in Eq. (3.1), can also be expressed as Eq. (3.2) [12] [34][37],

$$U_2(x, y) = \frac{e^{jkZ}}{j\lambda Z} \iint U_1(\xi, \eta) \exp \left\{ j \frac{k}{2Z} [(x - \xi)^2 + (y - \eta)^2] \right\} d\xi d\eta \quad (3.1)$$

$$U_2(x, y) = \frac{e^{jkZ}}{j\lambda Z} \iint U_1(\xi, \eta) h(x - \xi, y - \eta) d\xi d\eta \quad (3.2)$$

where the impulse response (IMP) is shown in Eq. (9),

$$h(x, y) = \frac{e^{jkZ}}{j\lambda Z} \exp \left[j \frac{k}{2Z} (x^2 + y^2) \right]. \quad (3.3)$$

The transfer function (TSF) is shown in Eq. (10):

$$H(x, y) = e^{jkZ} \exp \left[-j\pi\lambda Z (fx^2 + fy^2) \right]. \quad (3.4)$$

There are two ways to interpret Eq. (3.1), employing Eq. (3.1) or (3.4), yielding Eqn. (3.1) or (3.1):

$$U_2(x, y) = \mathcal{F}^{-1} \{ \mathcal{F} \{ U_1(x, y) \} \mathcal{F} \{ h(x, y) \} \}, \quad (3.5)$$

$$U_2(x, y) = \mathcal{F}^{-1} \{ \mathcal{F} \{ U_1(x, y) \} H(fx, fy) \}, \quad (3.6)$$

where \mathcal{F} and \mathcal{F}^{-1} are the Fourier transform and inverse Fourier transform respectively.

Despite the fact that Eqns. (3.5) and (3.6) are an identical solution for Eq. (3.1), different sampling values when computing these numerically can lead to conflicting and erroneous results. For relatively short propagation distances, or small λ , the TSF method is generally employed, whereas for relatively long propagation distances, or large λ , the IMP method is generally employed [12] [35]. Regardless, there are rigid sampling criteria for both IMP and TSF based solutions. Given a two-dimensional function with uniform square sampling,

$$g(x, y) = g(m\Delta x, n\Delta y), \quad (3.7)$$

where Δx and Δy are the sampling interval in the x and y directions respectively m and n are integer-valued indices. Letting $\Delta x = \Delta y$, the chirp function, TSF in Eq. (3.4) is sufficiently sampled by $\Delta x \geq \lambda Z/L_x$ where L_x is the size of the data array which encompasses the aperture including a surrounding zero band. Similarly, the chirp IMP function in Eq. (3.3) is sufficiently sampled when $\Delta x \leq \lambda Z/L_x$. These two expressions, which consider aliasing of the chirp function in the spatial and frequency domains respectively [12] [33], are clearly in opposition. The critical sample criteria should therefore work for both the TSF and IMP-based calculations when $\Delta x = \lambda Z/L_x$ [35] [36].

3.2 Gaussian Beam Decomposition Method

Any field distribution can be represented as a set of uniformly arrayed Gaussian beamlets. For a simple example, we choose a square aperture illuminated with a normally incident plane wave, a flat top beam profile with uniform amplitude and initial constant phase. This example contains the requirements of a smooth field amplitude as well as a sharp field edge, both of which can be quantified. As it has a flat phase field, the beamlets will all have their waists at the aperture plane. To obtain a flat top-hat amplitude profile with minimum ripples, the adjacent Gaussian beamlets must sufficiently overlap. We denote overlap factor (OF) as the ratio of the beam diameter, $D = 2\omega_0$ at $1/e^2$ irradiance to the adjacent beamlet center separation [15] [16] [17] [18] [19] [20] [21] [22] C_s , by $OF = \frac{D}{C_s}$. For a square aperture, there are a few restrictions; the number of Gaussian beamlets required along two dimensions (2D) to fill the square aperture is $N_G = \frac{L_s \cdot OF}{D}$, where L_s is the square aperture length. Although there is no exact value for minimum waist size, a reasonable value for the Gaussian beam decomposition (GBD) approach is $\omega_0 \geq 3\lambda$

[17] and this criterion [33] will not conflict with Gaussian beam solution of paraxial wave equation restrictions as mentioned in Sec.2.1.

When $OF = 1.00$, there will be substantial irradiance variation (ripples) in the GBD representation. On the other hand, $OF=2.00$ yields a decrease in the steepness of the edge roll-off. To balance these two limitations $OF \approx 1.50$ could be used.

The discrepancies among overlapping factors 1.00, 1.50 and 2.00 respectively at the plane of decomposition ($Z=0$) are shown in Figure 3.2 [15] [17]. We simulated a square aperture of dimensions $L_{sx}=L_{sy} = L_S=20\text{mm}$. The simulation uses $N_G = 11$, so 11x11 beamlets in the arrays and

$\lambda = 0.5 \cdot 10^{-6}$ m. The separation between two adjacent beamlets is 1.82 mm which leads to $\omega_0 = 0.91\text{mm}$, 1.36mm and 1.82mm respectively.

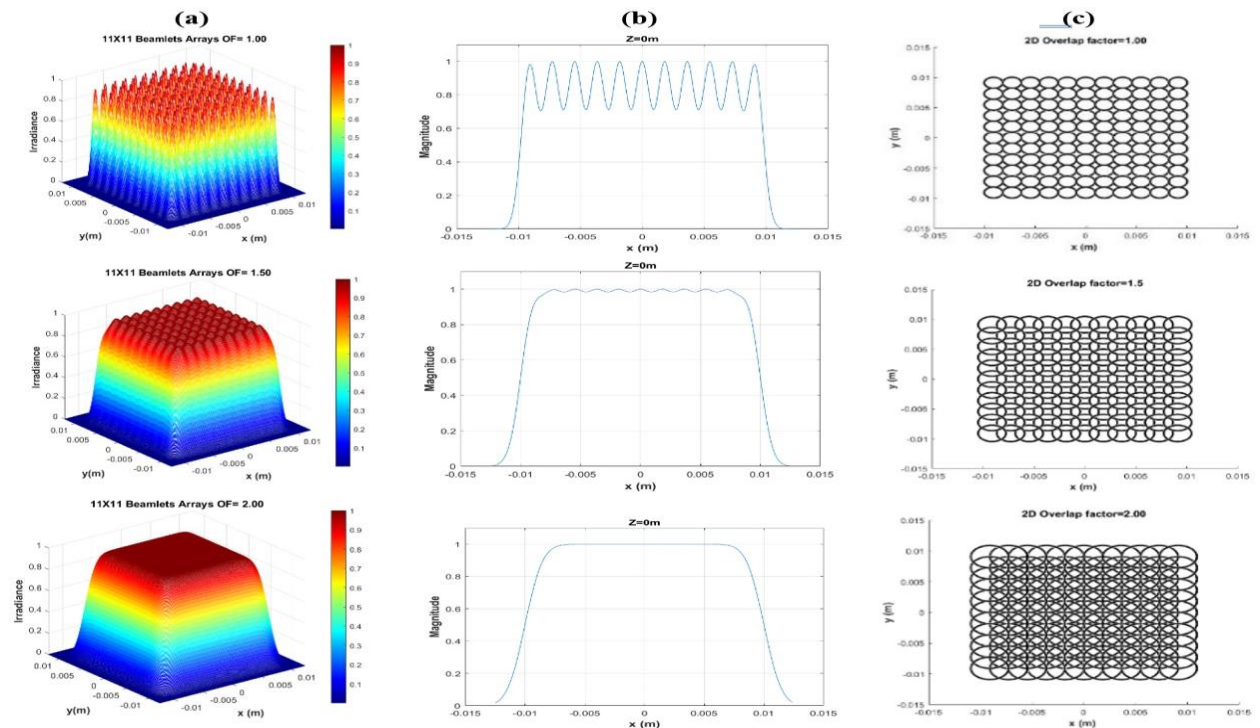


Figure 3.2 Column (a) normalized 3D irradiance at $Z=0$ showing ripples and roll off slope, **column (b)** normalized field magnitude cross section at $Z=0$ and **column (c)** 1/2 map radii of 11x11 beamlets [15] [17].

Chapter 4.

4.1 Modeling the Diffraction Pattern of Square Aperture by Overlap Factor 1.5 and FFT Using the IMP and TSF

We will demonstrate and compare the diffraction patterns for a square aperture because we know, analytically, the diffraction pattern for it with long propagation distances, the Fraunhofer regime and near field Fresnel distances have been well documented. We shall employ different beamlet numbers, N_G and beamlet sizes, ω_0 and $OF=1.5$. The decomposition into Gaussian beamlet propagation is a fast and simple technique. The GBD methodology can simulate the diffraction pattern at any propagation plane location; far field or near field, at any propagation distance and at any spatial resolution in the output plane. However, one must trade top hat smoothness for edge roll off. The constraints and limitations of the FFT methodology are well known and were briefly discussed.

The first example is near field propagation. For simplicity, we used the critical sample criteria $\Delta x = \lambda Z/L_x$ and $\lambda=0.5*10^{-6}$ m to satisfy the IMP and TSF [12]critical sampling rate simultaneously with square aperture length= 102 mm and propagation distance $Z= 2000$ m employing a grid of $X \times X$ data points. We chose 77×77 beamlets and $OF = 1.5$ for the GBD method. We have not investigated methods of making the code more efficient, so using 5929 beamlets will slow down the algorithm time, but at this stage, we are focusing on the accuracy of

these calculations, not the speed. For the FFT-based approach, MATLAB code based on Ref. [12] was written. We also created MATLAB code for the GBD method.

The second example is far field propagation. We modeled a smaller square aperture with length size =20mm, again propagating $Z= 2000$ m. For this calculation, 15x15 beamlets for used for GBD and the sampling rate for TSF and IMP were unchanged.

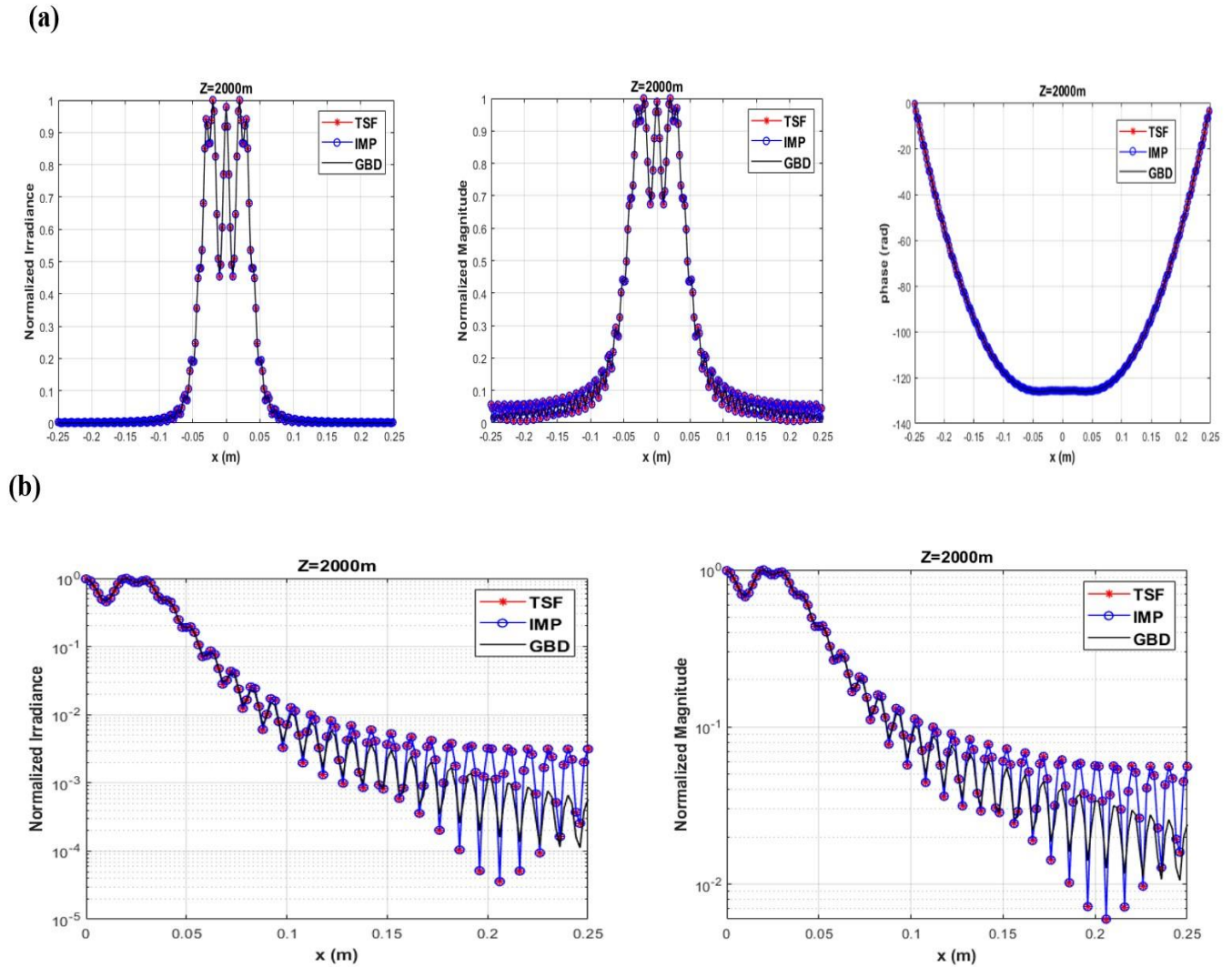
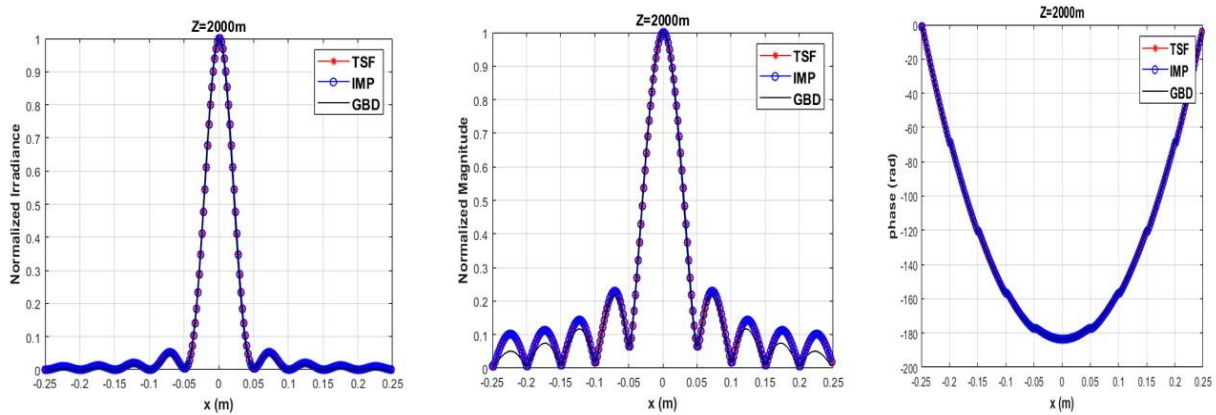


Figure 4.1 (a) comparison of irradiance, magnitude and phase among TSF, IMP and GBD for 102x102 (mm) square aperture with 77X77 beamlets and row (b) a base-10 logarithmic scale on the irradiance and magnitude of TSF, IMP and GBD respectively for 102x102 (mm) square aperture with 77X77 beamlets.

(a)



(b)

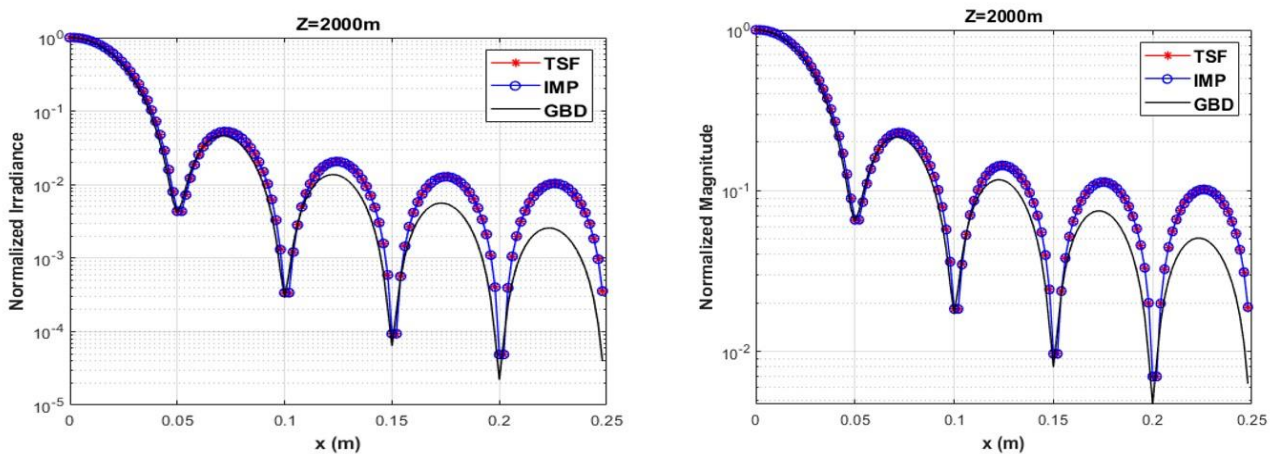


Figure 4.2 (a) comparison of irradiance, magnitude and phase among TSF, IMP and GBD, respectively for 20×20 mm square aperture with 15×15 beamlets and row (b) a base-10 logarithmic scale on the irradiance and magnitude of TSF, IMP and GBD respectively for 20×20 mm square aperture with 15×15 beamlets.

The results in Figs.4.1 are from the near field diffraction example and Figs.4.2 are for far field Fraunhofer diffraction pattern. It is apparent that both results match well, with some indications of the edge smoothing from the GBD primarily evident in the far field calculations. We note that the zeroes of the functions overlap precisely, matching the simple far-field result from a square aperture with uniform amplitude as given by Eqn. 4.1 [12] [35] [36].

Note that the width of the central lobe for the far field pattern is Eqn.4.2 [12] [35] [36] which matches the results. Note also that the TSF, IMP and GBD using $OF=1.5$ results are almost

identical with slight difference in amplitude for lobes number 3,4 and 5. By increasing the number of beamlets, N_G , while keeping OF constant, the smoothness of the top hat remains and, because ω_0 is decreasing, the edge steepness increases. Thus, the second lobe irradiance goes from $\approx 1.75X$ factor error with 15×15 beamlets, to less than a 5% error at the 5th lobe using 77×77 beamlets:

$$U(\xi, \eta) = \text{rect}\left(\frac{\xi}{L_s}\right) \text{rect}\left(\frac{\eta}{L_s}\right). \quad (4.1)$$

Again, the constant L_s is the widths of the square aperture in ξ and η directions:

$$x_0 = \frac{\lambda Z}{L_s} = 0.05 \text{ m}. \quad (4.2)$$

Thus, equation 4.3 defines complete results for computing the diffraction from a square aperture illuminated by a plane wave using the GBD method. Equation 4.3 for the square aperture is a simple double summation over the Gaussian beamlets, computed for any $(x, y; Z)$ position in the diffracted field using well known Gaussian beam equations:

$$U_2(x, y; Z) = \frac{\omega_0}{w_1} \exp(ikz) \exp(-itan^{-1}\left(\frac{Z}{zr}\right)) * \sum_{-\Delta x(m)}^{\Delta x(m)} \left[\sum_{-\Delta y(n)}^{\Delta y(n)} \exp\left(\frac{-((X-\Delta x(m))^2 + (Y-\Delta y(n))^2)}{(W(Z))^2}\right) \exp\left(\frac{ik((X-\Delta x(m))^2 + (Y-\Delta y(n))^2)}{(2R(Z))}\right) \right], \quad (4.3)$$

where $\Delta x(m) = \Delta y(n)$ are beam center locations determined once C_s is defined and $W(Z)$, $R(Z)$ and the Gouy phase values were defined in table 2.4. This equation can be manipulated for any aperture such as circle, or triangle aperture by changing the Gaussian beamlet locations, or for a non-planar wavefront by appropriately addressing the initial Gaussian beamlet curvature and phase.

4.2 Hybrid Overlap Factor Configuration

We now discuss how to improve the accuracy of the GBD fit for the square aperture to both minimize the ripple in the top hat region and increase the steepness of the edge. Increasing the overlap factor decreases ripple and decreases the steepness of the edge, whereas, decreasing the overlap factor will lead to increased ripple and an increase the steepness of the edge. One could increase the number of beamlets at constant OF which would make the edges steeper due to the gaussian beamlets being narrower, but at the cost of increasing the number of computations. What we propose instead is to mix different beam waists in the decomposition: broad gaussians where the field is slowly varying at the center of the aperture and narrow gaussians where the field is rapidly varying at the edges. Thus, one can achieve reduced ripple and sharper edges while using far less beamlets than if one had used the smaller beamlets throughout. Values of OF=2 can be used for all beamlets, ensuring a smooth fit. Alternatively, OF selection can be an adjustable parameter. Any field can be decomposed to GBD or hybrid Gaussian beam decomposition (HGBD).

We again simulate the 20 mm aperture with $\lambda = 0.5 \cdot 10^{-6}$ m. The central 7x7 beamlets were set to OF=2 and defined for a 15mm square, yielding $\omega_0 = C_S = 2.143$ mm. The edge beamlets are also set to OF=2 and we arbitrarily set terms so that $\omega_0 = C_S = 1.25$ mm and then added them with the appropriate amplitude to yield a uniform field amplitude, accounting for both the average amplitude vs OF and the remaining residual field amplitude needed after the central beamlets were summed.

One feature in using the hybrid beamlets configuration is that amplitudes of the summation of beamlets are driven by OF, so maintaining the same OF simplifies the summation. However, the boundary between the large and small beamlets creates an asymmetric summation

feature, a ridge, in the field distribution. This was solved by fitting a third set of Gaussian beamlets, of another size, which effectively removed the ridge. We used a third Gaussian beamlets of $\omega_0=1.9$ mm. Figures.5 shows the normalized 3D irradiance, 2D normalized field magnitude and $1/e^2$ map radii of HGBD for the 20mm square aperture.

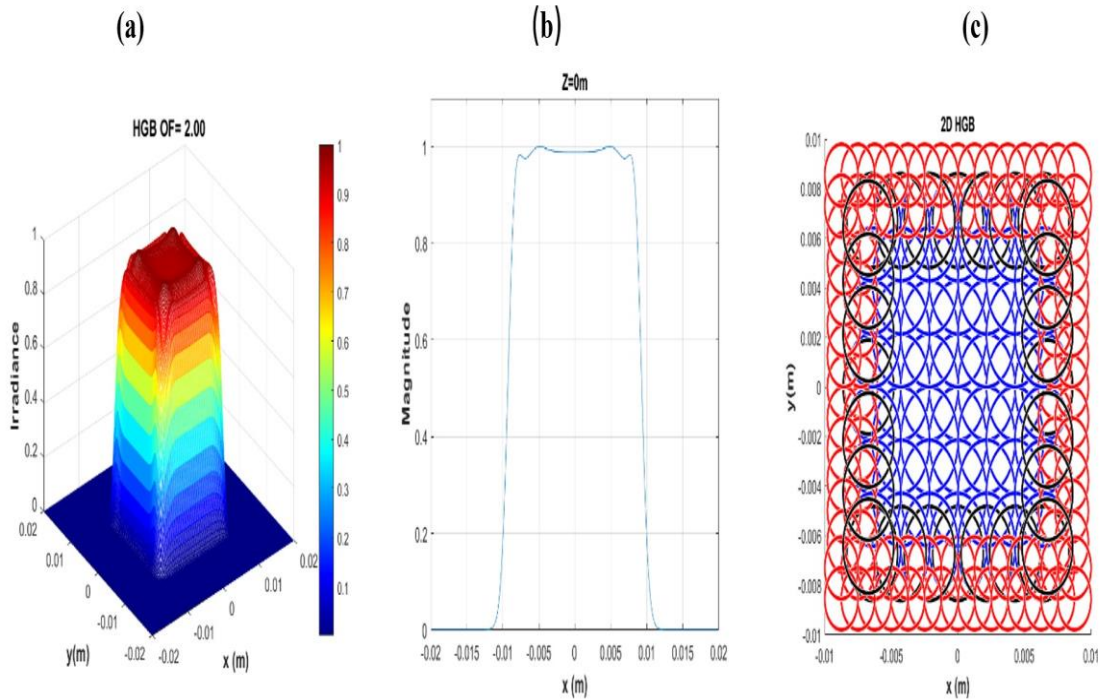


Figure 4.3 (a) normalized 3D field irradiance at $Z=0$ showing ripples and roll off slope, **column (b)** normalized field magnitude cross section at $Z=0$ and **column (c)** $1/e^2$ map radii of 11×11 beamlets.

We compared the diffraction pattern at near and far field between the GBD and HGBD models in Figs.4.4 and 4.5. All models employed $OF = 2$, but for the two different GBD models, we matched the largest and smallest beamlet sizes used in the HGBD model, equivalent to $N_G = 9$ and $N_G = 17$ for the 20mm square aperture. The $Z=50$ m near field propagation for these two GBD models and the HGBD are shown in Figure 4.4. It is clear that the $N_G=9$ GBD model does not effectively capture the expected modulation at the center of the pattern which leads to artifact, whereas the HGBD and $N_G=17$ GBD models closely match and show the expected

modulations. A similar result is shown for the far field calculations in Figure 4.5, where it is apparent that the HGBD and $N_G=17$ GBD are a close match. Thus, the HGBD model, which employs 181 gaussian beamlets achieves the same resolution as the GBD model that employs 289 beamlets, implying a potential reduction in calculations of 37% once the decomposition is completed.

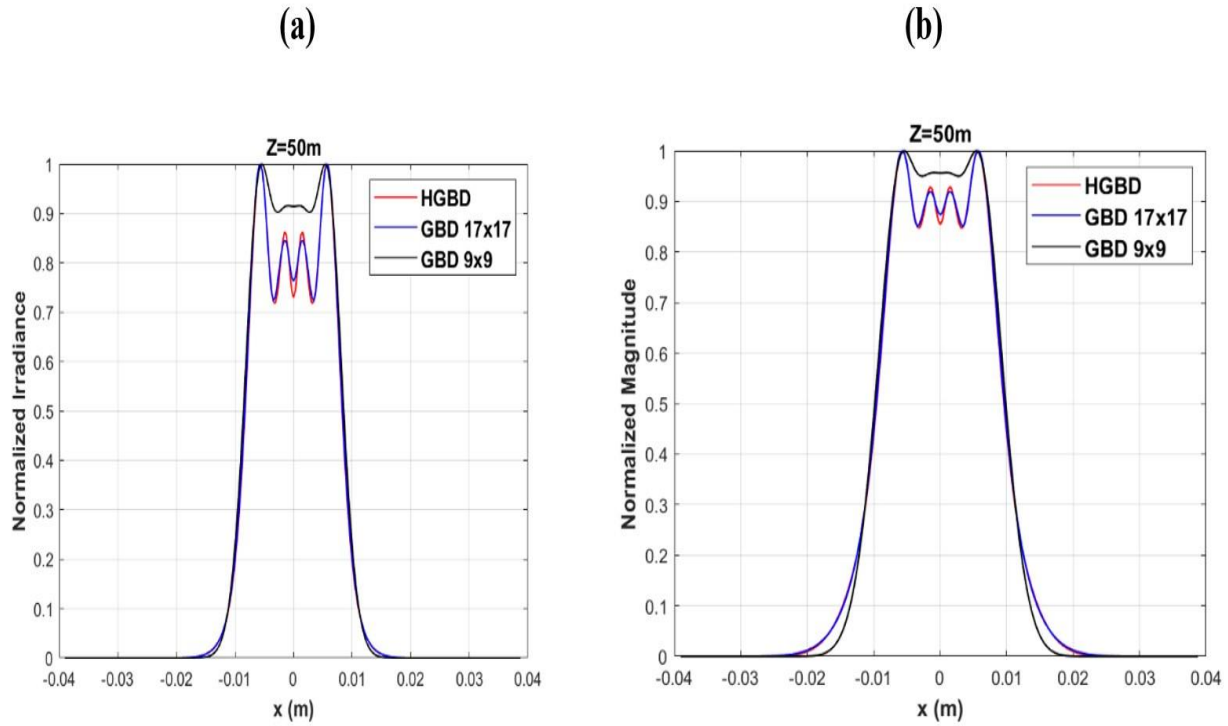


Figure 4.4 (a) comparison of irradiance between HGB, GBD17x17 and GBD 9X9 respectively for 20x20 mm near field square aperture (b) comparison of magnitude, between HGBD and GBD17X17, GBD 9X9 respectively for 20x20 mm near field square.

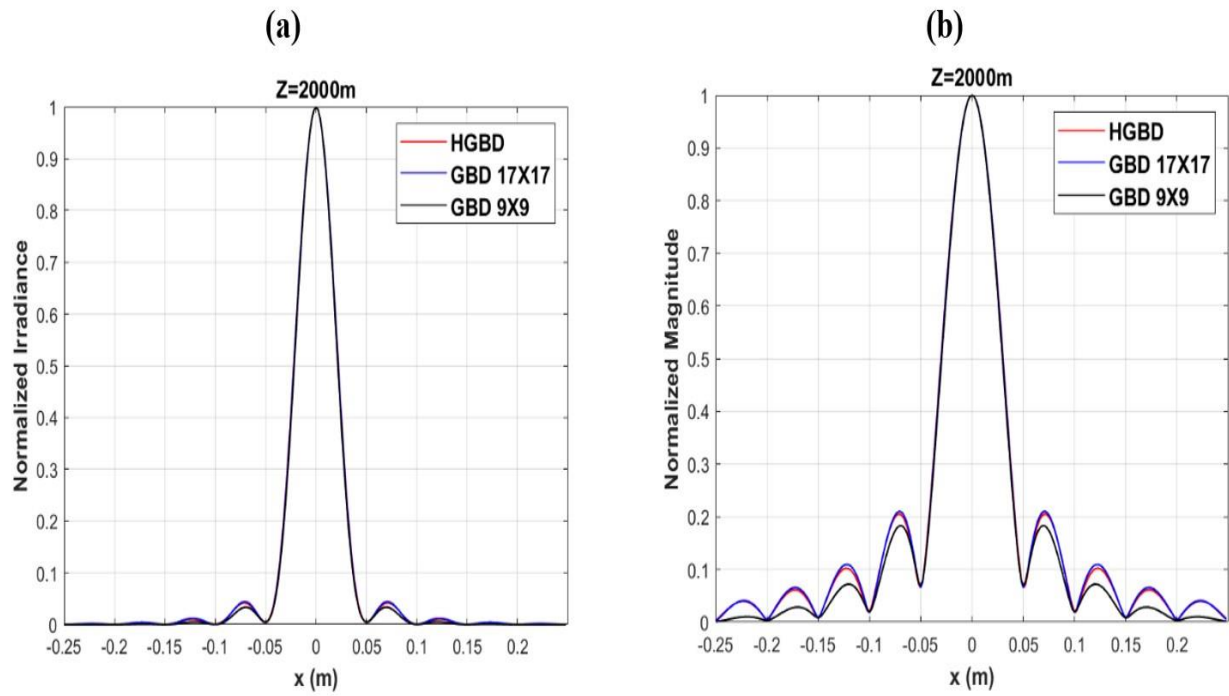


Figure 4.5 (a) comparison of irradiance between HGB, GBD17x17 and GBD 9X9 respectively for 20x20 mm far field square aperture (b) comparison of magnitude, between HGBD and GBD17X17, GBD 9X9 respectively for 20x20 mm far field square.

Chapter 5.

5.1 Introduction

In this chapter, we present Herriott's approach to design off-axis multi-pass cavities (HCMPC) with numerical examples. We were involved in the analysis, redesign, fabrication and testing of a HCMPC spectrometer [25] [26] [27] [28] [29] for measuring the O₂, CO₂ and H₂O levels aboard the Orion space capsule. The design provided to us was created following the methods described by Herriott [1]. We found that Herriott's design approach, though sufficient, obscured how one would design a system from the first principles. In this Chapter firstly, we present a detailed overview and analysis of the original design method developed by Pierce [3] and Herriott. Secondly, we use Zemax to analyze the HCMPC's. Thirdly, we show the process for converting the HCMPC gut ray trace to HCMPC a paraxial model collimated ray. Lastly, we show step-by-step of using HCMPC displacement value as $y\bar{y}$ diagram values. In the following chapters we will present a step-by-step for an innovative $y\bar{y}$ diagram approach for designing an absorbance spectrometer MPC, with several examples.

5.2 Herriott Cell Background and Design Analysis

The fundamental Herriott cell consists of a pair of identical positive powered (concave) mirrors designed to provide a repeating optical path for an optical beam inserted into the cell.

Pierce [3] has described and derived a paraxial solution in terms of a series of equally spaced positive lenses with the same focal lengths. In terms of ray optics, the interferometer system consisting of two equal and coaxial spherical mirrors is equivalent to a series of lenses. The analysis of a paraxial solution in periodic focusing arrays was first applied to electron beam design. Extension of this paraxial solution applied to the optical realm was accomplished by Herriot *et al.* in 1964. Although Herriott's original work was proposed for additional resonances for off-axis interferometer [1][3], it was not until recently applied to variety of applications such as tunable diode laser spectroscopy with long absorption path to detect gas molecules and to obtain high energy femtosecond pulses from a compact laser cavity. Extremely long laser cavities or a long path spectrometer can be compressed into small sizes as shown in Figure 5.1, where the blue line indicates the multiple paths a single beam takes in the cell. We focus here and on the following chapters, on its application to laser spectroscopic using tunable sources, enabling long absorption paths in a short package, including NASA's laser air monitoring spectrometer system (LAMS) for the Artemis III mission. LAMS's 31 laser beam bounces resulted in a 31X reduction in overall system length highlighting how extremely long path spectrometers can be compressed into small sizes using a Herriott cell. Herriott's derivation assumes that the two mirrors are concave of the same radii of curvatures, separated by a vertex distance of L and that the "exit" point overlaps the "injection" point. Conversely, for spectroscopic applications the injected beam can't overlap the exit beam.

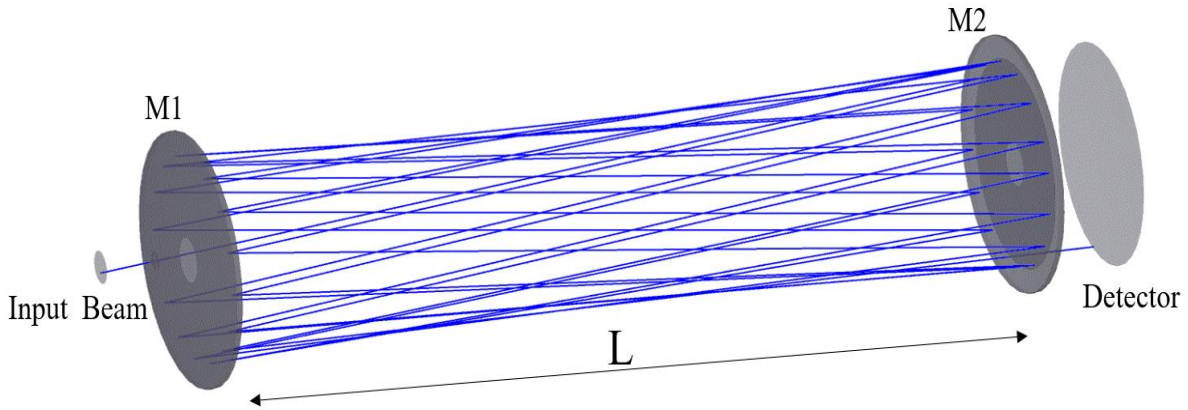


Figure 5.1 A schematic of a Herriot type multi-pass cavities MPCs [7].

Round trips can be presented by the (ABCD) matrix. Imagine a ray starting in the plane of the left mirror and after a round trip through the MPCs, this ray will have been transferred across the length L , reflected by the spherical mirror of radius of curvature R_2 , transferred another length L and finally reflected by the spherical mirror of radius of curvature R_1 where we will let $R_1 = -R_2$, so it is again back in the plane of M_1 and aiming towards M_2 as illustrated in Fig 5.2. The ray matrix describing the ray transformation by round trip through the MPCs are shown in equations 5.1 and 5.2 [30] [31] [33] [37] by:

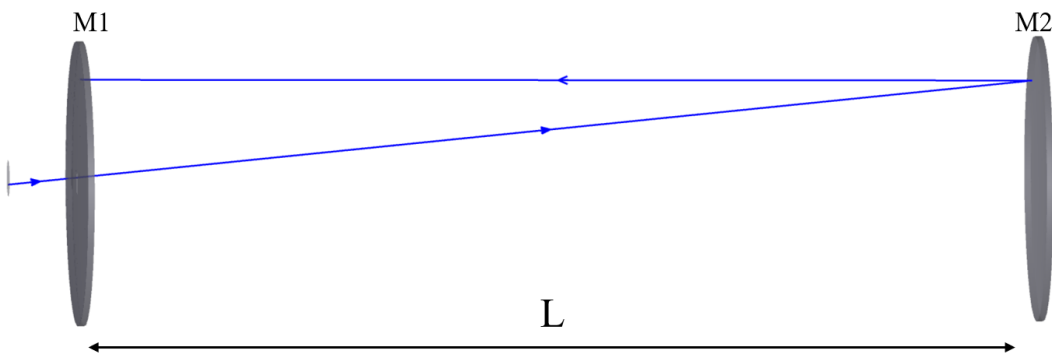


Figure 5.2 A round trip through the multi-pass cavities (MPCs) [7].

$$\begin{bmatrix} A & B \\ C & D \end{bmatrix} = \begin{bmatrix} 1 & 0 \\ \frac{2}{-R_1} & 1 \end{bmatrix} \begin{bmatrix} 1 & L \\ 0 & 1 \end{bmatrix} \begin{bmatrix} 1 & 0 \\ \frac{-2}{R_2} & 1 \end{bmatrix} \begin{bmatrix} 1 & L \\ 0 & 1 \end{bmatrix}, \quad (5.1)$$

$$\begin{bmatrix} A & B \\ C & D \end{bmatrix} = \begin{bmatrix} 1 - \frac{2L}{R_2} & 2L - \frac{2L^2}{R_2} \\ \frac{4L}{R_2 R_1} - \frac{2}{R_1} - \frac{2L}{R_2} & 1 - \frac{2L}{R_2} - \frac{4L}{R_1} + \frac{24L^2}{R_1 R_2} \end{bmatrix}. \quad (5.2)$$

After N round trips through the MPCs, therefore, the initial ray with displacement r_i and slope r_i' is transformed to the ray with displacement r_N and slope r_N' given by [31]

$$\begin{bmatrix} r_N \\ r_N' \end{bmatrix} = \begin{bmatrix} A & B \\ C & D \end{bmatrix}^N \begin{bmatrix} r_i \\ r_i' \end{bmatrix}. \quad (5.3)$$

This ray matrix has determinant equal to $AD-BC=1$ and defining an angle θ by

$$\cos\theta = \frac{1}{2}(A + D) \text{ or } \cos\theta = 1 - \frac{L}{R}. \quad (5.4)$$

The ABCD matrix after N rounds can be shown as [39]

$$\begin{bmatrix} A & B \\ C & D \end{bmatrix}^N = \begin{bmatrix} \frac{A-D}{2} \frac{\sin N\theta}{\sin\theta} + \cos N\theta & B \frac{\sin N\theta}{\sin\theta} \\ c \frac{\sin n\theta}{\sin\theta} & \frac{D-A}{2} \frac{\sin N\theta}{\sin\theta} + \cos N\theta \end{bmatrix}. \quad (5.5)$$

The stability of MPCs, in other words, the condition that the rays remain confined, are shown in Equation 5.6 [30] [31] [33] [37] :

$$0 \leq g_1 g_2 \leq 1 \quad \text{where} \quad g_1 = 1 - \frac{L}{R_1} \quad \& \quad g_2 = 1 - \frac{L}{R_2}. \quad (5.6)$$

Herriot noticed that Equation 5.6 can be reduced to equation 26 when $R_1=R_2$ [1] [37]

$$0 < \frac{L}{f} < 4. \quad (5.7)$$

Once again, the system can be unfolded into series of thin lenses of focal length $f=|R/2|$, each separated by a length equal to L.

By using well-known techniques of matrix algebra and Sylvester's theorem the displacements r_N coordinates x_n and y_n are equal to [37]

$$x_n = x_0 \cos N\theta + \left(\frac{x_0(A-D)+2Bx'_0}{2\sin\theta}\right)\sin N\theta, \quad (5.8)$$

$$y_n = y_0 \cos N\theta + \left(\frac{y_0(A-D)+2By'_0}{2\sin\theta}\right)\sin N\theta. \quad (5.9)$$

The corresponding relation for equal radii is [1]:

$$x_n = x_0 \cos N\theta + \sqrt{\frac{L}{4f-L}}(x_0 + 2fx'_0)\sin N\theta, \quad (5.10)$$

where $x_n, x_0, N, f, \theta, x'_0$ are the repeated radial displacements and the input beam coordinate in axis direction, number of intercepts on the front and back spherical mirrors, the mirror focal length ($f = |R|/2$), the angle between successive intercepts and the slope of input beam, respectively.

A corresponding relation holds for y_n [1]:

$$y_n = y_0 \cos N\theta + \sqrt{\frac{L}{4f-L}}(y_0 + 2fy'_0)\sin N\theta. \quad (5.11)$$

The previous equations can be simplified as [1]:

$$x_n = A \sin(N\theta + \alpha) \quad (5.12)$$

$$y_n = B \sin(N\theta + \beta), \quad (5.13)$$

where A and B are the maximum x- and y-semi-diameters of beam bounces on the mirrors. A circular pattern is formed when

$$A = B \quad \& \quad \alpha = \beta \pm \frac{\pi}{2}. \quad (5.14)$$

5.3 The Multi-Passes Consecutive Re-entrant Condition

The multi-pass cavities (MPCs) can be designed in such a way that the beam bounces will be consecutive or interlaced bounces as the beam progresses around the optical axis. It is only the relationship between (θ) , the number of intercepts (2ν) and the number of 2π rotation. Where 2ν is the number of intercepts in the cavity and θ rotates counterclockwise:

$$2\nu\theta = 2\pi. \quad (5.15)$$

If the resonator dimensions are such that $2\nu\theta$ is equal to 2π as shown in equation 5.15, then a ray consecutively returns exactly to its entrance point $(x_0, y_0) = (x_n, y_n)$ after 2ν trips through the cavity and continues to retrace the same ray pattern again and again.

We can use the above finding to understand the way in which a ray is reflected back- and- forth between the two concave mirrors of resonator. The even numbered intersection points will be the point where the ray strikes the one mirror and the odd numbered points will correspond to the points of impact on the other mirror.

For instance, closed paths of this type are known to exist for a confocal resonator with a repetition rate of two returns or $2\nu = 4$. This will lead to a common and important design. The confocal resonator, with mirrors of radii equal to the cavity length ($2f = R_1 = R_2 = L$). This MPC design produces the smallest possible beam diameter at the cavity mirrors for a given cavity length and is often used in lasers where the purity of the transverse mode pattern is important.

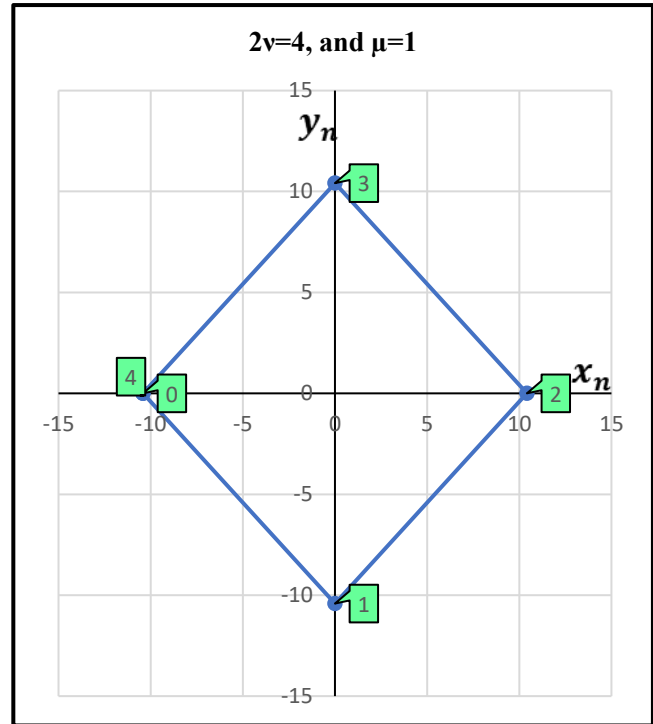
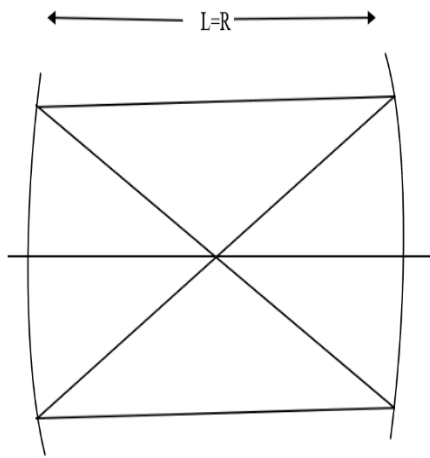


Figure 5.3 Consecutive confocal cavity and correspond (x_n, y_n) diagram plot.

Table 5.1 Consecutive Confocal cavity passes (a) (x_n, y_n) values (b) design parameters.

(a)

$2v$	x_n	y_n
0	-10.414	0
1	0	-10.414
2	10.414	0
3	0	10.414
4	-10.414	0

(b)

v	2
$\Theta(\text{rad})=$	$\pi/2$
$\text{COS}(\Theta)$	0
$L=$	75.552
$R=$	75.552

Another well-known MPC cavity when a cavity with a mirror separation equal to the focal length ($L=f$) and closed path of three returns or $2v = 6$.

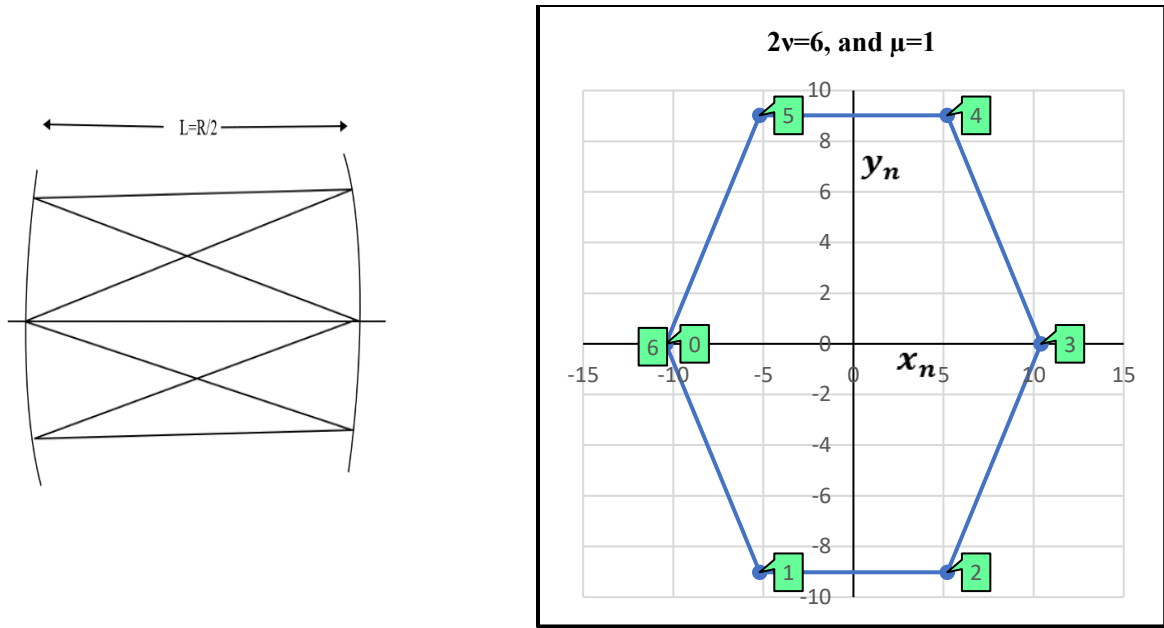


Figure 5.4 Consecutive focal cavity and correspond (x_n, y_n) diagram $2\mu=6$ plot.

Table 5.2 Consecutive focal cavity passes (a) (x_n, y_n) values (b) design parameters.

(a)		
$2v$	x_n	y_n
0	-10.414	0
1	-5.207	-9.0188
2	5.207	-9.0188
3	10.414	0
4	5.207	9.0188
5	-5.207	9.0188
6	-10.414	0

(b)	
$v =$	3
$\Theta(\text{rad}) =$	1.047197551
$\text{COS}(\Theta)$	0.5
$L =$	75.5523
$R =$	151.1046

Another multi-passe cavity example is when $2v = 32$ and $L = 75.55$ mm that will lead to

$|R1| = |R2| = 3932$ mm.

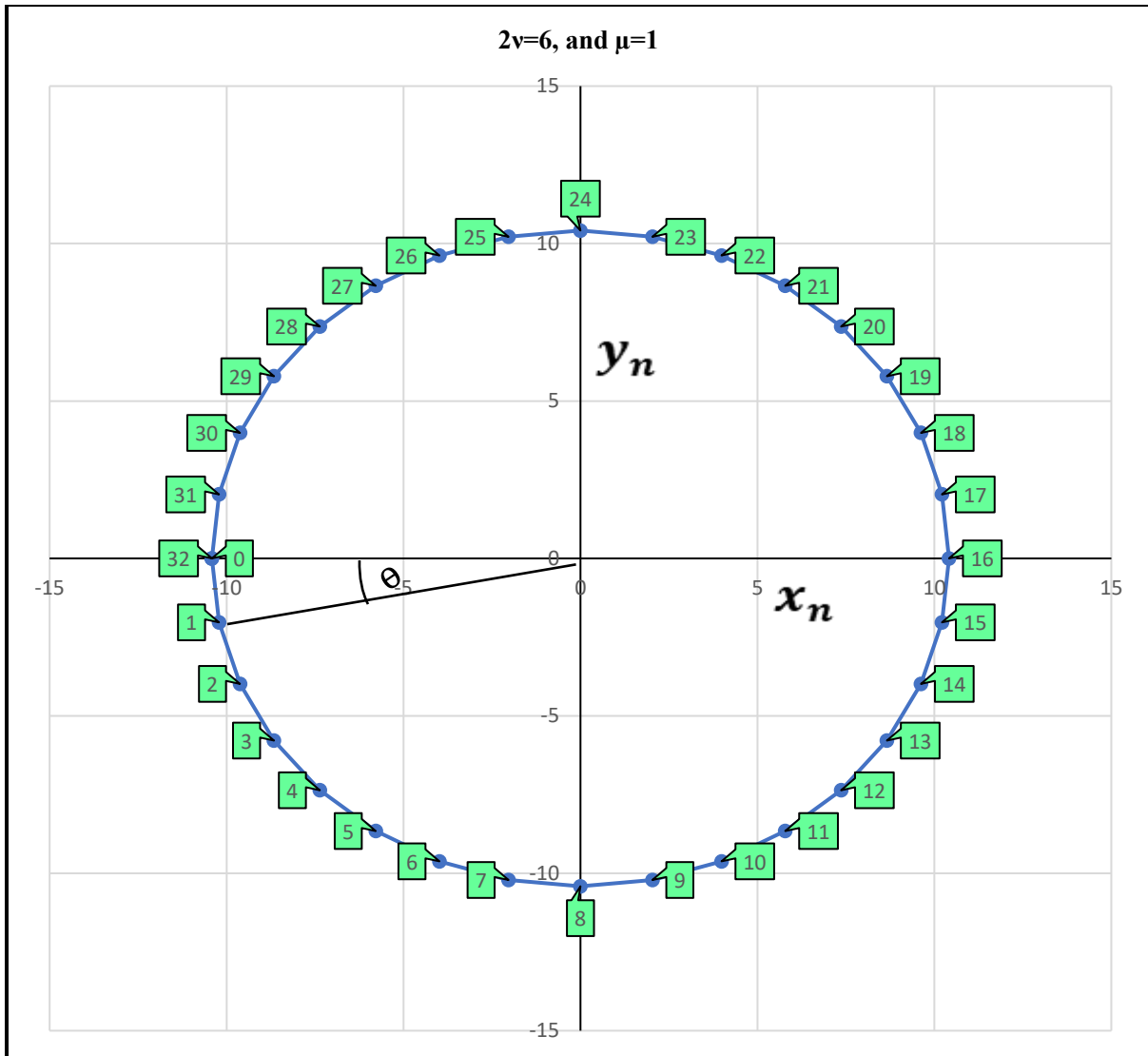


Figure 5.5 Consecutive multi-pass cavity and correspond (x_n, y_n) diagram plot.

Table 5.3 Consecutive multi-pass cavity passes **(a)** (x_n, y_n) values **(b)** design parameters .

(a)

2ν	x_n	y_n
0	-10.41400	0
1	-10.21390	-2.031671
2	-9.62128	-3.985265
3	-8.65892	-5.785708
4	-7.36381	-7.36381
5	-5.78571	-8.658925
6	-3.98527	-9.621281
7	-2.03167	-10.2139
8	0.00000	-10.414
9	2.03167	-10.2139
10	3.98527	-9.621281
11	5.78571	-8.658925
12	7.36381	-7.36381
13	8.65892	-5.785708
14	9.62128	-3.985265
15	10.21390	-2.031671
16	10.41400	-1.28E-15
17	10.21390	2.031671
18	9.62128	3.985265
19	8.65892	5.785708
20	7.36381	7.36381
21	5.78571	8.658925
22	3.98527	9.621281
23	2.03167	10.2139
24	0.00000	10.414
25	-2.03167	10.2139
26	-3.98527	9.621281
27	-5.78571	8.658925
28	-7.36381	7.36381
29	-8.65892	5.785708
30	-9.62128	3.985265
31	-10.21390	2.031671
32	-10.41400	2.55E-15

(b)

$\nu =$	16
$\Theta(\text{rad})=$	0.196350
$\text{COS}(\Theta)$	0.980785
$L=$	75.552
$R=$	3931.98556

From equations 5.4 and 5.15 the MPC can be designed with consecutive bounces. In other words, if the designer specifies the numbers of passes $2v$ and the cavity length L the MPC can be designed, as long as, the stability condition is met. A comparison among the three consecutive cavities explained above are shown in table 5.6.

In the following chapter we will explain in detail how one can calculate the numbers of intercepts and the cavity length L for absorbance spectrometer. In this chapter we are focusing on Herriot approach with arbitrary number of intercepts 2μ and the cavity length L .

Table 5.4 Comparison among three different cavities.

v	2	3	16
$\Theta(\text{rad})=$	1.570796	1.0472	0.196350
$\text{COS}(\Theta)$	0	0.500	0.980785
$L=$	75.55	75.55	75.55
$ R =$	75.5523	151.1046	3931.98556
$f=$	37.776	75.552	1965.993
f/d	0.5	1	26.02172
d/f	2	1	0.038429

It is only the ratio between focal length focal length and the mirror spacing and Θ which determine whether the MPC will have closed path or not. If the condition $0 < \frac{L}{f} < 4$ holds, a ray returns to its entrance point after 2μ no matter what its entrance slope, additionally, a 1:1 image magnification of the input spot after $2v$ and inverted image after v trips. The encircled energy does not degenerate as the beam bounces back and forth between the mirrors. The beam is continuously refocused by the concave mirrors [1] [37].

5.4 The Interlaced Re-entrant Condition

The MPCs can be designed in such a way that the beam intercepts will be interlaced on a circle. It is only the relationship among θ , the number of intercepts $2v$ and the number of 2π rotation (μ). Where v is the number of intercepts on each mirror and μ is an integer number [1] [40]:

$$2v\theta = 2\mu\pi. \quad (5.16)$$

The interlaced beam intercepts equation 5.16 with odd μ and even $2v$ shall be used for spectroscopic design for multi-passes cavity. By adjusting the odd value of μ number, the designer can choose a specific output beam intercepts coordinate and certain detector location.

By way of explanation, there are three rules for equation 5.16 namely:

1. When v and μ share odd common factors, the results are inappropriate solutions. For example, if $2v = 2 \times 3$ and μ is 3, a common factor of $2v$ and μ is odd numbers or 3 and $\theta = \pi$, therefore this solution can be quickly rejected.
2. When $2v$ and μ share even common factors, the results are inappropriate solutions. For example, if $2v = 2 \times 3$ and μ is 2, a common factor of $2v$ and μ is even numbers or 2 and $\theta = 120^\circ$ that will lead to 3 intercepts instead of 6 intercepts, therefore this solution can be quickly rejected.
3. The confocal and focal MPC are distinctive resonators and never change the intercepts coordinate locations, as illustrated in Figure 5.6 and Figure 5.7.

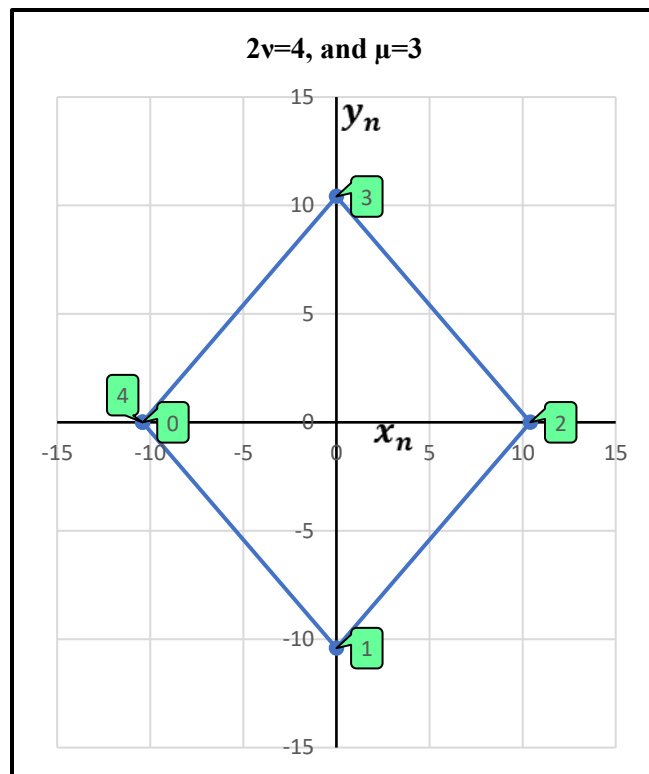
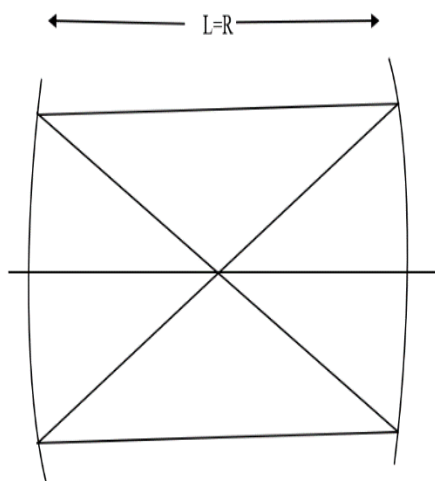


Figure 5.6 Distinctive interlaced confocal cavity and correspond (x_n, y_n) diagram plot.

Table 5.5 Interlaced Confocal passes (a) correspond (x_n, y_n) (b) design parameters values.

(a)

$2v$	x_n	y_n
0	-10.414	0
1	0	-10.414
2	10.414	0
3	0	10.414
4	-10.414	0

(b)

$v =$	2
$\Theta(\text{rad}) =$	4.7123
$\text{COS}(\Theta)$	0
$L =$	75.552
$R =$	75.552

An example when a cavity with a mirror separation equal to the focal length ($L=f$) one has closed path of three returns or $2v = 6$ and $\mu = 3$.

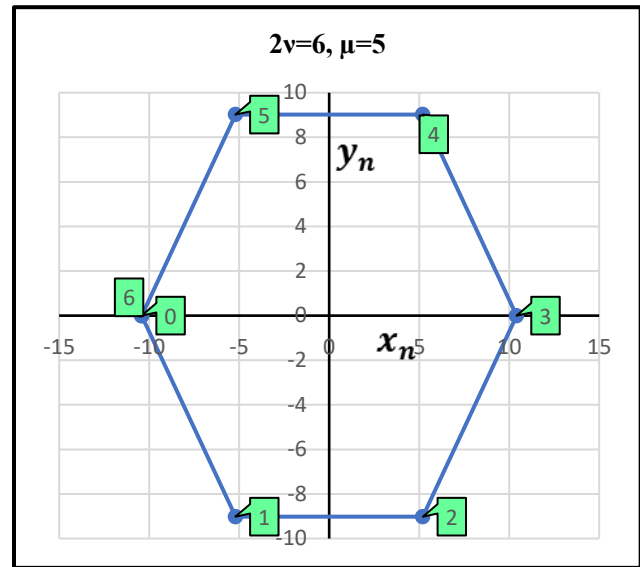
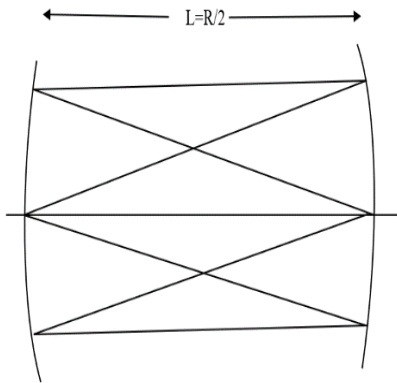


Figure 5.7 Distinctive interlaced focal cavity and correspond (x_n, y_n) $2v=6$ and $\mu=5$ plot.

Table 5.6 Distinctive interlaced focal passes (a) correspond (x_n, y_n) (b) design parameters values.

(a)

2μ	x_n	y_n
0	-10.414	0
1	-5.207	-9.0188
2	5.207	-9.0188
3	10.414	0
4	5.207	9.0188
5	-5.207	9.0188
6	-10.414	0

(b)

$\mu=$	3
$\Theta(\text{rad})=$	5.235988
$\text{COS}(\Theta)$	0.5
$L=$	75.5523
$R=$	151.1046

Another example when $2\nu = 32$, $\mu = 5$ and $L = 75.55$ mm that will lead $|R1| = |R2| = 169.997$ mm

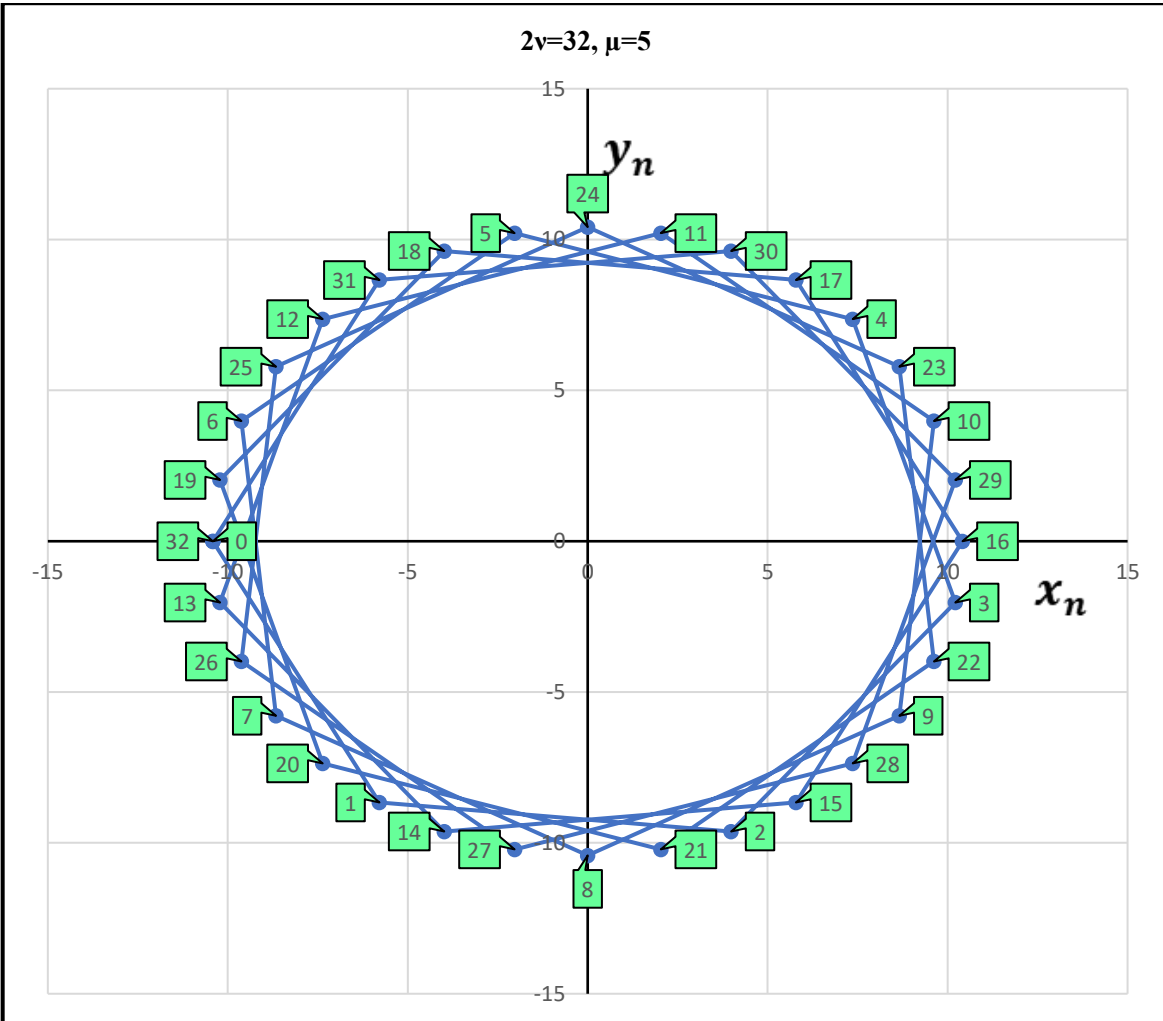


Figure 5.8 Interlaced multi-pass cavity and correspond (x_n, y_n) diagram plot.

Table 5.7 Interlaced multi-passes cavity 32 **(a)** corresponded (x_n, y_n) values **(b)** design parameters.

(a)

2ν	x_n	y_n
0	-10.41400	0
1	-5.78571	-8.658925
2	3.98527	-9.621281
3	10.21390	-2.031671
4	7.36381	7.36381
5	-2.03167	10.2139
6	-9.62128	3.985265
7	-8.65892	-5.785708
8	0.00000	-10.414
9	8.65892	-5.785708
10	9.62128	3.985265
11	2.03167	10.2139
12	-7.36381	7.36381
13	-10.21390	-2.031671
14	-3.98527	-9.621281
15	5.78571	-8.658925
16	10.41400	-6.38E-15
17	5.78571	8.658925
18	-3.98527	9.621281
19	-10.21390	2.031671
20	-7.36381	-7.36381
21	2.03167	-10.2139
22	9.62128	-3.985265
23	8.65892	5.785708
24	0.00000	10.414
25	-8.65892	5.785708
26	-9.62128	-3.985265
27	-2.03167	-10.2139
28	7.36381	-7.36381
29	10.21390	2.031671
30	3.98527	9.621281
31	-5.78571	8.658925
32	-10.41400	0.00000

(b)

$\nu =$	16
$\Theta(\text{rad})=$	0.981748
$\text{COS}(\Theta)$	0.55557
$d=$	75.552
$R=$	169.9976

Table 5.8 Comparison among three different interlaced cavities.

$\nu =$	2	3	16
μ	3	5	5
$\Theta(\text{rad})=$	4.7123	5.235988	0.981748
$\text{COS}(\Theta)$	0	0.500	0.55557
$L=$	75.55	75.55	75.55
$ R =$	75.5523	151.1046	169.9976141
$f=$	37.776	75.552	84.99881
f/L	0.5	1	1.125037
L/f	2	1	0.88886

5.5 Step by Step of Designing Absorbance Herriott's MPC

We will follow the Herriot approach for designing absorbance MPC spectrometer. From equation 5.16 we will assume that we have $2\nu = 32$ intercepts (or 30 bounces excluding the input and exit intercepts) and we choose arbitrary $\mu=5$ that will lead to $\Theta = 0.981735$ rad. From equation 5.4, we allocate that, the cavity length $L=75.55$, that leads to the mirror radii curvatures $R1=|R2|=170$ mm. For now, we also allocate the beam footprints semi-diameter $x_0 = r_0 = 10.414$ mm. In the following chapter we will describe how one can calculate the number of intercepts (bounces) and the beam footprints semi-diameter (r_0) that will be needed for any absorbance spectrometer.

We can now proceed to design a Herriott cell spectrometer. Firstly, the beam will be injected through hole on the back of M1 at coordinate location $(x_0, y_0) = (10.41, 0)$, in the other word, the beam will be injected at the back mirror semi-diameter location, but of course the mirrors will have extra few millimeters for mechanical semi-diameters to eliminate vignetting. Secondly, from

equation 5.6, 5.7 we calculate the stability factors G to ensure the stability of the cavity. Thirdly, we calculate aimed locations on M2 (x_1, y_1) . Fourthly, we calculate the first slope values and field of views for the first injected beam from (x'_0, y'_0) . Lastly, from equations 5.10 and 5.11 we calculate the repeated displacement values respectively then plot the ray path in (x_n, y_n) as viewed along the Z axis from behind M1. The first order design of HCMPCs is shown in table 5.10 and the repeated displacement values are shown in table 5.9 respectively.

Table 5.9 The displacement beam coordinates on front and back mirrors, respectively.

2v	x_n	y_n	2v	x_n	y_n
0	-10.414	0	1	-5.78570	-8.65892
2	3.985265	-9.62128	3	10.2138	-2.03167
4	7.36381	7.36381	5	-2.03167	10.2138
6	-9.62128	3.98526	7	-8.65892	-5.78570
8	-2.3E-14	-10.414	9	8.65892	-5.78570
10	9.621281	3.98526	11	2.03167	10.2138
12	-7.36381	7.36381	13	-10.2138	-2.03167
14	-3.98527	-9.62128	15	5.78570	-8.65892
16	10.414	-4.33E-14	17	5.78570	8.65892
18	-3.98527	9.621281	19	-10.2138	2.03167
20	-7.36381	-7.36381	21	2.03167	-10.2138
22	9.621281	-3.98526	23	8.65892	5.78570
24	6.6E-14	10.414	25	-8.65892	5.78570
26	-9.62128	-3.98526	27	-2.03167	-10.2138
28	7.36381	-7.36381	29	10.2138	2.03167
30	3.985265	9.62128	31	-5.78570	8.658924

Table 5.10 Description of first order design of Herriot cell.

Properties	Allocated Values	Calculated Values	Brief Description
μ		5	
2ν	32		Number of intercepts
(θ)		0.981735408 rad	$2\nu\theta = 2\mu\pi$
L	75.552 mm		Cavity length
ROC= R1 = R2		170.00 mm	$\cos\theta = 1 - \frac{L}{2f} = 1 - \frac{L}{R}$
G		0.555580457	$0 < \frac{L}{f} < 4$
x_0	-10.414 mm		Input beam location
y_0	0		Input beam location
Term1		0.534503231	$\sqrt{\frac{L}{4f-L}}$
x_1		-5.785814881	$x_1 = x_0 \cos(\theta) - y_0 \sin(\theta)$
y_1		-8.658853398	$y_1 = x_0 \sin(\theta) + y_0 \cos(\theta)$
(x'_0)		0.06125	$x'_0 = \frac{x_1 - x_0}{L}$ FOV=atan (0.06125)
(y'_0)		-0.114608	$y'_0 = \frac{y_1 - y_0}{L}$ FOV=atan (-0.114608)
(x_n)		✓	$x_n = x_0 \cos N\theta + \sqrt{\frac{L}{4f-L}} (x_0 + 2fx'_0) \sin N\theta$
(y_n)		✓	$y_n = y_0 \cos N\theta + \sqrt{\frac{L}{4f-L}} (y_0 + 2fy'_0) \sin N\theta$

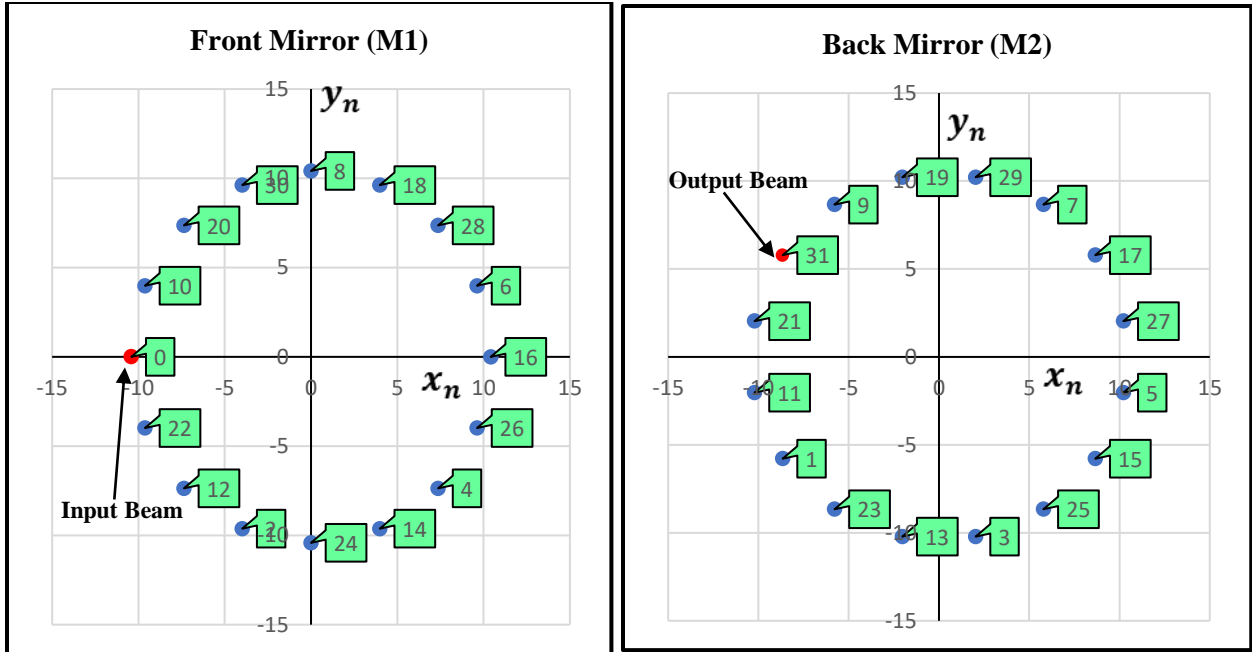


Figure 5.9 Layout of front and back mirrors beam bounces.

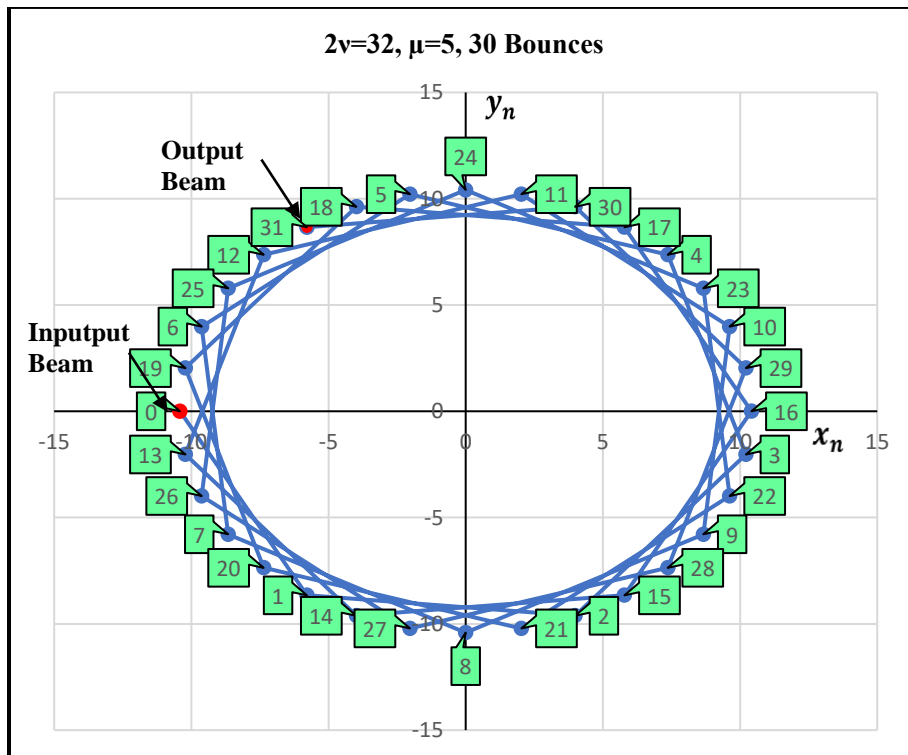


Figure 5.10 Layout of combined front and back mirrors beam bounces.

5.6 Using Ray Tracing Software (Zemax) to Analyze the Herriot Cell

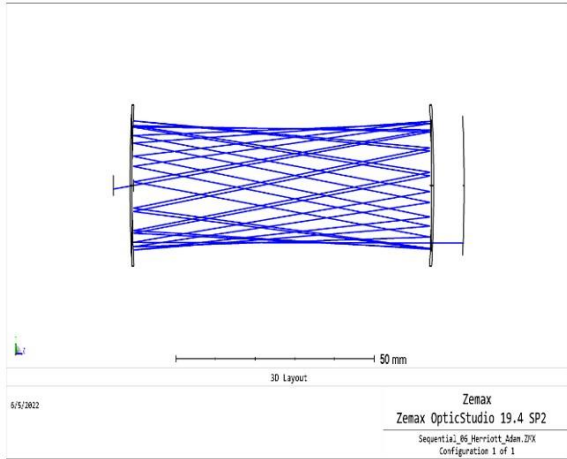
From table 5.11 we entered the first order solution into Zemax to confirm the Herriot cell design such as ROC and L. For now, we use the slope values to define the field of views (FOV) on x and y directions respectively as shown in equations 5.17 and 5.18, but in the following chapters we use $y\bar{y}$ equation to specify the field of views:

$$\text{FOV-X} = \text{atan}(0.061258031) = 3.53527^\circ \quad (5.17)$$

$$\text{FOV-Y} = \text{atan}(-0.114607409) = -6.59326^\circ. \quad (5.18)$$

We use the laser beam diameter as entrance pupil diameter =2mm (EPD=2mm) at the back of M1 then decentered the input collimated beam by $(x_0, y_0) = (-10.414, 0)$. In the following chapters we elaborate in detail how to calculate an exact entrance pupil diameter for plane wave or collimate light. So, in Herriott approach you can only design the system from gut ray. The Zemax first-order optical properties are shown in Fig5.11(b), where LaGrange or optical invariant of system (LINV), entrance pupil position (ENPP), entrance pupil diameter (EPDI), exit pupil position (EXPP), effective focal length (EFFL) and effective focal length for single element in the local plan y (EFLY). The real ray displacement data, FOV and EPD values are shown in Fig5.11(d). The inserted first order parameters such as ROC, L, decenter value are shown in Fig5.11(c).

(a)



(b)

Merit Function Editor

Wizards and Operands

Type		Target	Weight	Value	% Contrib
1	OOFF + Off-Axis				
2	LINV + 1	0.000	0.000	0.131	0.000
3	ENPP +	0.000	0.000	5.000	0.000
4	EPDI +	0.000	0.000	2.000	0.000
5	EXPP +	0.000	0.000	-1630.450	0.000
6	EXPD +	0.000	0.000	42.978	0.000
7	EFFL + 1	0.000	0.000	-76.505	0.000
8	EELY + 5	0.000	0.000	85.000	0.000

(c)

Surface 1 Properties

Configuration 1/1

Surface Type	Comment	Radius	Thickness	Material	Coating	Clear Semi-Dia	Chip Zone	Mech Semi-Dia	Conic	TCE x 1E-6	Par 1 (unused)	Par 2 (unused)	Par 4 (unused)	Par 5 (unused)	Par 6 (unused)
0	OBJECT	Standard	Infinity	Infinity		Infinity	0.000	Infinity	0.0...	0.000					
1	Standard	Standard	Infinity	5.000		1.655	0.000	1.655	0.0...	0.000					
2	STOP	Standard	Infinity	0.000		1.000	0.000	1.000	0.0...	0.000					
3	Coordinate Break	Standard	-0.319			0.000					-10.414	0.0	0.0	0.000	0.000
4	(aper)	Standard	Infinity	75.552		13.000	U	0.000	13.000	0.0...					
5	(aper)	Standard	1	-170.0...	-75.552	MIRROR		13.000	U	0.000					
6	(aper)	Standard	2	170.000	75.552	MIRROR		13.000	U	0.000					
7	(aper)	Standard	3	-170.0...	P	-75.552	P	MIRROR		13.000	U	0.000			
8	(aper)	Standard	4	170.000	P	75.552	P	MIRROR		13.000	U	0.000			
9	(aper)	Standard	5	-170.0...	P	-75.552	P	MIRROR		13.000	U	0.000			
10	(aper)	Standard	6	170.000	P	75.552	P	MIRROR		13.000	U	0.000			
11	(aper)	Standard	7	-170.0...	P	-75.552	P	MIRROR		13.000	U	0.000			
12	(aper)	Standard	8	170.000	P	75.552	P	MIRROR		13.000	U	0.000			
13	(aper)	Standard	9	-170.0...	P	-75.552	P	MIRROR		13.000	U	0.000			
14	(aper)	Standard	10	170.000	P	75.552	P	MIRROR		13.000	U	0.000			
15	(aper)	Standard	11	-170.0...	P	-75.552	P	MIRROR		13.000	U	0.000			
16	(aper)	Standard	12	170.000	P	75.552	P	MIRROR		13.000	U	0.000			
17	(aper)	Standard	13	-170.0...	P	-75.552	P	MIRROR		13.000	U	0.000			
18	(aper)	Standard	14	170.000	P	75.552	P	MIRROR		13.000	U	0.000			
19	(aper)	Standard	15	-170.0...	P	-75.552	P	MIRROR		13.000	U	0.000			
20	(aper)	Standard	16	170.000	P	75.552	P	MIRROR		13.000	U	0.000			
21	(aper)	Standard	17	-170.0...	P	-75.552	P	MIRROR		13.000	U	0.000			
22	(aper)	Standard	18	170.000	P	75.552	P	MIRROR		13.000	U	0.000			
23	(aper)	Standard	19	-170.0...	P	-75.552	P	MIRROR		13.000	U	0.000			
24	(aper)	Standard	20	170.000	P	75.552	P	MIRROR		13.000	U	0.000			
25	(aper)	Standard	21	-170.0...	P	-75.552	P	MIRROR		13.000	U	0.000			
26	(aper)	Standard	22	170.000	P	75.552	P	MIRROR		13.000	U	0.000			
27	(aper)	Standard	23	-170.0...	P	-75.552	P	MIRROR		13.000	U	0.000			
28	(aper)	Standard	24	170.000	P	75.552	P	MIRROR		13.000	U	0.000			
29	(aper)	Standard	25	-170.0...	P	-75.552	P	MIRROR		13.000	U	0.000			
30	(aper)	Standard	26	170.000	P	75.552	P	MIRROR		13.000	U	0.000			
31	(aper)	Standard	27	-170.0...	P	-75.552	P	MIRROR		13.000	U	0.000			
32	(aper)	Standard	28	170.000	P	75.552	P	MIRROR		13.000	U	0.000			
33	(aper)	Standard	29	-170.0...	P	-75.552	P	MIRROR		13.000	U	0.000			
34	(aper)	Standard	30	170.000	P	75.552	P	MIRROR		13.000	U	0.000			
35	Standard	Standard	Infinity	0.000		10.641	0.000	10.641	0.0...	0.000					
36	Standard	Standard	Infinity	8.225		10.641	0.000	10.641	0.0...	0.000					
37	IMAGE	Standard	-178.2...			11.265	0.000	11.265	0.0...	0.000					

(d)

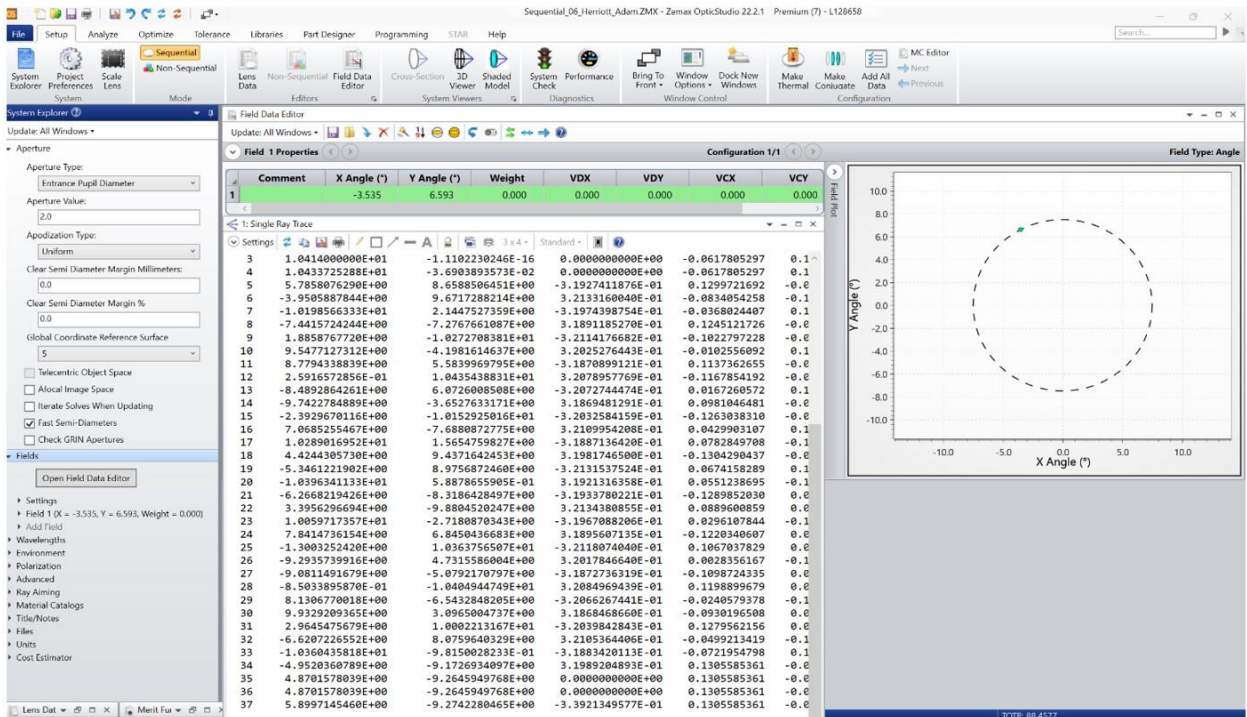


Figure 5.11 (a) Layout of gut ray Herriot cell design in Zemax (b) merit function (c) lens data editor (d) Zemax real ray tracing, FOV and EPD [7].

In the design shown in Fig 5.11, the real ray solution closely matches the first order Herriot cell displacements coordinate data (x_n, y_n) , but there are discrepancies among HCMPC first order, first order Zemax and paraxial optics Zemax, such as LaGrange invariant and EPD. These discrepancies come from several sources:

1. The M1 and M2 surfaces are spherical not flat as assumed in paraxial optics, which alters the real ray transfer distance, the local slope of the surface and aberrations. We will discuss the aberration impacts in detail in the following chapters.
2. HCMPC approach the input beam is a gut ray (object of finite conjugate), but in Zemax design the input beam is collimated (object of infinite conjugate object).

3. The HCMPC entrance pupil diameter is the mirror diameter=20.8mm, but in Zemax the EPD=2 mm, consequently, that will lead to deviation in LaGrange invariant for both designs.

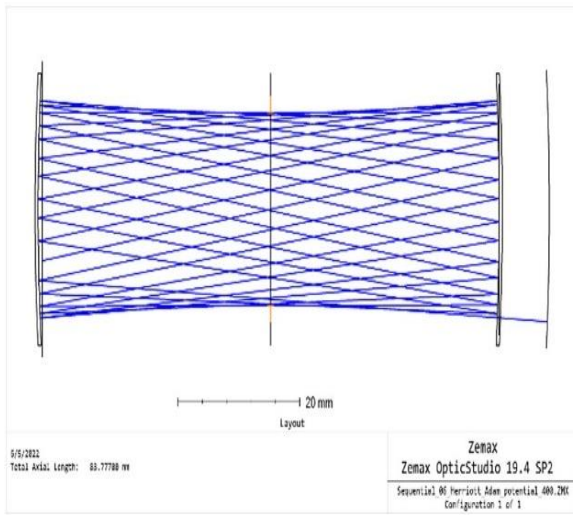
We found out that to make the HCMPC approach first order solution and first order solution for Zemax sufficiently identical the following procedures will be needed:

1. Rotate HCMPC displacements values (x_n, y_n) by the slope of the first segment, as shown in Fig5.12 and Fig5.13
2. Calculate a new entrance pupil diameter for rotated HCMPC design, by way explanation, $EPD(\text{collimated}) = 2y_n(\text{rotated})$, as shown in Fig5.14
3. Calculate a new FOV for the rotated HCMPC design, by way explanation, the new FOV only in y-coordinate instead of x-coordinate and y-coordinate,

$$FOV(\text{collimated}) = \sqrt{(FOV_X)^2 + (FOV_Y)^2} = \sqrt{(3.53527)^2 + (-6.59326)^2} = 7.481^\circ.$$

4. Calculate the first order parameter for rotated HCMPC, such as, EPD, EFL, radius of curvature and LaGrange invariant.
5. Insert the new collimated EPD and FOV into ZEMAX, without changing any other parameters.
6. Compare the Zemax design with rotated HCMPC design, such as, LaGrange invariant and $y\bar{y}$ diagram, as shown in Fig5.15.
7. After these procedures, the rotated HCMPC design and collimated input Zemax design are sufficiently identical results.

(a)



(b)

Merit Function Editor

Wizards and Operands Merit Function: 0

Type	Surf1	Surf2	Target	Weight	Value	% Contrib
1 LINV		1	0.000...	0.0000...	1.203632	0.000000
2 ENPP			0.000...	0.0000...	37.459000	0.000000
3 EPDI			0.000...	0.0000...	18.368712	0.000000
4 EFLY	5	5	0.000...	0.0000...	85.000000	0.000000

(c)

Lens Data

Update: All Windows

Surface 4 Properties Configuration 1/1

	Surface Type	Comment	Radius	Thickness	Material	Coating	Semi-Diameter	Chip Zone	Mech Semi-Dia	Conic	TCE x 1E-6
0	OBJECT	Standard	Infinity	Infinity			Infinity	0.000	Infinity	0.0...	0.000
1	Standard		Infinity	37.459			14.093	0.000	14.093	0.0...	0.000
2	STOP	Standard	Infinity	0.000			9.184	0.000	9.184	0.0...	0.000
3	Standard		Infinity	0.000			9.184	0.000	9.184	0.0...	0.000
4	(aper)	Standard	Infinity	37.459			13.000 U	0.000	13.000	0.0...	0.000
5	(aper)	Standard	1 -170.0...	-75.552	MIRROR		13.000 U	0.000	13.000	0.0...	0.000
6	(aper)	Standard	2 170.000	75.552	MIRROR		13.000 U	0.000	13.000	0.0...	0.000
7	(aper)	Standard	3 -170.0... P	-75.552	P MIRROR		13.000 U	0.000	13.000	0.0...	0.000
8	(aper)	Standard	4 170.000 P	75.552	P MIRROR		13.000 U	0.000	13.000	0.0...	0.000
9	(aper)	Standard	5 -170.0... P	-75.552	P MIRROR		13.000 U	0.000	13.000	0.0...	0.000
10	(aper)	Standard	6 170.000 P	75.552	P MIRROR		13.000 U	0.000	13.000	0.0...	0.000
11	(aper)	Standard	7 -170.0... P	-75.552	P MIRROR		13.000 U	0.000	13.000	0.0...	0.000
12	(aper)	Standard	8 170.000 P	75.552	P MIRROR		13.000 U	0.000	13.000	0.0...	0.000
13	(aper)	Standard	9 -170.0... P	-75.552	P MIRROR		13.000 U	0.000	13.000	0.0...	0.000
14	(aper)	Standard	10 170.000 P	75.552	P MIRROR		13.000 U	0.000	13.000	0.0...	0.000
15	(aper)	Standard	11 -170.0... P	-75.552	P MIRROR		13.000 U	0.000	13.000	0.0...	0.000
16	(aper)	Standard	12 170.000 P	75.552	P MIRROR		13.000 U	0.000	13.000	0.0...	0.000
17	(aper)	Standard	13 -170.0... P	-75.552	P MIRROR		13.000 U	0.000	13.000	0.0...	0.000
18	(aper)	Standard	14 170.000 P	75.552	P MIRROR		13.000 U	0.000	13.000	0.0...	0.000
19	(aper)	Standard	15 -170.0... P	-75.552	P MIRROR		13.000 U	0.000	13.000	0.0...	0.000
20	(aper)	Standard	16 170.000 P	75.552	P MIRROR		13.000 U	0.000	13.000	0.0...	0.000
21	(aper)	Standard	17 -170.0... P	-75.552	P MIRROR		13.000 U	0.000	13.000	0.0...	0.000
22	(aper)	Standard	18 170.000 P	75.552	P MIRROR		13.000 U	0.000	13.000	0.0...	0.000
23	(aper)	Standard	19 -170.0... P	-75.552	P MIRROR		13.000 U	0.000	13.000	0.0...	0.000
24	(aper)	Standard	20 170.000 P	75.552	P MIRROR		13.000 U	0.000	13.000	0.0...	0.000
25	(aper)	Standard	21 -170.0... P	-75.552	P MIRROR		13.000 U	0.000	13.000	0.0...	0.000
26	(aper)	Standard	22 170.000 P	75.552	P MIRROR		13.000 U	0.000	13.000	0.0...	0.000
27	(aper)	Standard	23 -170.0... P	-75.552	P MIRROR		13.000 U	0.000	13.000	0.0...	0.000
28	(aper)	Standard	24 170.000 P	75.552	P MIRROR		13.000 U	0.000	13.000	0.0...	0.000
29	(aper)	Standard	25 -170.0... P	-75.552	P MIRROR		13.000 U	0.000	13.000	0.0...	0.000
30	(aper)	Standard	26 170.000 P	75.552	P MIRROR		13.000 U	0.000	13.000	0.0...	0.000
31	(aper)	Standard	27 -170.0... P	-75.552	P MIRROR		13.000 U	0.000	13.000	0.0...	0.000
32	(aper)	Standard	28 170.000 P	75.552	P MIRROR		13.000 U	0.000	13.000	0.0...	0.000
33	(aper)	Standard	29 -170.0... P	-75.552	P MIRROR		13.000 U	0.000	13.000	0.0...	0.000
34	(aper)	Standard	30 170.000 P	75.552	P MIRROR		13.000 U	0.000	13.000	0.0...	0.000
35	Standard		Infinity	0.000			12.008	0.000	12.008	0.0...	0.000
36	Standard		Infinity	8.225			12.008	0.000	12.008	0.0...	0.000
37	IMAGE	Standard	-178.2				13.303	0.000	13.303	0.0...	0.000

(d)

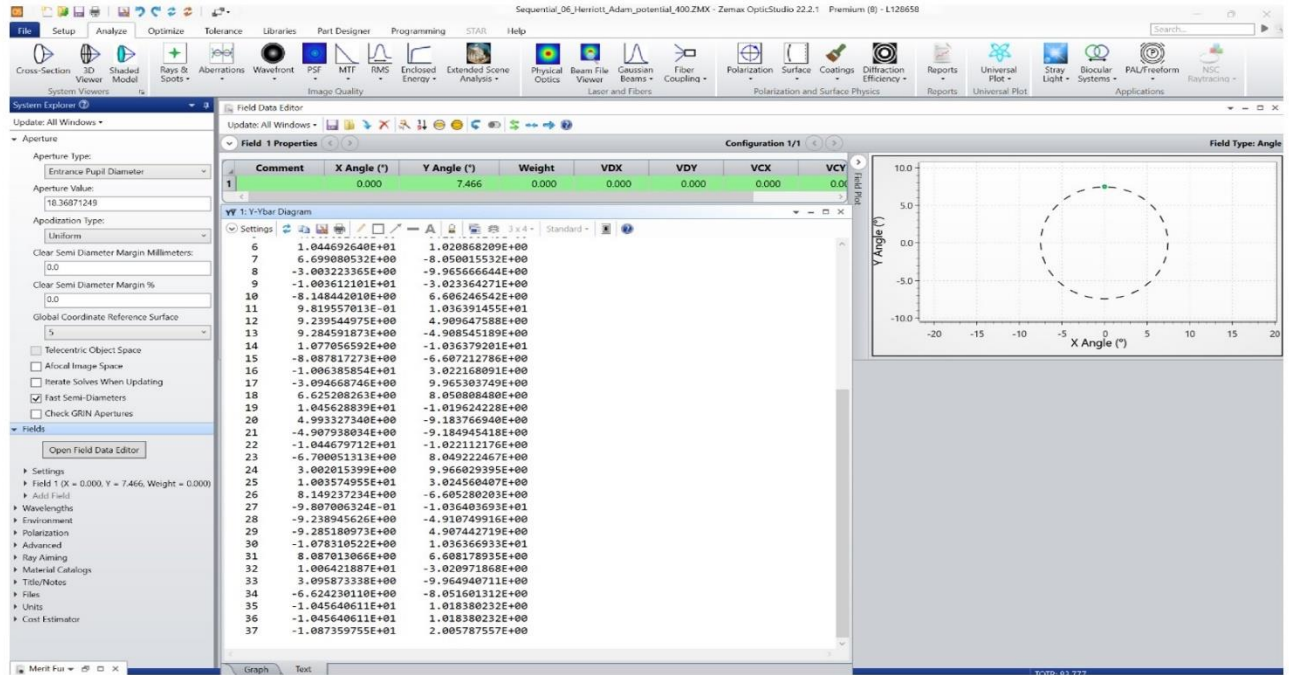


Figure 5.12 (a) Layout of Herriot collimated input design in Zemax (b) merit function (c) lens data editor (d) Paraxial real ray tracing, FOV and EPD [7].

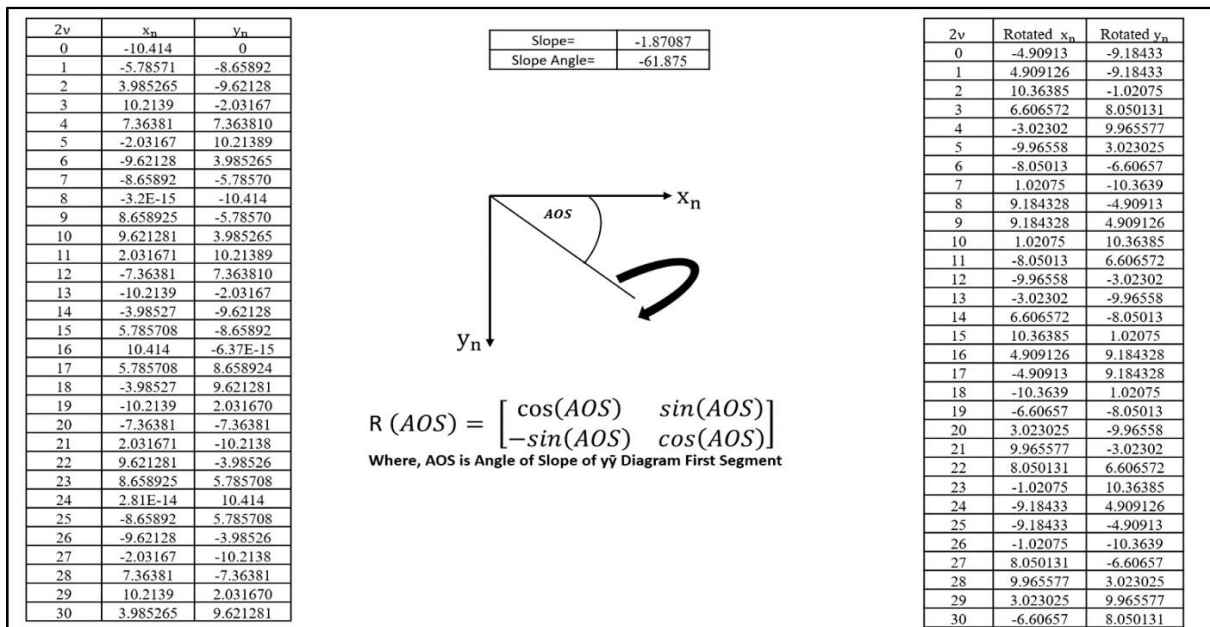


Figure 5.13 An image of rotated gut ray real solution to be matched with the Zemax collimated design.

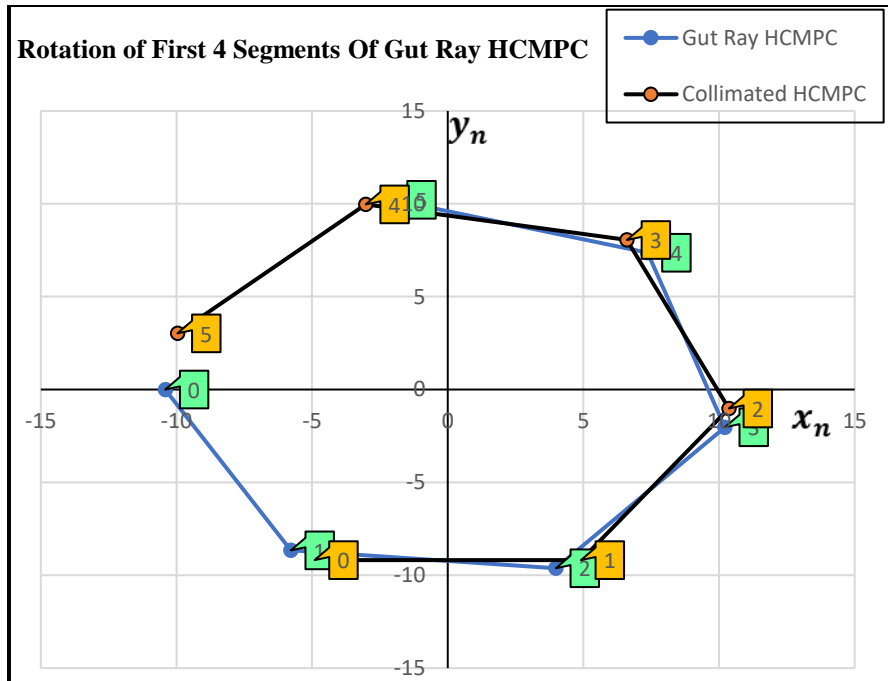


Figure 5.14 Shows the Rotation of the gut ray (green) to facilitate the collimated ray (orange).

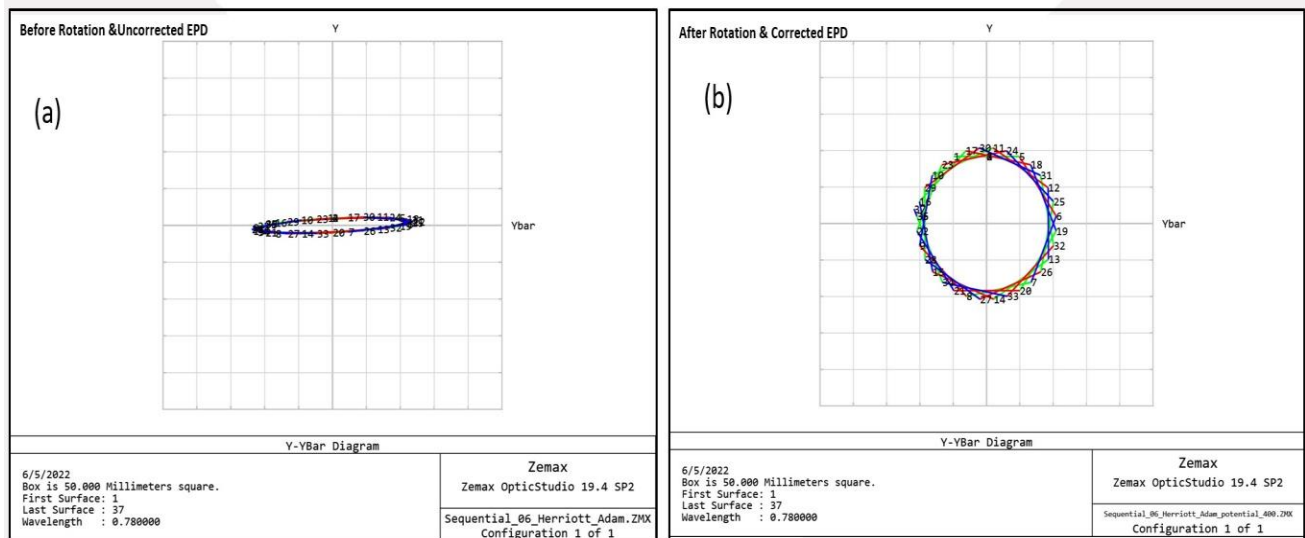


Figure 5.15 (a) The $y\bar{y}$ diagram of collimated input design, (b) The $y\bar{y}$ diagram of gut ray design [7].

In the following chapter we create a new equation to collimate input HCMPC with examples. An image of HCMPC programmed in Excel is shown in Appendix C.

5.7 Using the (x_n, y_n) Values as $y\bar{y}$ Values to Design First Order Herriott Cell

From section 5.6 the rotated HCMPC displacement values (x_n, y_n) and collimated Zemax $y\bar{y}$ diagram are sufficiently identical results.

Thus, we used the displacement value $(x_n, y_n) = (\bar{y}_n, y_n)$ and from table 2.1 we use the $y\bar{y}$ characterization to calculate the first order optical parameters. The results are sufficiently identical results with HCMPC approach, as shown in table 5.11 and table 5.12. As expected, we noticed the LaGrange invariant has negative sign and the explanation is the counterclockwise sense of θ .

Table 5.11 Deploy the displacement (x_n, y_n) values as initial $y\bar{y}$ value description.

Properties	Known Values	Calculated Values	Brief Description
$\bar{y}_n = x_n$	✓		Displacement in x direction(x_n)
$y = y_n$	✓		Displacement in y direction(y_n)
Length (L)	75.5523 mm		Axial distance between represented by two points in the $y\bar{y}$ diagram
Lg		-1.1935263	LaGrange invariant or the scaling factor $Lg = \frac{1}{t} \begin{bmatrix} y_n & \bar{y}_n \\ y_{n+1} & \bar{y}_{n+1} \end{bmatrix}$
u		✓	Marginal ray angle $U = \frac{y_{n+1} - y_n}{t}$
\bar{u}		✓	Chief ray angle $\bar{U} = \frac{\bar{y}_{n+1} - \bar{y}_n}{t}$
Φ_1		0.0117646 diopters	Optical power for back mirror $\Phi_1 = \frac{1}{Lg} \begin{bmatrix} un & \bar{u}_n \\ un+1 & \bar{u}_{n+1} \end{bmatrix}$
Φ_2		-0.0117646 diopters	Optical power for front mirror $\Phi_2 = -\Phi_1$
f_1		85.00076 mm	Focal length for back mirror $f_1 = \frac{1}{\Phi_1}$
f_2		-85.00076 mm	Focal length for front mirror $f_2 = \frac{1}{\Phi_2}$
R_1		-170.002 mm	Radius of curvature of back mirror $R_1 = \frac{-2n}{\Phi_1}$
R_2		170.002 mm	Radius of curvature of front mirror $R_2 = -R_1$

Table 5.12 Results of deploy the displacement values as initial \bar{y} values.

N	\bar{Y}	y	n	L	u	\bar{u}	R1	$\Phi 1=\Phi 2$	$1/\Phi 1=f1$
0	10.414	0	1	75.552	0.11461				
1	5.785815	8.658853	1	75.552	0.11461	-0.0613	-170.0015	0.0117646	85.000762
2	-3.98503	9.621379	1	75.552	0.01274	-0.1293	-170.0015	0.0117646	85.000762
3	-10.2138	2.032047	1	75.552	-0.1005	-0.0824	-170.0015	0.0117646	85.000762
4	-7.36417	-7.36345	1	75.552	-0.1244	0.03772	-170.0015	0.0117646	85.000762
5	2.031043	-10.214	1	75.552	-0.0377	0.12435	-170.0015	0.0117646	85.000762
6	9.620987	-3.98598	1	75.552	0.08243	0.10046	-170.0015	0.0117646	85.000762
7	8.659423	5.784963	1	75.552	0.12933	-0.0127	-170.0015	0.0117646	85.000762
8	0.001024	10.414	1	75.552	0.06127	-0.1146	-170.0015	0.0117646	85.000762
9	-8.65828	5.786667	1	75.552	-0.0612	-0.1146	-170.0015	0.0117646	85.000762
10	-9.62177	-3.98408	1	75.552	-0.1293	-0.0128	-170.0015	0.0117646	85.000762
11	-2.03305	-10.2136	1	75.552	-0.0825	0.10044	-170.0015	0.0117646	85.000762
12	7.362723	-7.3649	1	75.552	0.03771	0.12436	-170.0015	0.0117646	85.000762
13	10.21422	2.030038	1	75.552	0.12435	0.03774	-170.0015	0.0117646	85.000762
14	3.986922	9.620595	1	75.552	0.10047	-0.0824	-170.0015	0.0117646	85.000762
15	-5.78411	8.659992	1	75.552	-0.0127	-0.1293	-170.0015	0.0117646	85.000762
16	-10.414	0.002049	1	75.552	-0.1146	-0.0613	-170.0015	0.0117646	85.000762
17	-5.78752	-8.65771	1	75.552	-0.1146	0.06124	-170.0015	0.0117646	85.000762
18	3.983136	-9.62216	1	75.552	-0.0128	0.12932	-170.0015	0.0117646	85.000762
19	10.21342	-2.03406	1	75.552	0.10044	0.08246	-170.0015	0.0117646	85.000762
20	7.365621	7.361999	1	75.552	0.12437	-0.0377	-170.0015	0.0117646	85.000762
21	-2.02903	10.21442	1	75.552	0.03775	-0.1243	-170.0015	0.0117646	85.000762
22	-9.6202	3.987868	1	75.552	-0.0824	-0.1005	-170.0015	0.0117646	85.000762
23	-8.66056	-5.78326	1	75.552	-0.1293	0.0127	-170.0015	0.0117646	85.000762
24	-0.00307	-10.414	1	75.552	-0.0613	0.11459	-170.0015	0.0117646	85.000762
25	8.657146	-5.78837	1	75.552	0.06122	0.11463	-170.0015	0.0117646	85.000762
26	9.622555	3.982189	1	75.552	0.12932	0.01278	-170.0015	0.0117646	85.000762
27	2.035062	10.21322	1	75.552	0.08247	-0.1004	-170.0015	0.0117646	85.000762
28	-7.36127	7.366345	1	75.552	-0.0377	-0.1244	-170.0015	0.0117646	85.000762
29	-10.2146	-2.02803	1	75.552	-0.1243	-0.0378	-170.0015	0.0117646	85.000762
30	-3.98881	-9.61981	1	75.552	-0.1005	0.0824	-170.0015	0.0117646	85.000762
31	5.782407	-8.66113	1	0	0.01269	0.12933		0	0

Chapter 6.

6.1 The MPC $y\bar{y}$ Diagram Methodology Introduction

The $y\bar{y}$ diagram is a representation of geometrical paraxial optics, developed by Delano [9] then extended and employed by others to design and analyze gaussian beams propagating through optical systems [24][38] [39]. The $y\bar{y}$ diagram is a plot of the paraxial chief and marginal ray heights at each surface as they are sequentially encountered through the optical system, with a scaling factor defined by the LaGrange invariant (Lg) of the system. It can be described as observing a skew ray propagating through an optical system as viewed along the optical axis. With simple relations to connect individual and pairs of (\bar{y}, y) points to optical specifications, the designer can readily calculate ray angles, beam sizes, distances, focal lengths and principal locations. Additionally, simple graphical rules allow the designer to rapidly layout or evaluate optical conditions throughout a system, including locating and determining the sizes of all pupils and images, telecentric, plane wave and collimated spaces and evaluating distances, as shown in Chapter 2.

We felt that Herriott's design approach, though sufficient, obscured how one would design a system from the first principles from the perspective of an optical designer. We also found that Herriott's didn't present a methodology to calculate some of critical design aspects such as the radial distance, r_0 , that defines the circle of the beam footprints. The variable r_0 is equivalent

to Herriott's $r_0 = A = B = \sqrt{x_0^2 + y_0^2} = \sqrt{x_n^2 + y_n^2}$ for circular beam footprint on the mirrors.

From Chapter 5, we also saw that Herriott's MPC gut ray design approach deviates from paraxial optics and some of the parameters of first order ray tracing software results such as entrance pupil diameter and LaGrange invariant. If we treat $(x_n, y_n) = (\bar{y}, y)$ in the diagrams Figure 5.10 we see that every mirror is positive powered (the segments "bend" towards the coordinate origin), every mirror is separated by the same distance (the area swept out by a vector whose base is at the origin from element N to element N+1 is identical) and the radial distance of the spots from the mirror center is identical. In case of Herriott's MPC injected gut ray approach, once the LaGrange Invariant (Lg) is properly set to match the mirror separations and powers, note that this case the $\bar{y}y$ diagram itself does not precisely represent the Herriot's MPC ray tracing software design. The entrance pupil diameter represented by the $\bar{y}y$ diagram is nearly the diameter of the circle of dots, but the probing beam is generally far smaller. Thus, the $(x_n, y_n) = (\bar{y}, y)$ diagram is essential plot of gut ray of the probing beam and it allows the designer to optimize and analysis the design and after that the designer needs to fix the data to be correlated with geometrical optics convention signs. And rotate the design to collimated injected beam to compute accurate values of entrance pupil diameter and the LaGrange Invariant, as shown in the previous chapter. In the following chapter, we will show how 3rd order aberration calculations can be made with this approach.

In this chapter, firstly we define all parameters needed to lay out any MPC absorbance spectrometer such as the clear aperture semi-diameter r_0 , number of mirrors intercepts (N), the angles among the bounces Θ_m and the K_m parameter (the numbers of $\bar{y}y$ circular rotation (2π) rotation) and cavity length. Secondly, we create intuitive $\bar{y}y$ diagram equations that correlate with geometrical optics sign convention (rays propagate from left to right and ray angles are positive if

the ray direction is obtained by rotating about the +z axis counterclockwise) for MPC gut ray design instead of Herriott's MPC Eqn.5.10 and Eqn.5.11 respectively. Thirdly we create the $y\bar{y}$ diagram of collimated input of MPC for further analysis. Fourthly, we create equations of MPC of different radii of curvature, Lastly, the chapter will include numerous step-by-step numerical examples using first order $y\bar{y}$ approach and compared with ray tracing software (ZEMAX).

The creation of collimated input beam $y\bar{y}$ diagram equations to MPC will help the designer to readily use the ray tracing software and obtain precise analysis of aberrations, tolerate, an accurate values of entrance pupil diameter and LaGrange. Using the ray tracing software is an essential tool to analyze, tolerate and obtain as build MPC model.

6.2 Defining MPC Absorbance Parameters

The optical designer is presented with a set of specifications for the system. First, the science of the spectroscopic task will yield a minimum path length through which the laser probe must pass, the overall length (OAL). Mechanical criteria for the packaging yield the maximum length into which the system must fit, which yields a mirror separation, L. This sets the minimum number of integer passes the probe beam must make through the cell, $N \geq OAL/L$, which requires $N+1$ points on the $y\bar{y}$ diagram, $n = 0 \dots N$. One, $n=0$, is for the beam entering (\bar{y}_0, y_0) and the last, $n = N$, (\bar{y}_{31}, y_{31}) is for exiting the cavity, both of which are located at the respective mirrors. Note that there may be additional packaging requirements that increase N. For example, if the detector needs to be on the opposite side as the source, in our approach N must be odd and greater than OAL/L . And finally, our N is related to Herriott's v by $N = 2v - 1$ for odd N and $N = 2v$ for even N.

In other words, the input pass (\bar{y}_0, y_0) is for the beam entering and (\bar{y}_{31}, y_{31}) is for exiting the cavity, both of which are located at the respective mirrors, or the even numbered intersection

points will be the point where the ray strikes (intercept) the one mirror and the odd numbered points will correspond to the points of impact on the other mirror. In addition, that designer obtains a 1:1 image of the input spot at (\bar{y}_{32}, y_{32}) and inverted image after at (\bar{y}_{16}, y_{16}) for concave mirrors. And the encircled energy does not degenerate as the beams bounce back and forth between the mirrors but is continuously refocused by the concave MPC mirrors. These concepts allow the designer to choose an accurate location of input beam locations and output beam location (detector) for any absorbance MPC design and correlate with HCMPC approach.

Now that N has been defined, we now note that the probe beam has some diameter, D and to ensure that beam footprints do not overlap, we set:

$$2\pi r_0 \geq (N + 1)D \quad \& \quad r_0 \geq \frac{(N+1)D}{2\pi}. \quad (6.1)$$

Given this parameter, the ring of beams does not overlap one another, which is important at the source and detector locations as the designer wants to avoid feedback into the source and stray beams onto the detector as those beams will have traveled different distances through the cell, as illustrated on Figure 6.1.

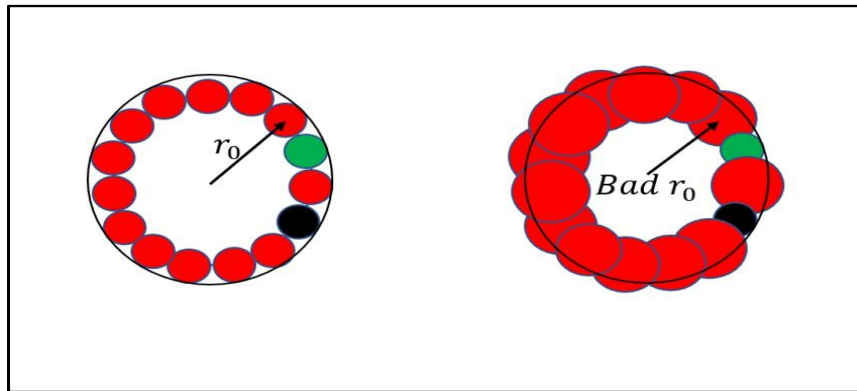


Figure 6.1 a) Correct size of mirror semi-diameter for absorbance spectrometer **Mirror b)** Undersized mirror semi-diameter for absorbance spectrometer.

For an example, assume a system requires a spectroscopic path length $\geq 2282\text{mm}$ in a package 75.55mm in length between the mirrors and the detector. Also assume the Laser source has a 4.8mm diameter beam and it must be on the opposite side of the cell from the detector. This requires $OAL/L = 2282/75.55 = 30.21$ passes, so we select $N=31$, which is an odd number ensuring the detector and source are on opposite sides of the cell. From equations 6.1, we find that $r_0 \geq 32*4.8/(2\pi) = 24.45\text{mm}$ so we select minimum value $r_0 = 25\text{mm}$.

6.3 The $y\bar{y}$ Diagram Methodology of Gut Ray with Numerical Example

We choose to plot the $y\bar{y}$ diagram MPC in a clockwise sense to follow geometrical optics convention signs, so, we create gut ray MPC $y\bar{y}$ diagram baseline equations as shown in equations 6.2 and 6.3, where $n=0$ to $N=31$:

$$\bar{y}_n = -r_0 \cos(-n\Theta m), \quad (6.2)$$

$$y_n = -r_0 \sin(-n\Theta m). \quad (6.3)$$

Then we define a new parameter, K_m , which is related to the number of times the mirror intercepts circle around the cell, in other words, the number of times the $y\bar{y}$ diagram mirror intercepts circle around (2π) the cell. To avoid ambiguity, we change from Herriott's notion of μ to m . The parameter K_m also ensures that the beams are evenly spaced on the mirrors:

$$K_m = \frac{m(2v-1)}{2v} = \frac{m(N)}{N+1}. \quad (6.4)$$

Then we calculate Θm between two sequence bounces as

$$\Theta m = \frac{2\pi K_m}{N} = \frac{2\pi m}{N+1}. \quad (6.5)$$

From section 6.2 and section 6.3 we have all the parameters and equation required to completely design gut ray $y\bar{y}$ diagram MPC absorbance spectrometer, which is programmed in Excel.

6.4 Consecutive $y\bar{y}$ Diagram Gut Ray Design of MPC Absorbance Spectrometer

From section 6.2 we can proceed to design the consecutive $y\bar{y}$ diagram for absorbance spectrometer application. Firstly, the beam will be injected through the back of M1 as calculated from section 6.2, $(\bar{y}_0, y_0) = (25, 0)$ and calculated intercepts (passes) $N=31$. Secondly, from equation 6.4 and 6.5 the angle Θ_m between bounces for consecutive design can be calculated $m=1$ as:

$$K_m = \frac{(N)}{N+1},$$

$$\Theta_m = \frac{2\pi}{N+1}.$$

Thirdly, from equations 6.2 and 6.3 the points on the $y\bar{y}$ diagram will fall on a circle of calculated radius r_0 , in other words, we can assign \bar{y} and y to cosine and sine functions, respectively, where the arguments will entail increments in angular steps. Fourthly, the radius of curvature, g_1g_2 parameter and stability, EFL, can be calculated from the $y\bar{y}$ diagram characterization (Chapter2, table 2.21). Lastly, we plotted the repeated skew ray $y\bar{y}$ values and as viewed along the Z axis from behind M1. The first order design of the consecutive $y\bar{y}$ diagram MPCs are shown in table 6.1, table 6.2 and the repeated $y\bar{y}$ diagram values is shown in Figure 6.2, Figure 6.3 respectively and an image of programmed Excel file attached on Appendix D.

Table 6.1 Description of First Order Consecutive gut ray \bar{y} Diagram MPC.

Properties	Allocated Values	Calculated Values	Brief Description
m	1		
r_0		-25mm	$r_0 \geq \frac{(N+1)D}{2\pi}$
Number of intercepts (N)		31	$N=OAL/L$
θ_m		0.196350	$\theta_m = \frac{2\pi Km}{N} = \frac{2\pi m}{N+1}$
\bar{y}_0		-25	Input beam location $\bar{y}_0 = r_0 \cos(-n\theta_m)$
y_0		0	Input beam location $y_0 = r_0 \sin(-n\theta_m)$
\bar{y}_n		√	$\bar{y}_n = r_0 \cos(-n\theta_m)$ From n=0 to N=31
y_n		√	$y_n = r_0 \sin(-n\theta_m)$ From n=0 to N=31
Length (L)		75.552 mm	Cavity length $t_1 = \frac{1}{Lg} \begin{bmatrix} y_0 & \bar{y}_0 \\ y_l & \bar{y}_l \end{bmatrix}$
\bar{U} (rad)		0.00635	$\bar{U} = \frac{\bar{y}_{i+1} - \bar{y}_i}{t_1}$
U(Rad)		0.064555	$U = \frac{y_{i+1} - y_i}{t_1}$
R		3931.98556	$\Phi = \frac{1}{Lg} \begin{bmatrix} u_0 & \bar{u}_0 \\ u_l & \bar{u}_l \end{bmatrix}$
$\frac{L}{f}$ (Stability)		0.038429	$0 \leq \frac{L}{f} \leq 4$
FOV (Y-direction)		-3.693°	FOV_X=atan (U)
FOV (X-direction)		0.364°	FOV_Y=atan (\bar{U})

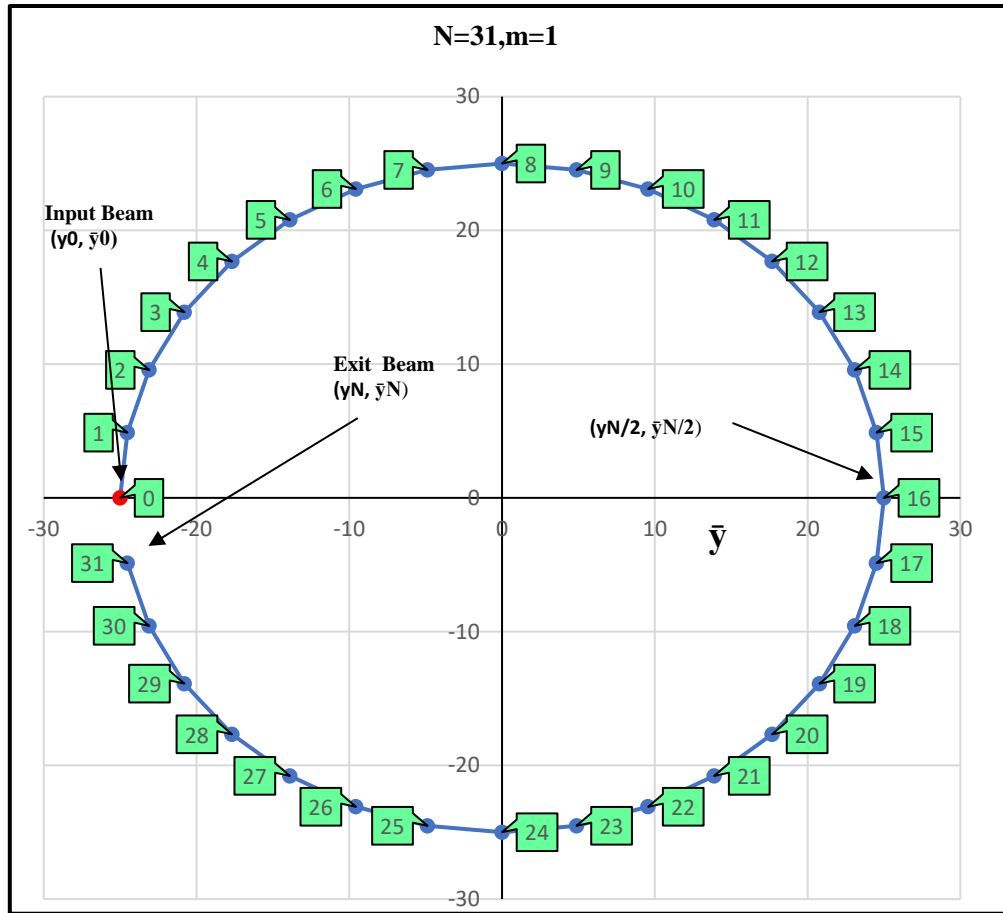


Figure 6.2 Consecutive gut ray $\bar{y}\bar{y}$ diagram MPC.

Table 6.2 Consecutive gut ray $y\bar{y}$ diagram MPC.

N	\bar{y}	y
0	-25.00000	0
2	-23.09699	9.567086
4	-17.67767	17.67767
6	-9.56709	23.09699
8	0.00000	25
10	9.56709	23.09699
12	17.67767	17.67767
14	23.09699	9.567086
16	25.00000	3.06E-15
18	23.09699	-9.567086
20	17.67767	-17.67767
22	9.56709	-23.09699
24	0.00000	-25
26	-9.56709	-23.09699
28	-17.67767	-17.67767
30	-23.09699	-9.567086

N	\bar{y}	y
1	-24.51963	4.877258
3	-20.78674	13.88926
5	-13.88926	20.78674
7	-4.87726	24.51963
9	4.87726	24.51963
11	13.88926	20.78674
13	20.78674	13.88926
15	24.51963	4.877258
17	24.51963	-4.87726
19	20.78674	-13.8893
21	13.88926	-20.7867
23	4.87726	-24.5196
25	-4.87726	-24.5196
27	-13.88926	-20.7867
29	-20.78674	-13.8893
31	-24.51963	-4.87726

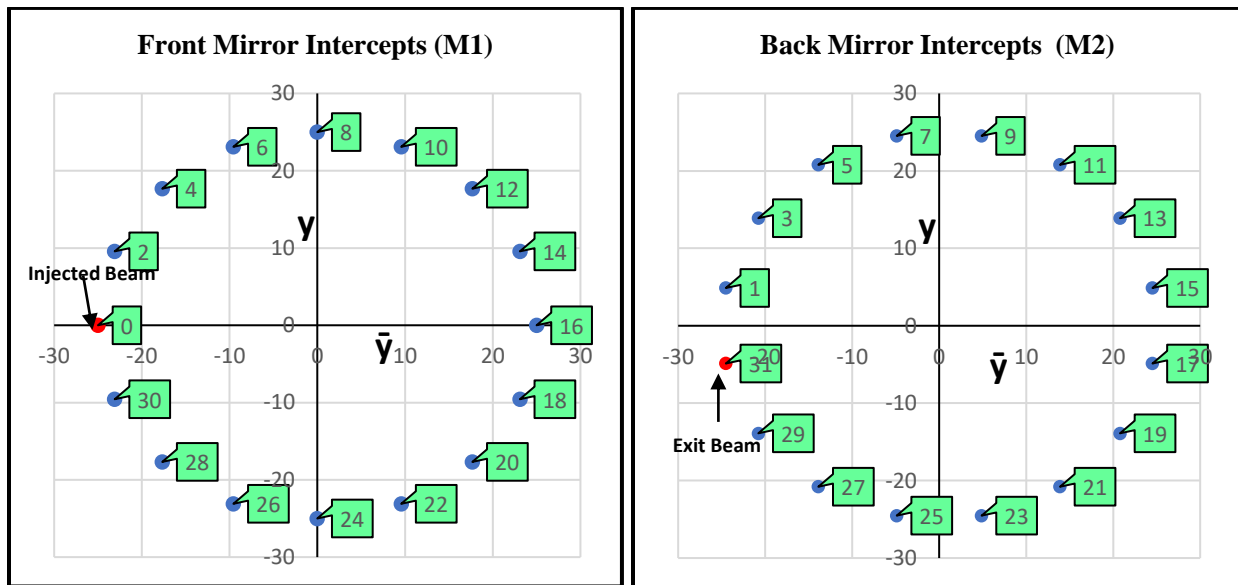


Figure 6.3 Consecutive gut ray $y\bar{y}$ diagram MPC intercepts on M1, M2.

6.5 Interlaced $y\bar{y}$ Diagram Gut Ray Design of MPC

Similarly, we follow the same producers on previous section, but we use $m=5$. The first order design of the interlaced $y\bar{y}$ diagram MPCs is shown in table 6.3, table 6.4 and the repeated $y\bar{y}$ diagram values is shown in Figure 6.4, Figure 6.5 respectively and programmed Excel file image is attached in Appendix D.

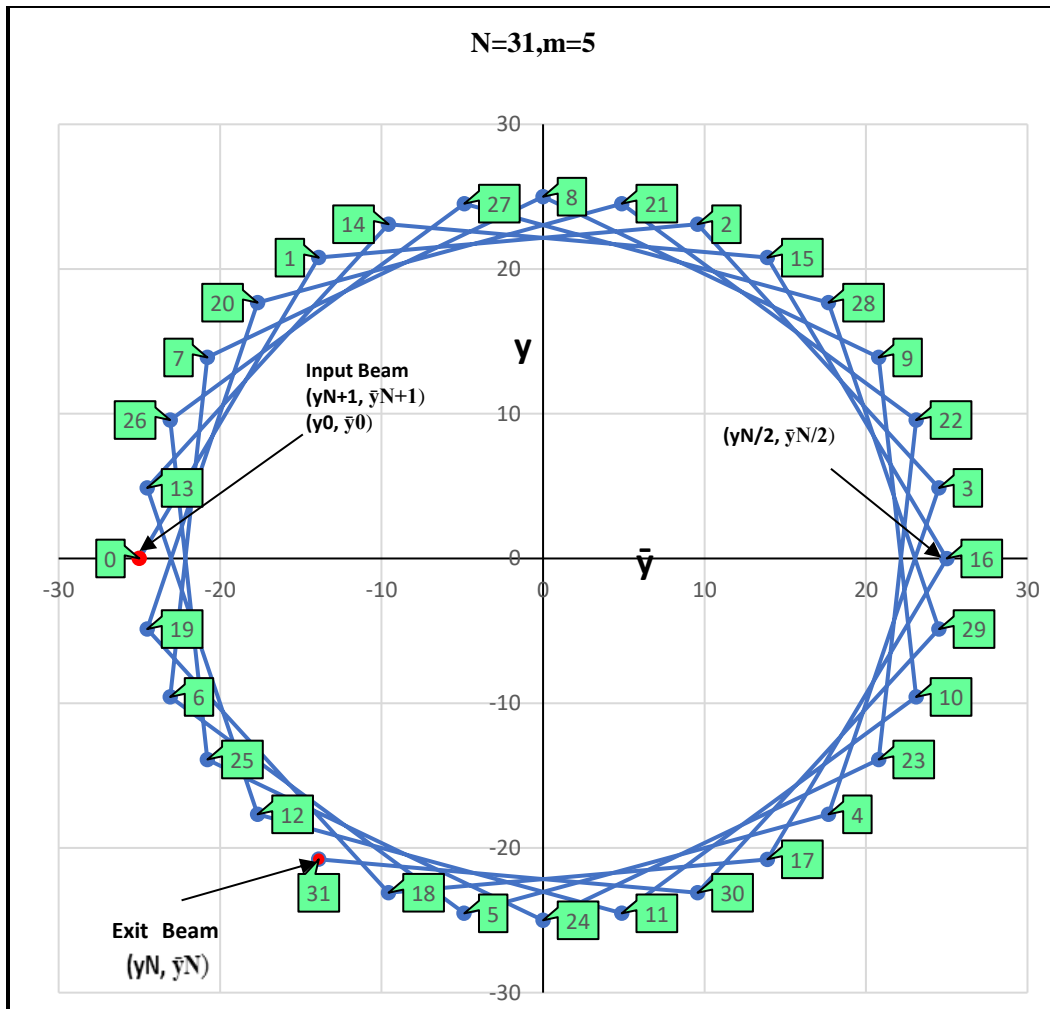


Figure 6.4 Interlaced gut ray $y\bar{y}$ diagram MPC.

Table 6.3 Description of first order Interlaced gut ray $y\bar{y}$ diagram MPC.

Properties	Allocated Values	Calculated Values	Brief Description
m	5		
r_0		-25mm	$r_0 \geq \frac{(N+1)D}{2\pi}$
Number of bounces(N)		31	N=OAL/L When N=31
Length (L)		75.552 mm	Cavity length $t1 = \frac{1}{Lg} \begin{bmatrix} y0 & \bar{y}0 \\ y1 & \bar{y}1 \end{bmatrix}$
θ_m (rad)		0.981748	$\theta_m = \frac{2\pi km}{N} = \frac{2\pi m}{N+1}$
\bar{y}_0		-25	Input beam location $\bar{y}0 = r_0 \cos(-n\theta m)$
y_0		0	Input beam location $y0 = r_0 \sin(-n\theta m)$
\bar{y}_n		$\sqrt{\quad}$	$\bar{y}n = r_0 \cos(-n\theta m)$
y_n		$\sqrt{\quad}$	$y0 = r_0 \sin(-n\theta m)$
\bar{U} (rad)		0.147061	$\bar{U} = \frac{\bar{y}i+1 - \bar{y}i}{t1}$
U		0.27513	$U = \frac{y_i+1 - y_i}{t1}$
R		169.99761	$\Phi = \frac{1}{Lg} \begin{bmatrix} u0 & \bar{u}0 \\ u1 & \bar{u}1 \end{bmatrix}$
$\frac{L}{f}$ (Stability)		0.88886	$g1=g2 = 1 - \frac{2L}{R1}$ $0 \leq \frac{L}{f} \leq 4$
FOV(Y-direction)		-15.4°	FOV=atan (U)
FOV(X-direction)		8.366°	FOV=atan (\bar{U})

Table 6.4 Interlaced gut ray $y\bar{y}$ diagram MPC design.

n	\bar{y}	y
0	-25.00	0
2	9.56709	23.09699
4	17.67767	-17.67767
6	-23.09699	-9.567086
8	0.000	25.00
10	23.09699	-9.567086
12	-17.67767	-17.67767
14	-9.56709	23.09699
16	25.00000	1.53E-14
18	-9.56709	-23.09699
20	-17.67767	17.67767
22	23.09699	9.567086
24	0.000	-25.00
26	-23.09699	9.567086
28	17.67767	17.67767
30	9.56709	-23.09699

n	\bar{y}	y
1	-13.88926	20.78674
3	24.51963	4.877258
5	-4.87726	-24.5196
7	-20.78674	13.88926
9	20.78674	13.88926
11	4.87726	-24.5196
13	-24.51963	4.877258
15	13.88926	20.78674
17	13.88926	-20.7867
19	-24.51963	-4.87726
21	4.87726	24.51963
23	20.78674	-13.8893
25	-20.78674	-13.8893
27	-4.87726	24.51963
29	24.51963	-4.87726
31	-13.88926	-20.7867

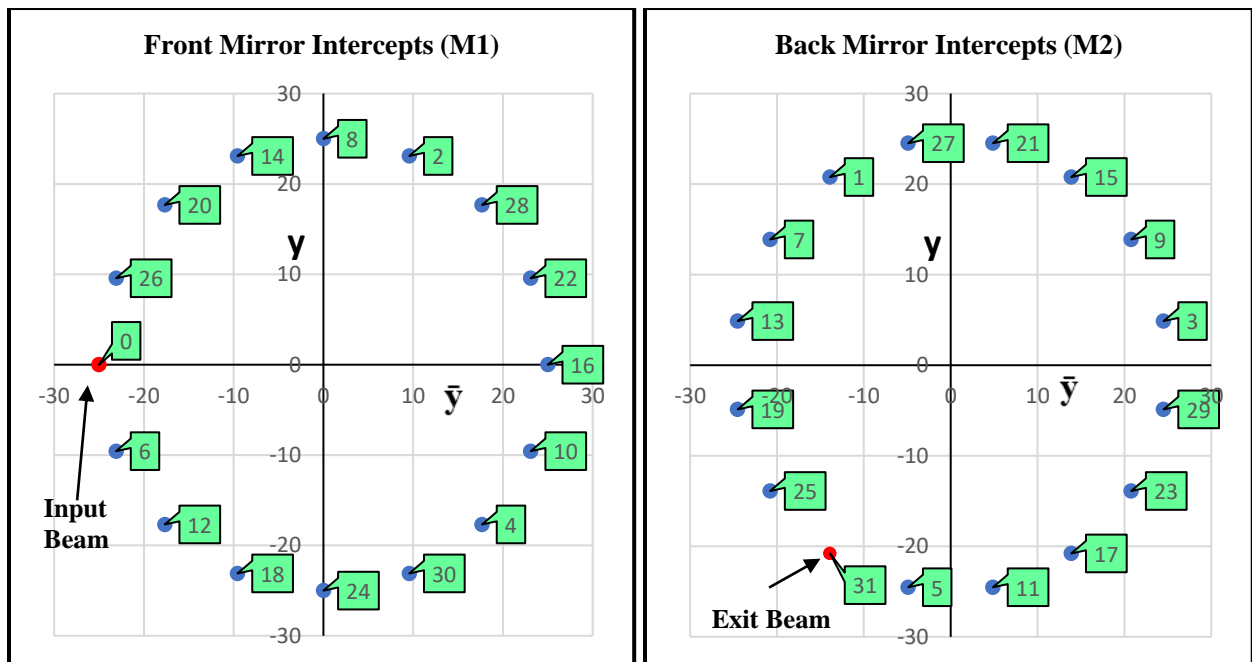


Figure 6.5 Interlaced gut ray $y\bar{y}$ diagram MPC intercepts on M1, M2.

6.6 Invalid $y\bar{y}$ Diagram Gut Ray Design of MPC

When $N+1$ and m share common factors, the results are inappropriate solutions. These flawed solutions are visually obvious and, therefore, can be quickly rejected. For example, if $N = 31$ and m is even, a common factor of $N+1$ and m is 2. If $N = 32$, then if m is a multiple of 3, the solution does not work. These flawed solutions are visually obvious – the number of points plotted is a fraction $N+1$ - and, therefore, can be quickly rejected.

The designer must avoid beams from overlapping with one another, which is important at the source and detector locations. Any beam returned to the laser source could lead to overheating and laser instability. And any other feedback into the detector will lead to an increase in the stray light and signal to noise ratio(S/N). Plus, these unwanted stray beams will have traveled different distances through the cell, contaminating the signal.

Similarly, we use the same parameters as in the previous section, but we use $m=2$ and $N=31$. The first order design of invalid $y\bar{y}$ diagram MPCs is shown in table 6.5, table 6.6, the repeated $y\bar{y}$ diagram is shown in Figure 6.6, Figure 6.7 and programmed Excel file image is attached in Appendix D. respectively.

Table 6.5 Description of first order Interlaced gut ray $y\bar{y}$ diagram MPC.

Properties	Allocated Values	Calculated Values	Brief Description
m	2		
r_0		25mm	$r_0 \geq \frac{(N+1)D}{2\pi}$
Number of bounces(N)		31	N=OAL/L when N=31
θ_m (rad)		0.392699	$\theta_m = \frac{2\pi Km}{N} = \frac{2\pi m}{N+1}$
\bar{y}_0		-25	Input beam location. $\bar{y}_0 = r_0 \cos(-n\theta_m)$
y_0		0	Input beam location. $y_0 = r_0 \sin(-n\theta_m)$
\bar{y}_n		√	$\bar{y}_n = r_0 \cos(-n\theta_m)$ From n=0 to N=31
y_n		√	$y_n = r_0 \sin(-n\theta_m)$ From n=0 to N=31
Length (L)		75.552 mm	Cavity length $t_1 = \frac{1}{Lg} \begin{bmatrix} y_0 & \bar{y}_0 \\ y_l & \bar{y}_l \end{bmatrix}$
\bar{U} (rad)		0.025188	$\bar{U} = \frac{\bar{y}_{i+1} - \bar{y}_i}{t_1}$
U(rad)		0.12663	$U = \frac{y_{i+1} - y_i}{t_1}$
R		992.5320	$\Phi = \frac{1}{Lg} \begin{bmatrix} u_0 & \bar{u}_0 \\ u_l & \bar{u}_l \end{bmatrix}$ $R = 2EFL = \frac{1}{2\Phi}$
$\frac{L}{f}$ (Stability)		0.152241	$0 \leq \frac{L}{f} \leq 4$
FOV(Y-direction)		7.22°	FOV= atan (U)
FOV(X-direction)		1.44°	FOV= atan (\bar{U})

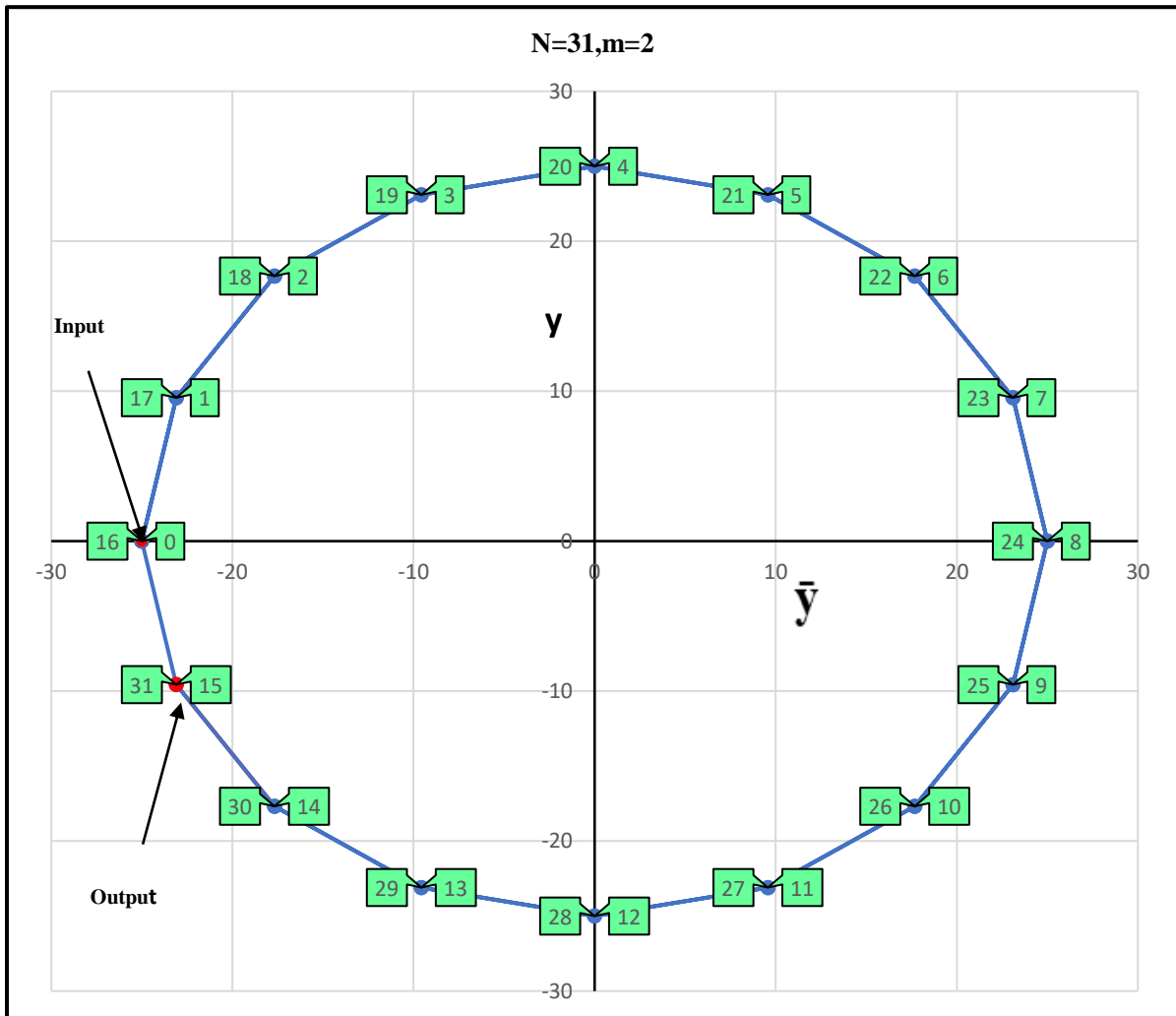


Figure 6.6 Invalid gut ray $y\bar{y}$ diagram MPC.

Table 6.6 Invalid gut ray $y\bar{y}$ diagram MPC design.

n	\bar{y}	y	n	\bar{y}	y
0	-25.00	0	1	-23.09699	9.567086
2	-17.67767	17.67767	3	-9.56709	23.09699
4	0.00000	25.00	5	9.56709	23.09699
6	17.67767	17.67767	7	23.09699	9.567086
8	25.00000	3.06E-15	9	23.09699	-9.56709
10	17.67767	-17.67767	11	9.56709	-23.097
12	0.000	-25.00	13	-9.56709	-23.097
14	-17.67767	-17.67767	15	-23.09699	-9.56709
16	-25.00000	-6.13E-15	17	-23.09699	9.567086
18	-17.67767	17.67767	19	-9.56709	23.09699
20	0.00000	25.00	21	9.56709	23.09699
22	17.67767	17.67767	23	23.09699	9.567086
24	25.00000	9.19E-15	25	23.09699	-9.56709
26	17.67767	-17.67767	27	9.56709	-23.097
28	0.00000	-25.00	29	-9.56709	-23.097
30	-17.67767	-17.67767	31	-23.09699	-9.56709

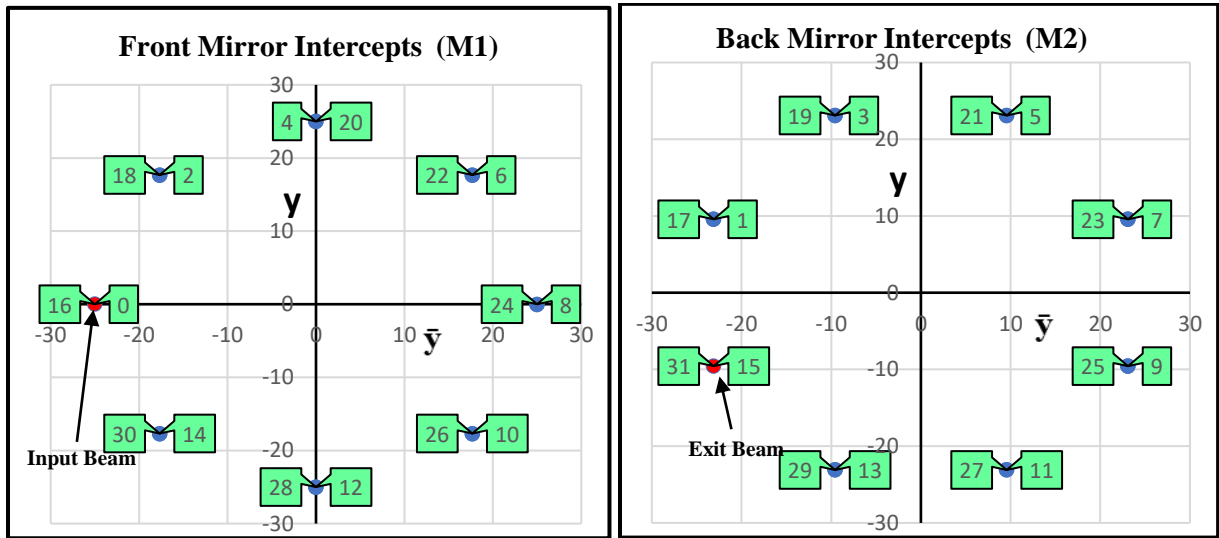


Figure 6.7 Invalid gut ray $y\bar{y}$ diagram MPC intercepts on M1, M2.

6.7 Uneven and Unstable Intercepts for \bar{y} Diagram Gut Ray Design of MPC

A major advantage of \bar{y} technique that an easy visualization of uneven, invalid, unstable and dysfunctional resonator. From Eqns. 6.4 and 6.5 these equations lead to an even distribution for the circular beam footprints, although, there are some solutions the resonator can be stabled but has uneven circular footprints distribution. For instance, if we allocate an arbitrary value for $K_m=4.5$ and from Eqn.6.5, $\Theta_m = 52.258^\circ$ and $L/f=0.776$, by way of explanation, if we assume an arbitrary number for K_m parameter or $K_m=4.5$. The resonator in this case is stable but has uneven circular distribution footprints as shown in Figure 6.8 and Figure 6.9.

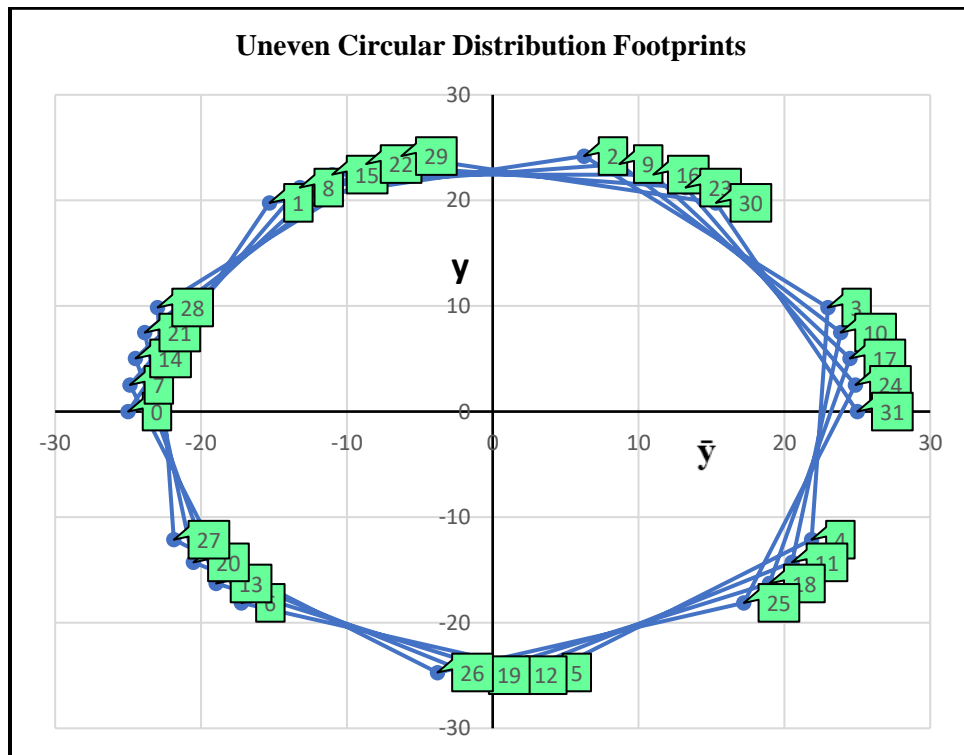


Figure 6.8 Uneven distribution gut ray \bar{y} diagram MPC.

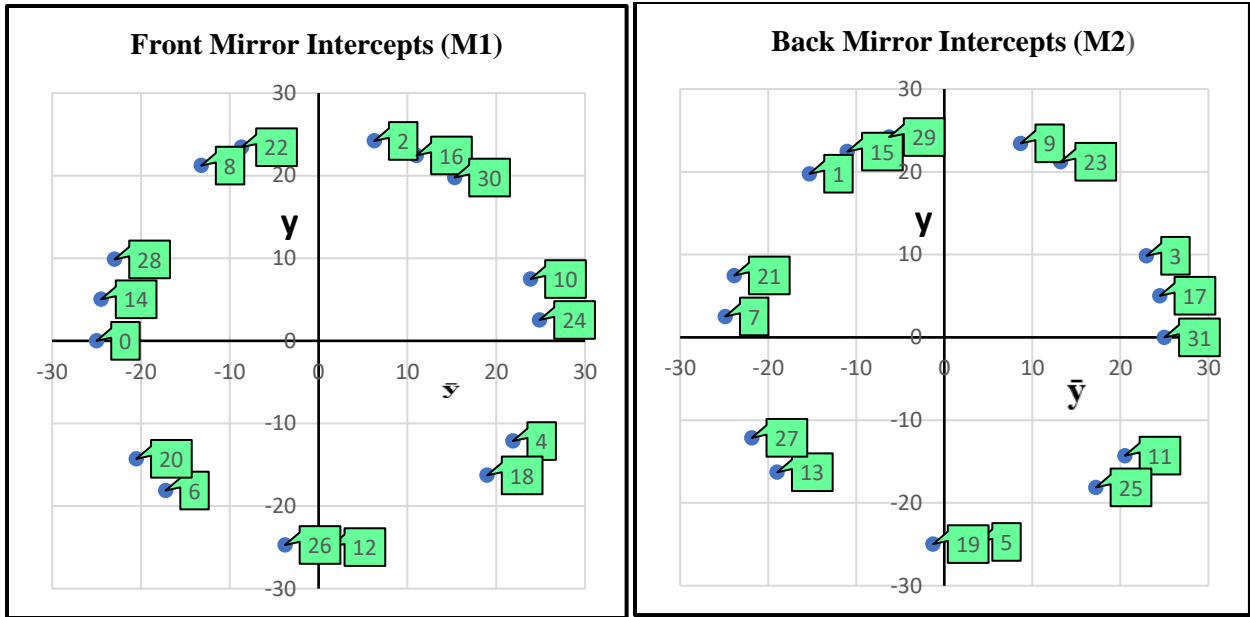


Figure 6.9 Invalid gut ray \bar{y} diagram MPC intercepts on M1, M2.

On the other hand, if we allocate an arbitrary extreme value for $K_m=15.5$, in other words, if we add an extreme constant to K_m or $K_m=15.5$. from Eqn.6.5, $\Theta_m = \pi$, and $L/f=4$. This is an unstable MPC and the solution can be quickly rejected as shown in Figure 6.10.

The unstable result from the previous example is a perfect match to our results in section 5.4 for HCMPC confocal interlaced case. For example, if $2v = 2 \times 3$ and μ is 3, a [Use your notation here!] common factor of $2v$ and μ is odd numbers or 3 and $\Theta = \pi$, therefore, our \bar{y} diagram results will always be identical to HCMPC approach but our approach is rapid and intuitive for optical designers and the K_m and Θ_m equations can be manipulated for a variety of applications.

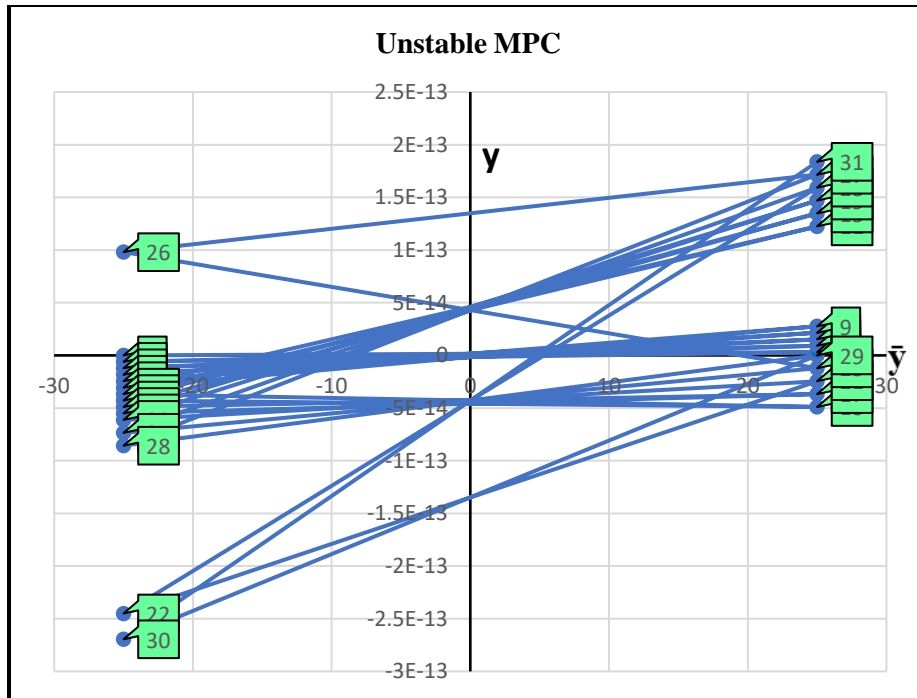


Figure 6.10 Unstable gut ray $y\bar{y}$ diagram MPC.

6.8 Collimated Injected Beam $y\bar{y}$ Diagram Design of MPC

In the previous Chapter, we found out that the ray tracing software (ZEMAX) doesn't provide accurate data of gut ray L_g and EPD and we rotated the design by the angle of the slope to obtain accurate data. The reasons of these discrepancies are the entrance pupil diameter represented by ray tracing software is the diameter of injected beam and the injected beam generally far smaller from the $y\bar{y}$ diagram entrance pupil diameter. Where the $y\bar{y}$ diagram entrance pupil diameter is nearly the diameter of the circle of dots.

Although it's not necessary to rotate the design and the designer can always use the gut ray design, more importantly, this simplifies communicating the design to the mechanical design team when specifying the drawings for the mirrors and the designer can use the ray tracing software for precision tolerances analysis and aberration result. It means the injected beam only has an y-angle

instead of x- field angle and y- field angle and the entry of the design into an optical design code is easier, to get the injected beam to be collimated space, the first segment must be parallel to the \bar{y} axis as discussed in previous Chapter. We create collimated input equations of MPC $y\bar{y}$ diagram, a constant of $\pi/2 + \Theta m/2$ is added to equation 6.2 and 6.3, placing the injected beam segment at the top of the diagram and symmetric about the y-axis. The equations for the \bar{y}_n values are, therefore,

$$\bar{y}_n = -r_0 \cos\left(-\Theta m * n + \frac{\pi}{2} + \frac{\Theta m}{2}\right) \quad (6.6)$$

$$= -r_0 \cos\left(\left(-\Theta m * n + \frac{\Theta m}{2}\right) + \frac{\pi}{2}\right), \quad (6.7)$$

where,

$$\cos\left(\beta + \frac{\pi}{2}\right) = \sin(-\beta) \quad (6.8)$$

$$= -r_0 \sin\left(-\left(-\Theta m * n + \frac{\Theta m}{2}\right)\right) \quad (6.9)$$

$$= -r_0 \sin\left(\left(\Theta m * n - \frac{\Theta m}{2}\right)\right) \quad (6.10)$$

$$\bar{y}_n = -r_0 \sin\left(\Theta m * \left(n - \frac{1}{2}\right)\right), \quad (6.11)$$

where $n = 0$ to N ,

Similarly, the equations for the y_n values are, therefore,

$$y_n = -r_0 \sin\left(-\Theta m * n + \frac{\pi}{2} + \frac{\Theta m}{2}\right) \quad (6.12)$$

$$= -r_0 \sin\left(\left(-\Theta m * n + \frac{\Theta m}{2}\right) + \frac{\pi}{2}\right) \quad (6.13)$$

$$= -r_0 \sin\left(\left(-\Theta m \left(n - \frac{1}{2}\right)\right) + \frac{\pi}{2}\right), \quad (6.14)$$

where,

$$\sin\left(-\beta + \frac{\pi}{2}\right) = \cos(-\beta) = \cos(\beta) \quad (6.15)$$

$$y_n = -r_0 \cos\left(\Theta m * \left(n - \frac{1}{2}\right)\right), \quad (6.16)$$

where $n = 0$ to N .

Since we require the mirrors to be separated by L and scaled by Lg , we can use the simple relations for computing distance on the $y\bar{y}$ diagram to derive the Lg :

$$\begin{aligned}
 Lg &= (y_0\bar{y}_1 - \bar{y}_0y_1) * \left(\frac{1}{L}\right) \\
 &= \left(r_0 \cos\left(-\frac{\theta_m}{2}\right) * r_0 \sin\left(\frac{\theta_m}{2}\right)\right) - \left(r_0 \sin\left(-\frac{\theta_m}{2}\right) r_0 \cos\left(\frac{\theta_m}{2}\right)\right) * \left(\frac{1}{L}\right) \\
 &= r_0^2 \left(\cos\left(-\frac{\theta_m}{2}\right) * \sin\left(\frac{\theta_m}{2}\right)\right) - \left(\sin\left(-\frac{\theta_m}{2}\right) \cos\left(\frac{\theta_m}{2}\right)\right) * \left(\frac{1}{L}\right) \tag{6.17}
 \end{aligned}$$

$$Lg = \left(2 r_0^2 \sin\left(\frac{\theta_m}{2}\right) \cos\left(\frac{\theta_m}{2}\right)\right) * \left(\frac{1}{L}\right)$$

$$Lg = \left(r_0^2 \sin(\theta_m)\right) * \left(\frac{1}{L}\right). \tag{6.18}$$

Using any programming software, the designer can now rapidly scan through multiple designs for a single set of specifications and, when further analysis with an optical design code is desired, the mirrors ROC, separation, location of injected beam offset on initial mirror, $(x_0, y_0) = (\bar{y}_0, y_0)$ and the injected beam field angle, y -angle = $\text{atan}(\bar{u}_0)$ where \bar{u} is readily computed through Delano the $y\bar{y}$ diagram equations in Chapter 2.

We follow the same procedures for gut ray $y\bar{y}$ diagram HCMPCs to specify the MPC parameters of collimated input beam. Firstly, from section 6.2 we can proceed to collimated input beam of the consecutive or interlaced MPC $y\bar{y}$ diagram, thus, the beam will be injected through the back of M1 at calculated $r_0=25$ mm and calculated $N=31$ and cavity length $L=75.55$ mm. Secondly, from equation 6.4 and 6.5 the angle θ_m between bounces for consecutive or interlaced designs can be calculated, $m=1,2,3$ and 5 .

Thirdly, from equations 6.11, 6.16 and 6.18 the points on the $y\bar{y}$ diagram will fall on a circle of radius r_0 but the first two points will be collimated to optical axis.

Fourthly, the radius of curvature, G parameters, stability and EFL, can be calculated from the $y\bar{y}$ diagram characterization. Lastly, we plotted the repeated the skew ray $y\bar{y}$ values and as viewed along the Z axis from behind M1. We present 4 different designs example and compared with Zemax data for proof of concept.

6.8.1 Collimated Input Beam Consecutive $y\bar{y}$ Diagram Design of MPC

In this design we use consecutive ($m=1$), $r_0=25\text{mm}$, $N=31$ and collimated input beam. In collimated approach equations 6.11, 6.16 and 6.18 will take care of geometrical optics convention signs, with positive L_g .

We notice that the intercepts $(0,1)$, $(16,17)$ are both collimated and are, in fact, images of each other: they, (\bar{y}_{32}, y_{32}) and (\bar{y}_{17}, y_{17}) , are inverted images of each other. In fact, every 16th reflection of any mirror intercept is an inverted image. And the beam size does not significantly grow as the beams bounce back and forth between the mirrors but is continuously refocused by the concave MPC mirrors.

The first order design of collimated $y\bar{y}$ diagram MPCs is shown in Table 6.7, Table 6.8, the repeated $y\bar{y}$ diagram is shown in Figure 6.11, Figure 6.12, the ZEMAX design data are shown in Figure 6.13, Figure 6.14 and programmed Excel file image is attached on Appendix D. respectively.

Table 8.7 Description of first order consecutive collimated ray $y\bar{y}$ diagram MPC.

Properties	Allocated Values	Calculated Values	Brief Description
m	1		
r_0		25mm	$r_0 \geq \frac{(N+1)D}{2\pi}$
Number of bounces(N)		31	$N=OAL/L$
Length (L)		75.552 mm	Cavity length $t1 = \frac{1}{Lg} \begin{bmatrix} y0 & \bar{y}0 \\ y1 & \bar{y}1 \end{bmatrix}$
$\Theta_m(\text{rad})$		0.19634954	$\Theta_m = \frac{2\pi m}{N+1}$
\bar{y}_0		-2.45043	$\bar{y}_n = r_0 \sin\left(\Theta_m * \left(n - \frac{1}{2}\right)\right)$
y_0		24.87962	$y_n = r_0 \cos\left(\Theta_m * \left(n - \frac{1}{2}\right)\right)$
EPD		50 mm	$EPD=2 * y_1$
Lg		1.63874	$Lg = \left(2 r_0^2 \sin\left(\frac{\Theta_m}{2}\right) \cos\left(\frac{\Theta_m}{2}\right)\right) * \left(\frac{1}{L}\right)$
$\bar{U}(\text{rad})$		0.064867	$\bar{U} = \frac{\bar{y}i + 1 - \bar{y}i}{t1}$
U(rad)		0	$U = \frac{yi + 1 - yi}{t1}$
R		3931.98556	$R=2EFL=\frac{1}{2\Phi}$
$\frac{L}{f}$ (Stability)		0.038429	$0 \leq \frac{L}{f} \leq 4$
FOV(X-direction)		3.711425°	$FOV=\text{atan}(\bar{U})$

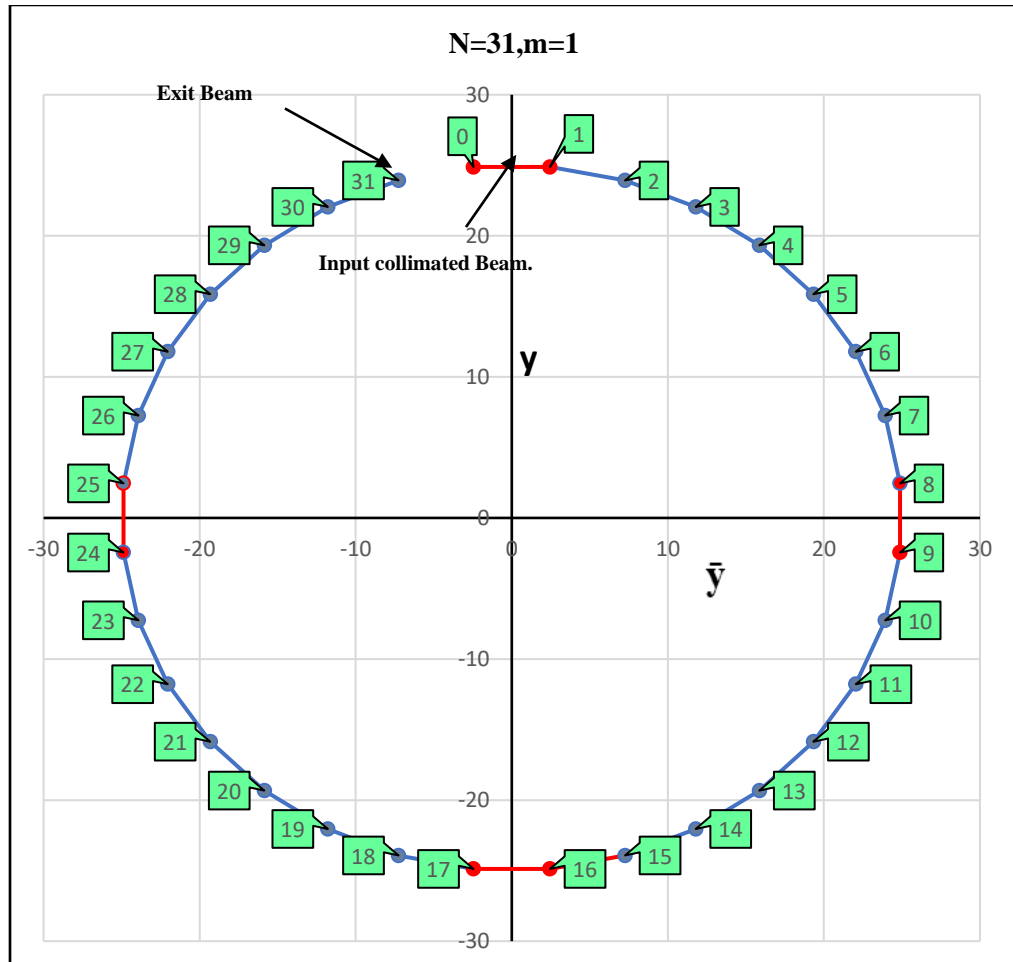


Figure 6.11 Consecutive collimated input \bar{y} diagram MPC.

Table 6.8 Consecutive collimated Input $y\bar{y}$ Diagram MPC intercepts M1, M2 data.

N	\bar{y}	y
0	-2.45043	24.87962
2	7.25712	23.92351
4	15.85983	19.32526
6	22.04803	11.78492
8	24.87962	2.45043
10	23.92351	-7.25712
12	19.32526	-15.85983
14	11.78492	-22.04803
16	2.45043	-24.87962
18	-7.25712	-23.92351
20	-15.85983	-19.32526
22	-22.04803	-11.78492
24	-24.87962	-2.45043
26	-23.92351	7.25712
28	-19.32526	15.85983
30	-11.78492	22.04803

N	\bar{y}	y
1	2.45043	24.87962
3	11.78492	22.04803
5	19.32526	15.85983
7	23.92351	23.92351
9	24.87962	24.87962
11	22.04803	22.04803
13	15.85983	15.85983
15	7.25712	7.25712
17	-2.45043	-2.45043
19	-11.78492	-11.78492
21	-19.32526	-19.32526
23	-23.92351	-23.92351
25	-24.87962	-24.87962
27	-22.04803	-22.04803
29	-15.85983	-15.85983
31	-7.25712	-7.25712

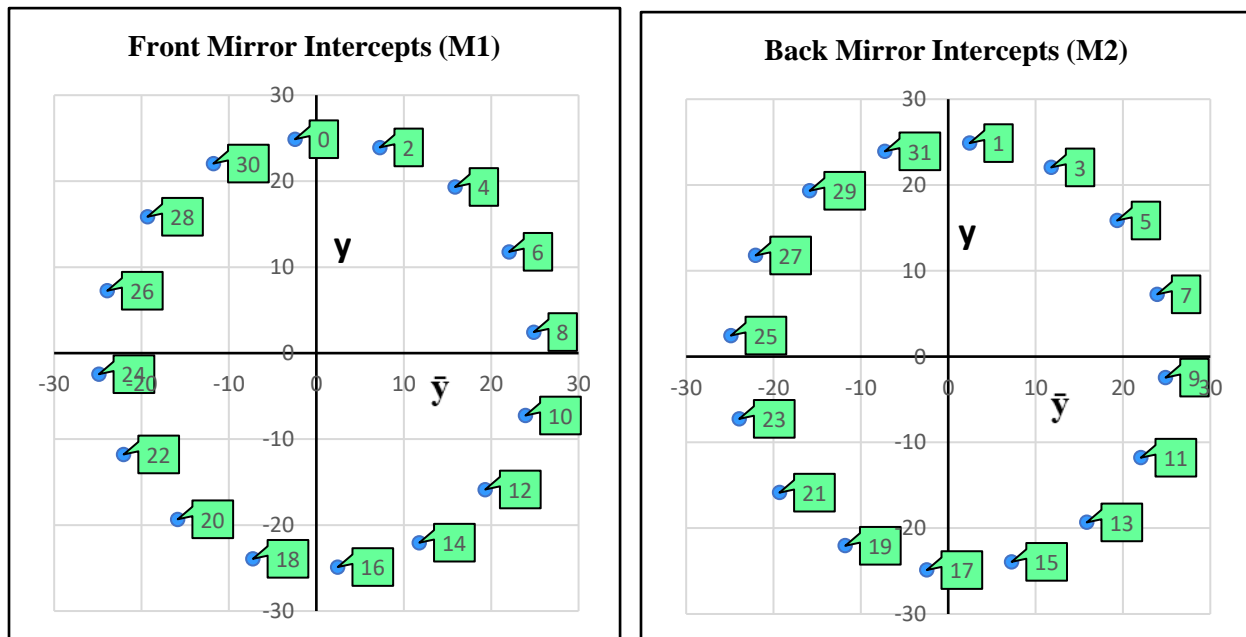


Figure 6.12 Consecutive collimated Input $y\bar{y}$ Diagram MPC intercepts M1, M2 plot.

Consecutive collimated m=1

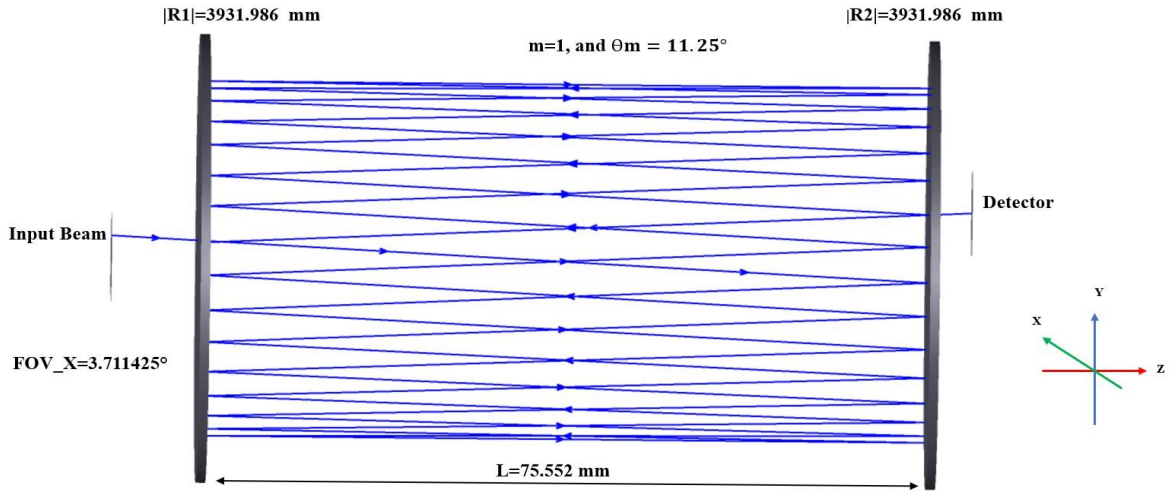


Figure 6.13 Consecutive collimated input ray tracing simulation [7].

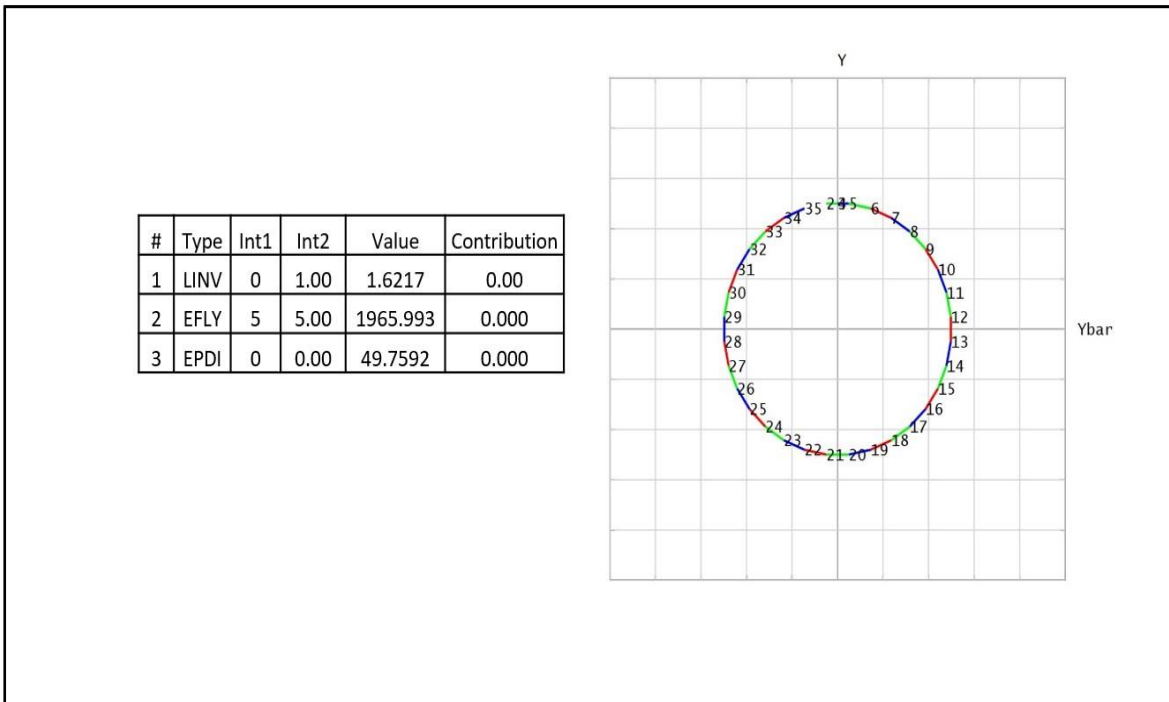


Figure 6.14 An image of consecutive collimated input ray tracing simulation data [7].

6.8.2 Collimated Input Beam Interlaced $y\bar{y}$ Diagram Design of MPC

Similarly, in this design we use interlaced design where ($m=3$), $r_0=25\text{mm}$, $N=31$ and collimated input beam. In collimated approach equations 6.11, 6.16 and 6.18 will take care of geometrical optics convention signs. The first order design of collimated $y\bar{y}$ diagram MPCs is shown in Table 6.9, Table 6.10, the repeated $y\bar{y}$ diagram values is shown in Figure 6.15, Figure 6.16, the ZEMAX design data are shown in Figure 6.17, Figure 6.18 respectively.

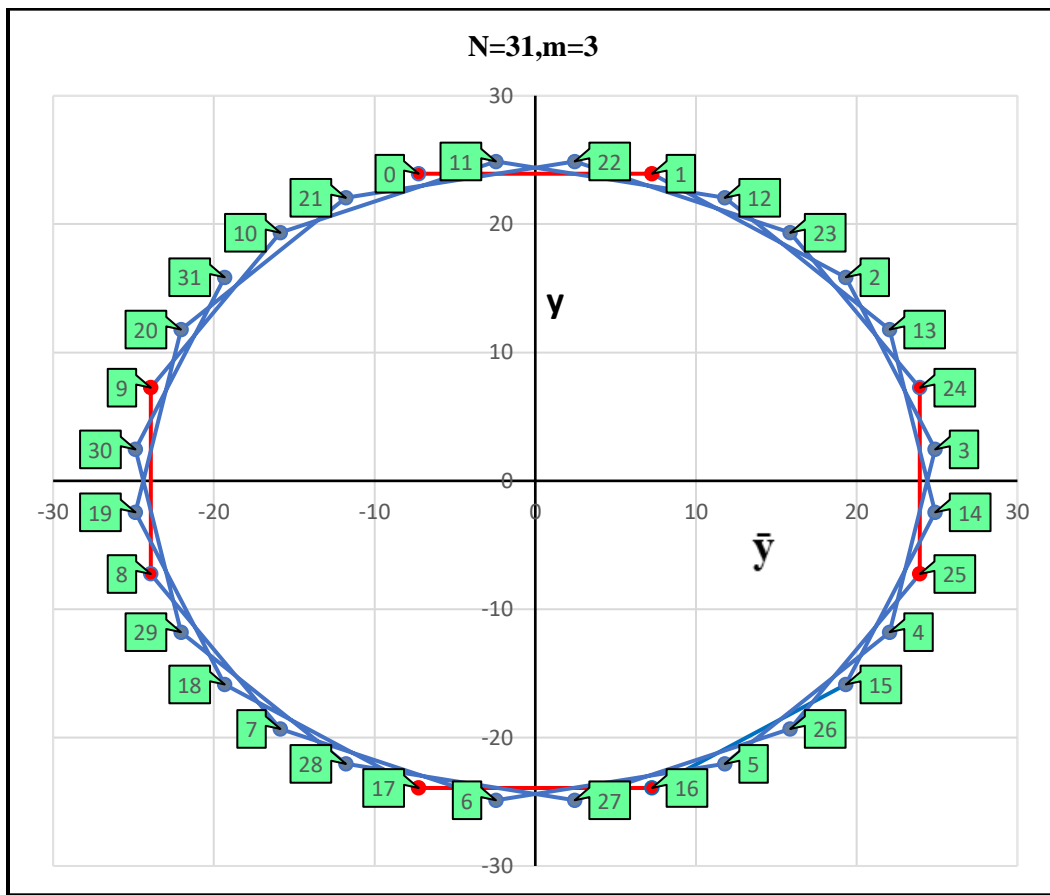


Figure 6.15 Interlace collimated input $y\bar{y}$ diagram MPC.

Table 6.9 Description of first order interlaced collimated ray $y\bar{y}$ diagram MPC.

Properties	Allocated Values	Calculated Values	Brief Description
m	3		
r_0		25mm	$r_0 \geq \frac{(N+1)D}{2\pi}$
Number of bounces(N)		31	$N=OAL/L$
Length (L)		75.552 mm	Cavity length $t1 = \frac{1}{Lg} \begin{bmatrix} y0 & \bar{y}0 \\ y1 & \bar{y}1 \end{bmatrix}$
$\Theta_m(\text{rad})$		0.58904862	$\Theta_m = \frac{2\pi m}{N+1}$
\bar{y}_0		-7.25712	$\bar{y}_n = r_0 \sin\left(\Theta_m * \left(n - \frac{1}{2}\right)\right)$
y_0		23.92351	$y_n = r_0 \cos\left(\Theta_m * \left(n - \frac{1}{2}\right)\right)$
EPD		50 mm	$EPD=2 * y_1$
Lg		4.5959	$Lg = \left(2 r_0^2 \sin\left(\frac{\Theta_m}{2}\right) \cos\left(\frac{\Theta_m}{2}\right)\right) * \left(\frac{1}{L}\right)$
$\bar{U}(\text{rad})$		0.192109	$\bar{U} = \frac{\bar{y}i + 1 - \bar{y}i}{t1}$
$U(\text{rad})$		0	$U = \frac{yi + 1 - yi}{t1}$
R		448.299	$\Phi = \frac{1}{Lg} \begin{bmatrix} u0 & \bar{u}0 \\ u1 & \bar{u}1 \end{bmatrix}$ $R=2EFL=\frac{1}{2\Phi}$
$\frac{L}{f}$ (Stability)		0.337061	$g_1=g_2=1 - \frac{2L}{R1}$ $0 \leq \frac{L}{f} \leq 4$
FOV(X-direction)		10.87456°	$FOV=\text{atan}(\bar{U})$

Table 6.10 Interlace collimated input $y\bar{y}$ diagram MPC design.

N	\bar{y}	y
0	-7.25712	23.92351
2	19.32526	15.85983
4	22.04803	-11.78492
6	-2.45043	-24.87962
8	-23.92351	-7.25712
10	-15.85983	19.32526
12	11.78492	22.04803
14	24.87962	-2.45043
16	7.25712	-23.92351
18	-19.32526	-15.85983
20	-22.04803	11.78492
22	2.45043	24.87962
24	23.92351	7.25712
26	15.85983	-19.32526
28	-11.78492	-22.04803
30	-24.87962	2.45043

N	\bar{y}	y
1	7.25712	23.92351
3	24.87962	2.45043
5	11.78492	-22.04803
7	-15.85983	-19.32526
9	-23.92351	7.25712
11	-2.45043	24.87962
13	22.04803	11.78492
15	19.32526	-15.85983
17	-7.25712	-23.92351
19	-24.87962	-2.45043
21	-11.78492	22.04803
23	15.85983	19.32526
25	23.92351	-7.25712
27	2.45043	-24.87962
29	-22.04803	-11.78492
31	-19.32526	15.85983

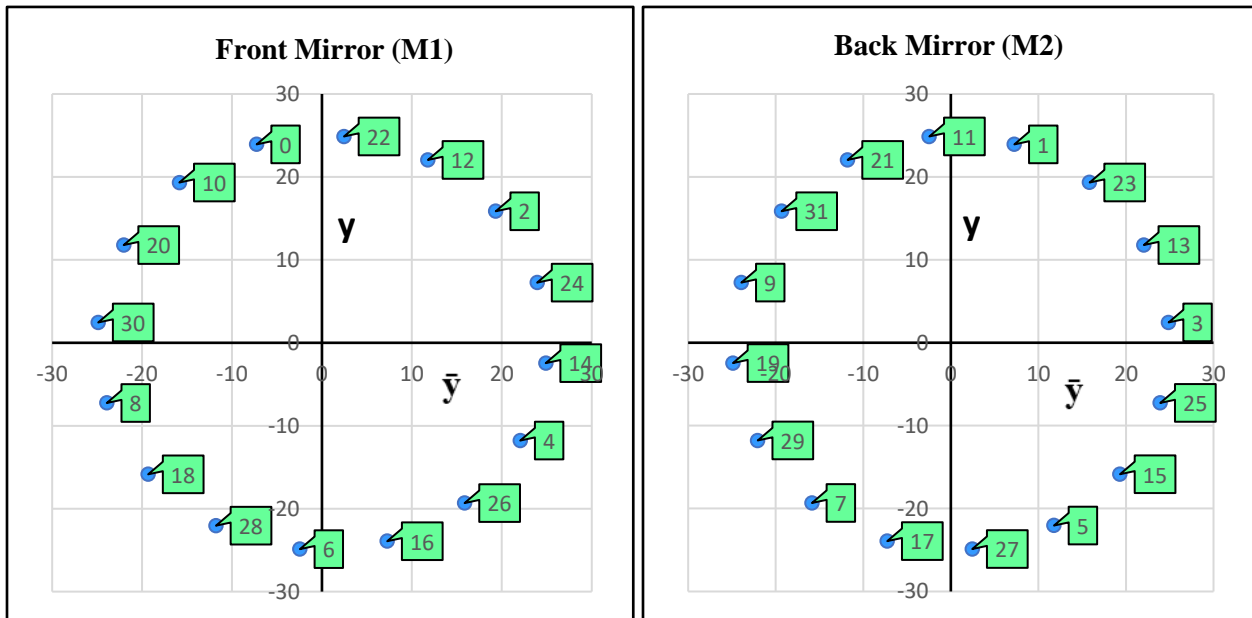


Figure 6.16 Interlace Collimated input $y\bar{y}$ diagram MPC intercepts M1, M2.

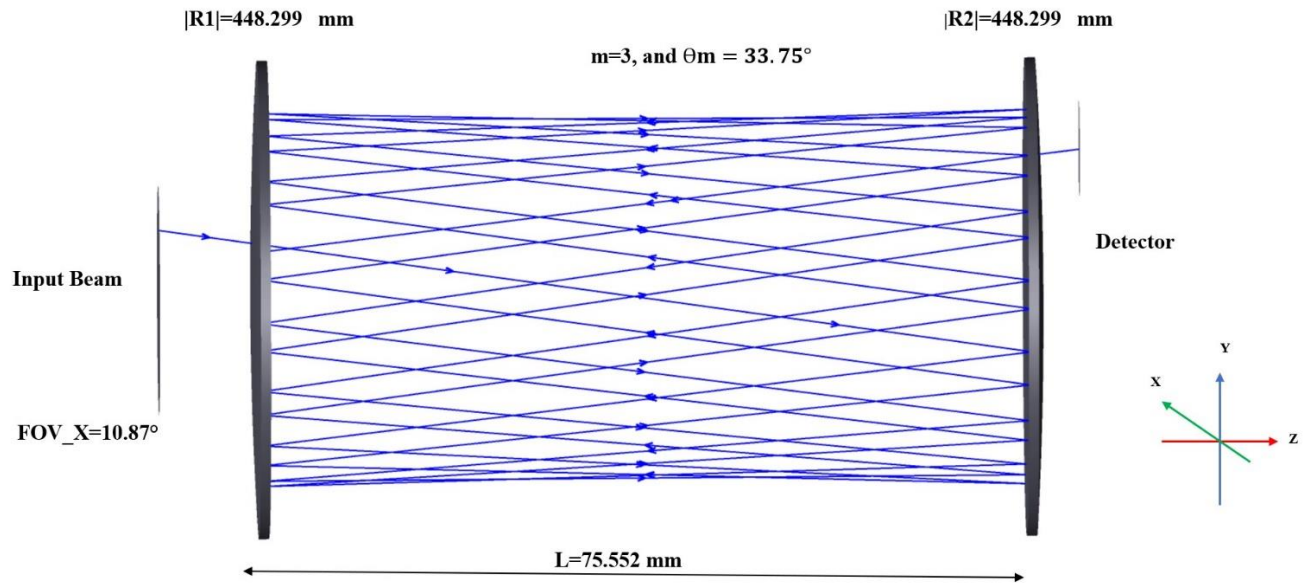


Figure 6.17 Interlace Collimated input ray tracing simulation [7].

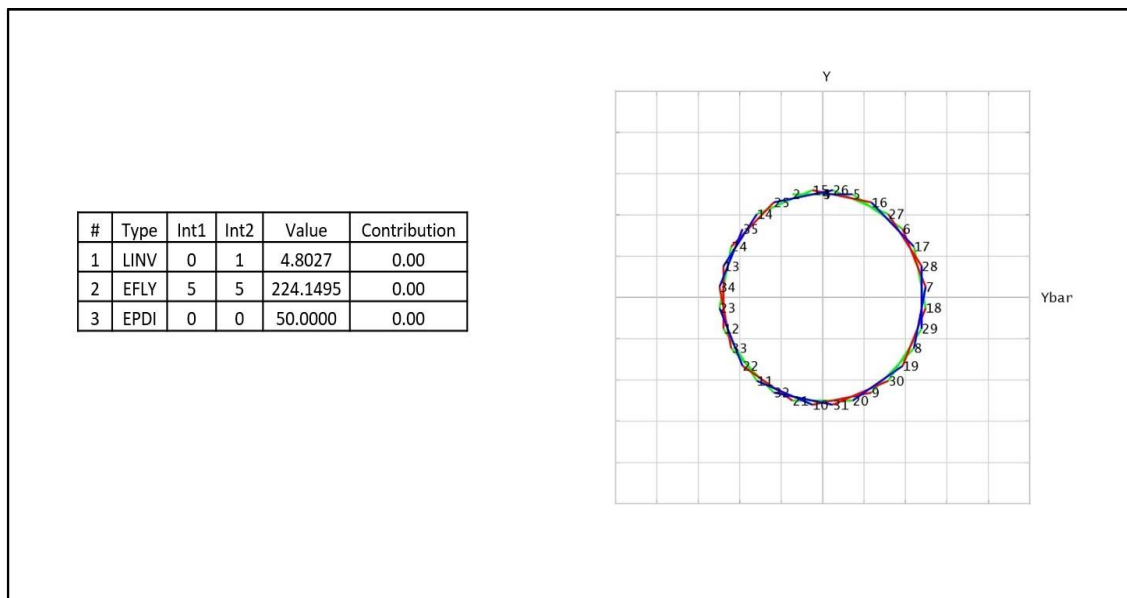


Figure 6.18 An image of interlaced collimated input ray tracing simulation data [7].

6.8.3 Collimated Input Beam Invalid \bar{y} Diagram Design of MPC

Similarly, when $m=2$ this is invalid solution. Because of when $N = 31$ and m is even, a common factor of $N+1$ and m is 2. The first order design of collimated invalid \bar{y} diagram MPCs is shown in table 6.11, table 6.12, the repeated \bar{y} diagram values are shown in Fig 6.19, Figure 6.20, the ZEMAX design data are shown in Figure 6.21, Figure 6.22 and programmed Excel file is attached in Appendix D., respectively.

Table 6.11 Description of first order invalid collimated ray \bar{y} diagram MPC.

Properties	Allocated Values	Calculated Values	Brief Description
m	2		
r_0		25mm	$r_0 \geq \frac{(N+1)D}{2\pi}$
Number of bounces(N)		31	$N=OAL/L$
Length (L)		75.552 mm	Cavity length $t1 = \frac{1}{Lg} \begin{bmatrix} y0 & \bar{y}0 \\ y1 & \bar{y}1 \end{bmatrix}$
$\theta_m(\text{rad})$		0.39269	$\theta_m = \frac{2\pi m}{N+1}$
\bar{y}_0		-4.87726	$\bar{y}_n = r_0 \sin\left(\theta_m * \left(n - \frac{1}{2}\right)\right)$
y_0		24.51963	$y_n = r_0 \cos\left(\theta_m * \left(n - \frac{1}{2}\right)\right)$
EPD		50 mm	$EPD=2 * y_1$
Lg		3.16572	Lg $= \left(2 r_0^2 \sin\left(\frac{\theta_m}{2}\right) \cos\left(\frac{\theta_m}{2}\right)\right)$ $* \left(\frac{1}{L}\right)$
$\bar{U}(\text{rad})$		0.129110	$\bar{U} = \frac{\bar{y}^{i+1} - \bar{y}^i}{t1}$

U(rad)		0	$U = \frac{y_{i+1} - y_i}{t_1}$
R		992.532	$\Phi = \frac{1}{L_g} \begin{bmatrix} u_0 & \bar{u}_0 \\ u_1 & \bar{u}_1 \end{bmatrix}$ $R = 2EFL = \frac{1}{2\Phi}$
$\frac{L}{f}$ (Stability)		0.152241	$g_1 = g_2 = 1 - \frac{2L}{R_1}$ $0 \leq \frac{L}{f} \leq 4$
FOV(X-direction)		7.356759°	FOV=atan(\bar{U})

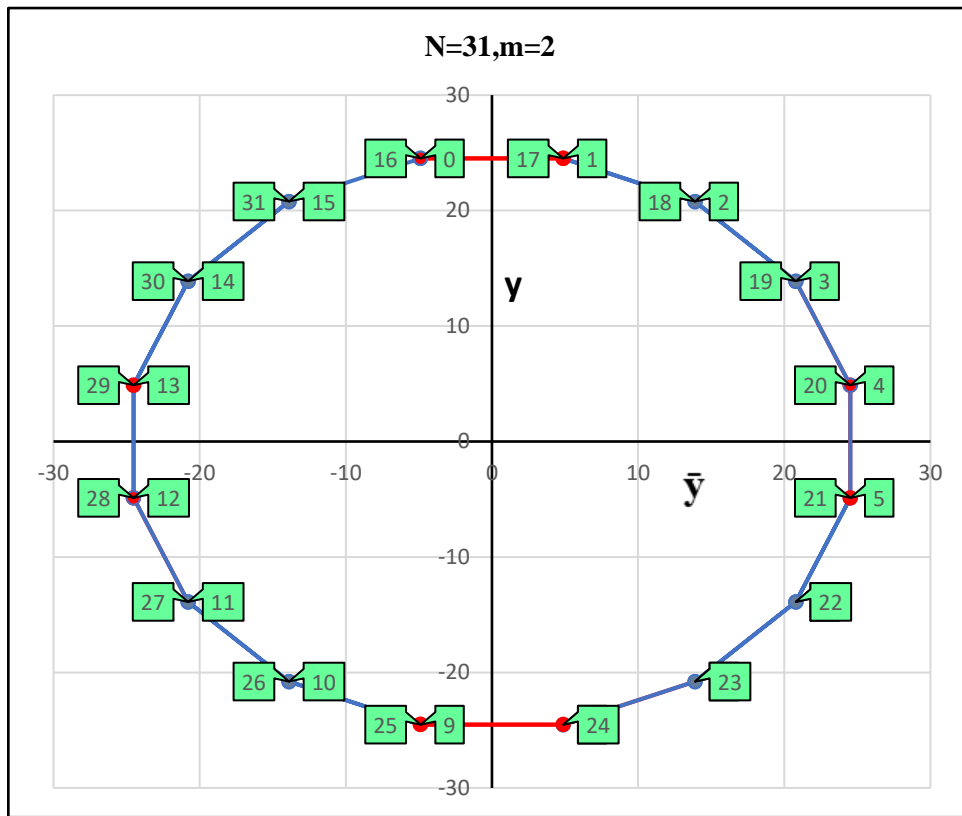


Figure 6.19 Invalid collimated input $y\bar{y}$ diagram MPC.

Table 6.12 Invalid collimated interlaced $y\bar{y}$ diagram MPC design.

N	\bar{y}	y
0	-4.87726	24.51963
2	13.88926	20.78674
4	24.51963	4.87726
6	20.78674	-13.88926
8	4.87726	-24.51963
10	-13.88926	-20.78674
12	-24.51963	-4.87726
14	-20.78674	13.88926
16	-4.87726	24.51963
18	13.88926	20.78674
20	24.51963	4.87726
22	20.78674	-13.88926
24	4.87726	-24.51963
26	-13.88926	-20.78674
28	-24.51963	-4.87726
30	-20.78674	13.88926

N	\bar{y}	y
1	4.87726	24.51963
3	20.78674	13.88926
5	24.51963	-4.87726
7	13.88926	-20.78674
9	-4.87726	-24.51963
11	-20.78674	-13.88926
13	-24.51963	4.87726
15	-13.88926	20.78674
17	4.87726	24.51963
19	20.78674	13.88926
21	24.51963	-4.87726
23	13.88926	-20.78674
25	-4.87726	-24.51963
27	-20.78674	-13.88926
29	-24.51963	4.87726
31	-13.88926	20.78674

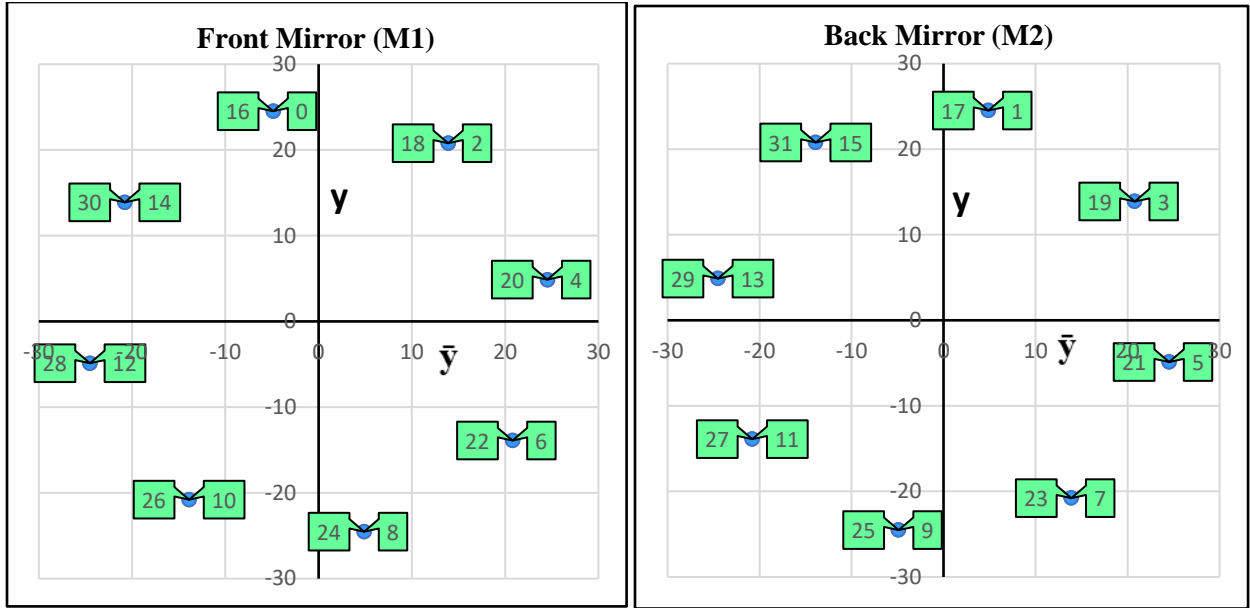


Figure 6.20 Invalid collimated input $y\bar{y}$ diagram MPC intercepts M1, M2.

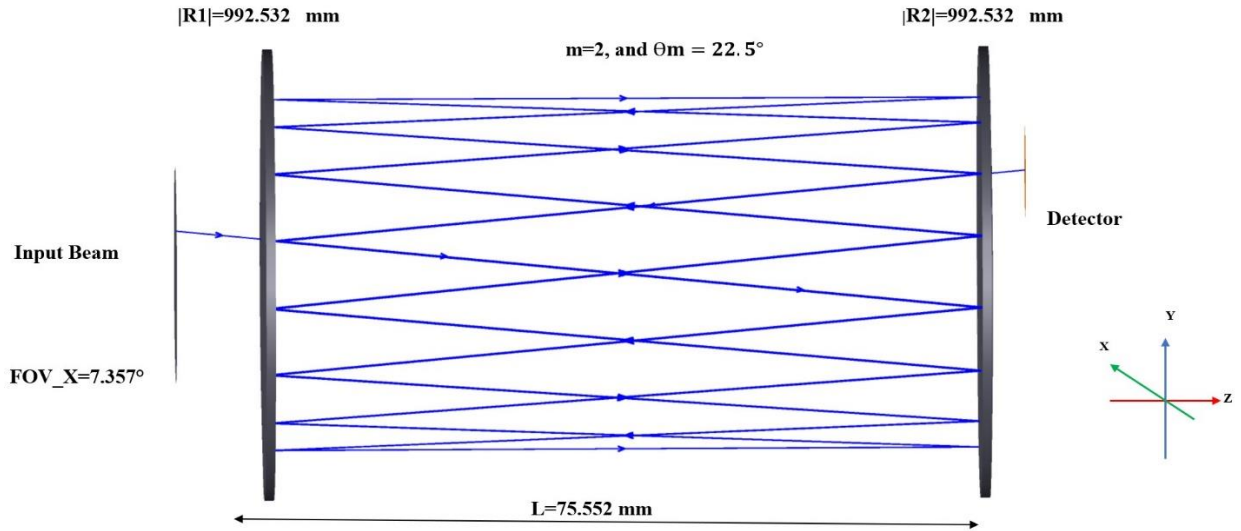


Figure 6.21 Invalid Collimated input ray tracing simulation [7].

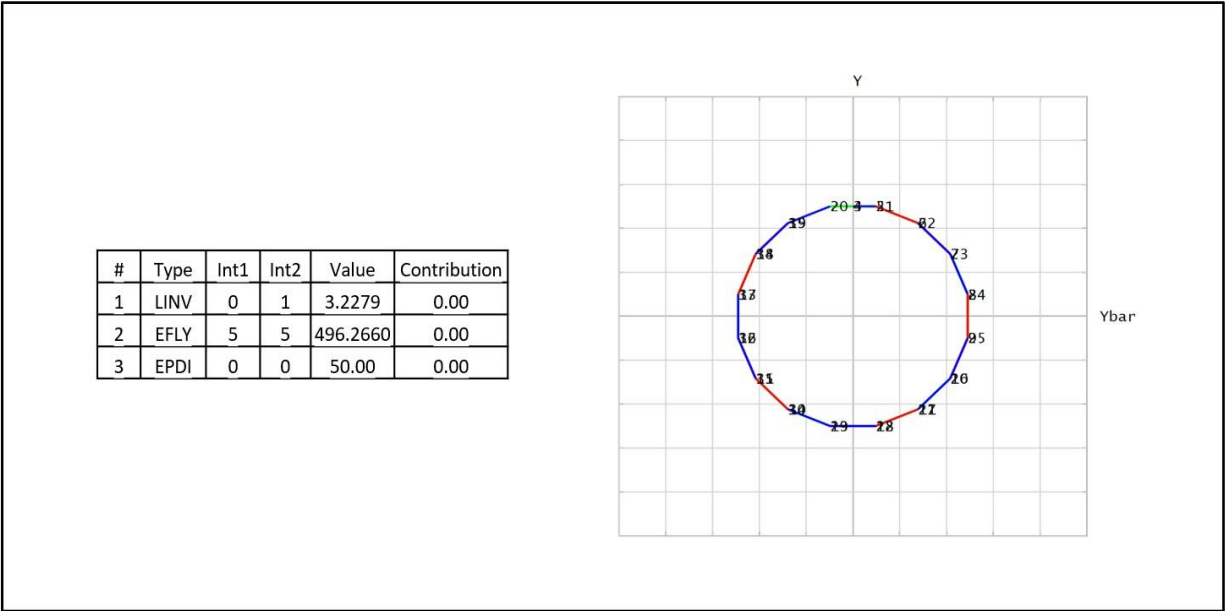


Figure 6.22 An image of invalid collimated input ray tracing simulation data [7].

We compare the resulting designs data tabulated in Table 6.7.3.3. First, we note that the mirror radius decreases with increasing m , where $|R|$ is inversely dependent on m . Next, we see that, for $m = 2$, the design produces 16 bounces beams that hit the exit position twice, so the solution is not functional: N is odd and m is even. Finally, the injection and detection points are always m footprints apart.

Table 6.13 Four different solutions of collimated MPCs using the $y\bar{y}$ diagram.

m	Θ_m	ROC	Source x-angle(deg)
1	11.25°	3931.986	3.71
2	22.5°	992.532	7.357
3	33.75°	448.299	10.87
5	56.25°	169.98	17.33

6.9 Designing a MPC with Two Different Mirror Radii of Curvatures

The advantage of the $y\bar{y}$ diagram method is the graphical interpretations one can employ to set up new design approaches. For example, one can quickly modify the design by changing the value of r_0 for every other mirror intercept. This also requires a change in the calculation for the Lg since the initial two data points are no longer in collimated space, so we modified in Eqns.6.17 and 6.18 to:

$$\begin{aligned} Lg &= \left(2 r_{01} r_{02} \sin\left(\frac{\theta_m}{2}\right) \cos\left(\frac{\theta_m}{2}\right) \right) * \left(\frac{1}{L}\right) \\ Lg &= \left(r_{01} r_{02} \sin(\theta_m) \right) * \left(\frac{1}{L}\right) \end{aligned} \quad (6.19)$$

For this design, we did not force the injected beam to be in collimated space in the $y\bar{y}$ diagram, so one must input both an x- and y-field angle when entering it into a lens design program where

$$\text{y-angle} = \text{atan}(u_0) \quad (6.20)$$

$$\text{x-angle} = \text{atan}(\bar{u}_0). \quad (6.21)$$

We will present three different cases design for MPC with two different radii of curvatures:

Concave, concave mirrors, concave convex mirrors and plano concave mirrors.

6.9.1 Concave-Concave $y\bar{y}$ Diagram Design with Different Radii of Curvatures of MPC Design

Similarly, in this design we use interlaced design where ($m=5$), $N=31$ but off axes input beam and $r_{01} = 25$, $r_{02} = 21.25$. The equations 6.11 and 6.16 will take care of geometrical optics convention signs. We noticed that, from Figure 6.8.1.1 the design has two circles of two semi-diameters of M1 beam intercepts $r_{01} = \sqrt{\bar{y}_{even}^2 + y_{even}^2}$ and M2 beam intercepts $r_{02} = \sqrt{\bar{y}_{odd}^2 + y_{odd}^2}$ as expected. The ray tracing also has very similar result, but the $y\bar{y}$ diagram slightly different because of the diagonal field of view and the right-hand rules. The first order

design of concave-concave $y\bar{y}$ diagram MPCs is shown in table 6.14, table 6.15, the repeated $y\bar{y}$ diagram values is shown in Figure 6.23, Figure 6.24, the ZEMAX design data are shown in Figure 6.25, Figure 6.26, programmed Excel file is attached on Appendix D. respectively.

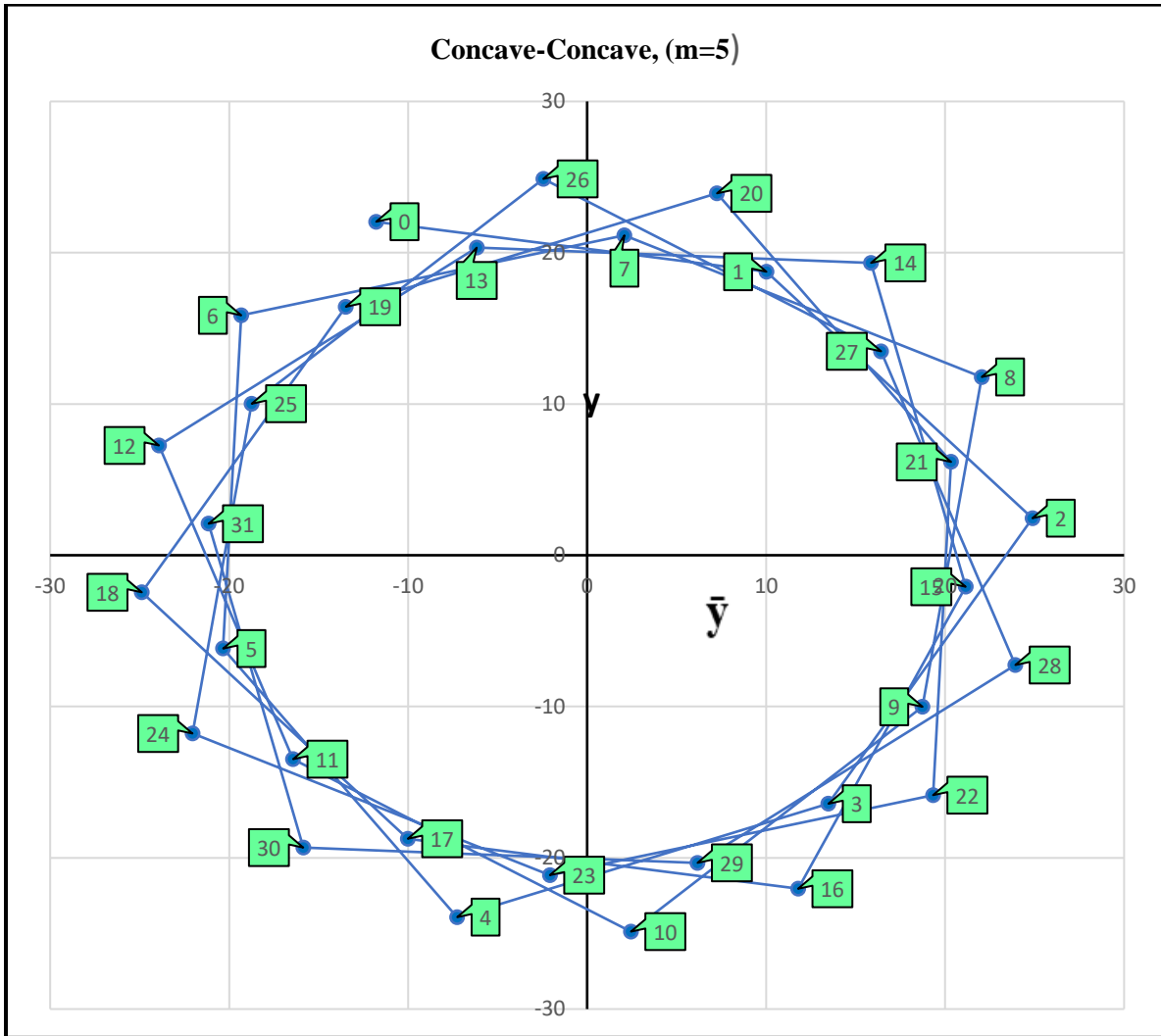


Figure 6.23 Concave-concave interlace $y\bar{y}$ diagram MPC plot.

Table 6.14 Description of first order interlaced concave-concave $y\bar{y}$ diagram MPC.

Properties	Allocated Values	Calculated Values	Brief Description
m	5		
r_{01}	25mm		
r_{02}	21.25		
Number of bounces(N)		31	$N=OAL/L$
Length (L)		75.552 mm	Cavity length $t1 = \frac{1}{Lg} \begin{bmatrix} y0 & \bar{y}0 \\ y1 & \bar{y}1 \end{bmatrix}$
$\Theta_m(\text{rad})$		0.981748	$\Theta_m = \frac{2\pi m}{N+1}$
\bar{y}_0, \bar{y}_1		-11.7849, 10.01784	$\bar{y}_n = r_n \sin\left(\Theta_m * \left(n - \frac{1}{2}\right)\right)$
y_0, y_1		22.04803, 18.74083	$y_n = r_n \cos\left(\Theta_m * \left(n - \frac{1}{2}\right)\right)$
EPD		40	$EPD=2 * y_0$
Lg		5.8465	$Lg = \left(2 r_0^2 \sin\left(\frac{\Theta_m}{2}\right) \cos\left(\frac{\Theta_m}{2}\right)\right) * \left(\frac{1}{L}\right)$
$\bar{U}(\text{rad})$		0.289	$\bar{U} = \frac{\bar{y}i + 1 - \bar{y}i}{t1}$
U(rad)		-0.044	$U = \frac{yi + 1 - yi}{t1}$
R1		143.1443 (concave)	$R=2EFL=\frac{1}{2\Phi_1}$
R2		218.09 (Concave)	$\Phi_2 = \frac{1}{Lg} \begin{bmatrix} u1 & \bar{u}1 \\ u2 & \bar{u}2 \end{bmatrix}$
g1g2 (Stability)		0.30866	$0 \leq g1g2 \leq 1$
FOV(X-direction)		16.096541°	$FOV=\text{atan}(\bar{U})$
FOV(Y-direction)		-2.506458	$FOV=\text{atan}(U)$

Table 6.15 Concave-concave interlaced $y\bar{y}$ diagram MPC design data.

N	\bar{y}	y
0	-11.7849	22.04803
2	24.87962	2.450429
4	-7.25712	-23.9235
6	-19.3253	15.85983
8	22.04803	11.78492
10	2.450429	-24.8796
12	-23.9235	7.257117
14	15.85983	19.32526
16	11.78492	-22.048
18	-24.8796	-2.45043
20	7.257117	23.92351
22	19.32526	-15.8598
24	-22.048	-11.7849
26	-2.45043	24.87962
28	23.92351	-7.25712
30	-15.8598	-19.3253

N	\bar{y}	y
1	10.01718	18.74083
3	13.48086	-16.4265
5	-20.335	-6.16855
7	2.082864	21.14768
9	18.74083	-10.0172
11	-16.4265	-13.4809
13	-6.16855	20.33498
15	21.14768	-2.08286
17	-10.0172	-18.7408
19	-13.4809	16.42647
21	20.33498	6.168549
23	-2.08286	-21.1477
25	-18.7408	10.01718
27	16.42647	13.48086
29	6.168549	-20.335
31	-21.1477	2.082864

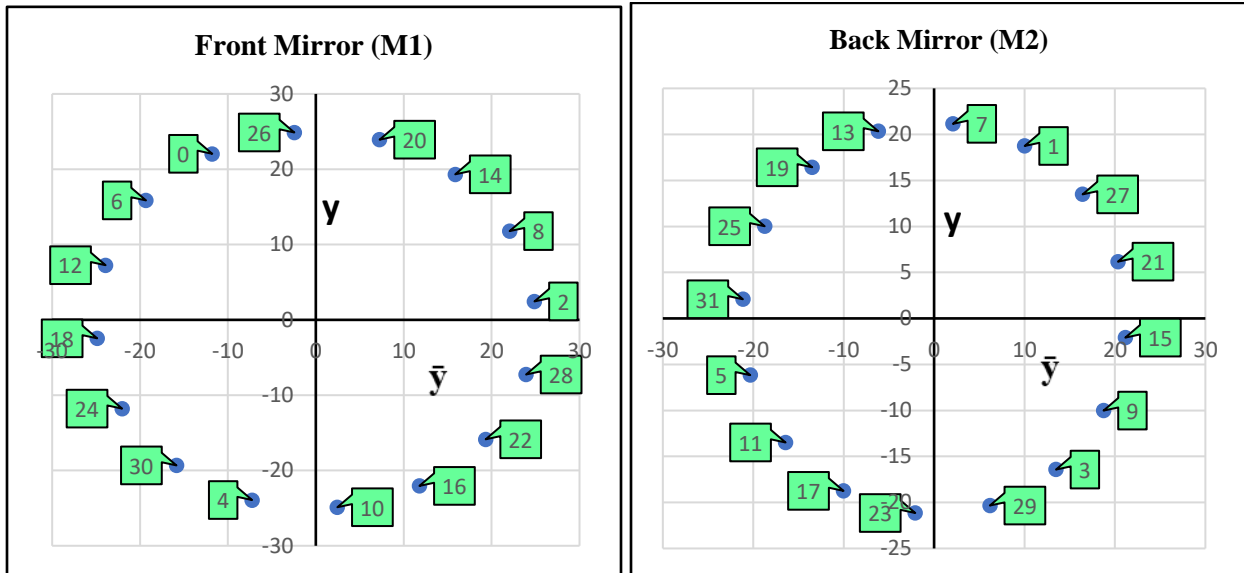


Figure 6.24 Interlace concave-concave $y\bar{y}$ diagram MPC intercepts M1, M2.

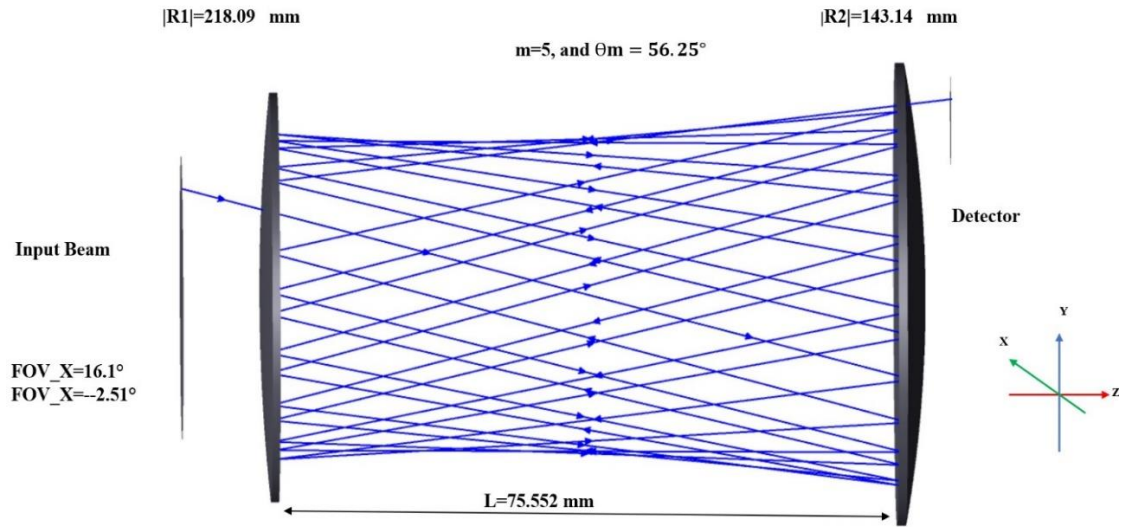


Figure 6.25 Concave-concave ray tracing simulation [7].

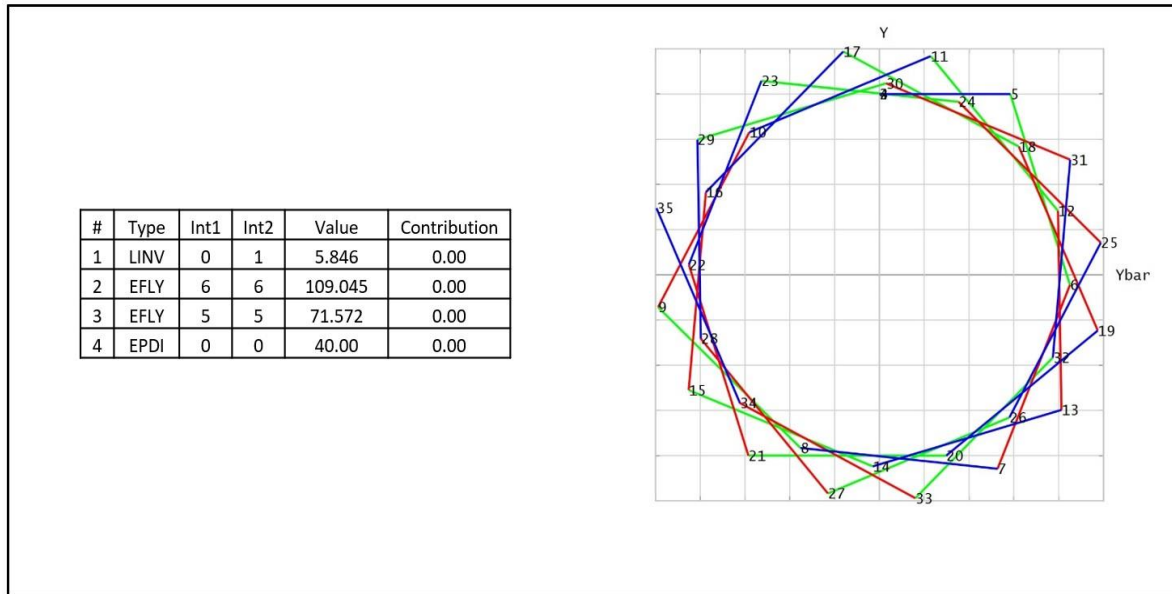


Figure 6.26 An image of concave-concave ray tracing simulation data [7].

6.9.2 Concave-Plano $y\bar{y}$ Diagram Design with Different Radii of Curvatures of MPC Design

Similarly, in this design we use interlaced design where ($m=5$), $N=31$ but off axes input beam, concave-plano mirrors and $r_{01} = 25$, $r_{02} = 13.89$. The equations 48 and 53 will take care of geometrical optics convention signs. We noticed from Figure 6.8.2.1 that, the concave-plano design only shows bending for the powered mirror and similarly there are two circles present M1 beam intercepts $r_{01} = \sqrt{\bar{y}_{even}^2 + y_{even}^2}$ and M2 beam intercepts $r_{02} = \sqrt{\bar{y}_{odd}^2 + y_{odd}^2}$ as expected. The first order design of concave-concave $y\bar{y}$ diagram MPCs is shown in table 6.16, table 6.17, the repeated $y\bar{y}$ diagram values are shown in Figure 6.27, Figure 6.28, the ZEMAX design data are shown in Figure 6.29, Figure 6.30 and an image of programmed Excel file is attached in Appendix D. respectively.

Table 6.16 Description of first order interlaced concave-plano $\bar{y}\bar{y}$ diagram MPC.

Properties	Allocated Values	Calculated Values	Brief Description
m	5		
r_{01}	25		
r_{02}	13.89		
Number of bounces(N)		31	$N=OAL/L$
Length (L)		75.552 mm	Cavity length $t1 = \frac{1}{Lg} \begin{bmatrix} y0 & \bar{y}0 \\ y1 & \bar{y}1 \end{bmatrix}$
$\Theta_m(\text{rad})$		0.981748	$\Theta_m = \frac{2\pi m}{N+1}$
\bar{y}_0, \bar{y}_1		-11.7849, 6.5477	$\bar{y}_n = r_n \sin\left(\Theta_m * \left(n - \frac{1}{2}\right)\right)$
y_0, y_0		22.04803, 12.24989	$y_n = r_n \cos\left(\Theta_m * \left(n - \frac{1}{2}\right)\right)$
EPD		27.78	$EPD=2 * \sqrt{\bar{y}^2 + y^2}$
Lg		3.81577	$Lg = \left(2 r_0^2 \sin\left(\frac{\Theta_m}{2}\right) \cos\left(\frac{\Theta_m}{2}\right)\right) * \left(\frac{1}{L}\right)$
$\bar{U}(\text{rad})$		0.243	$\bar{U} = \frac{\bar{y}i + 1 - \bar{y}i}{t1}$
U(rad)		-0.130	$U = \frac{yi + 1 - yi}{t1}$
R1		Plano	$R=2EFL=\frac{1}{2\Phi_1}$
R2		109.86 (Concave)	$\Phi_2 = \frac{1}{Lg} \begin{bmatrix} u1 & \bar{u}1 \\ u2 & \bar{u}2 \end{bmatrix}$
g1g2 (Stability)		0.3086	$0 \leq g1g2 \leq 1$
FOV(X-direction)		13.63915°	FOV=atan(\bar{U})
FOV(Y-direction)		-7.3893°	FOV=atan(U)

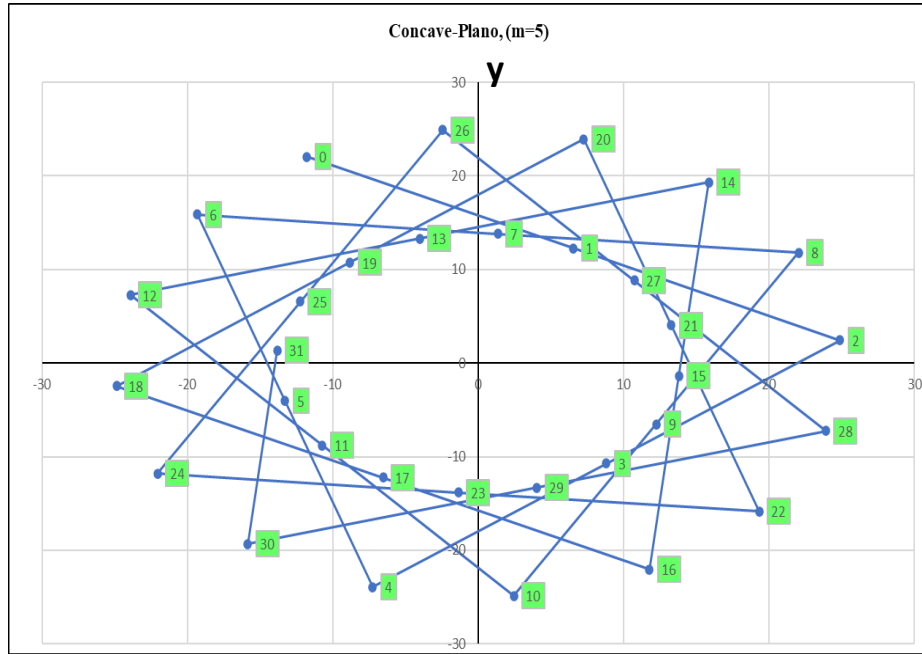


Figure 6.27 Concave-concave interlace \bar{y} diagram MPC plot.

Table 6.17 Concave-plano interlaced \bar{y} diagram MPC design.

N	\bar{y}	y
0	-11.7849184	22.04803
2	24.87961817	2.450429
4	-7.257116931	-23.9235
6	-19.32526133	15.85983
8	22.04803161	11.78492
10	2.450428508	-24.8796
12	-23.92350839	7.257117
14	15.8598321	19.32526
16	11.78491842	-22.048
18	-24.87961817	-2.45043
20	7.257116931	23.92351
22	19.32526133	-15.8598
24	-22.04803161	-11.7849
26	-2.450428508	24.87962
28	23.92350839	-7.25712
30	-15.8598321	-19.3253

N	\bar{y}	y
1	6.547701	12.24989
3	8.811723	-10.7371
5	-13.2919	-4.03205
7	1.361458	13.82312
9	12.24989	-6.5477
11	-10.7371	-8.81172
13	-4.03205	13.2919
15	13.82312	-1.36146
17	-6.5477	-12.2499
19	-8.81172	10.73712
21	13.2919	4.032054
23	-1.36146	-13.8231
25	-12.2499	6.547701
27	10.73712	8.811723
29	4.032054	-13.2919
31	-13.8231	1.361458

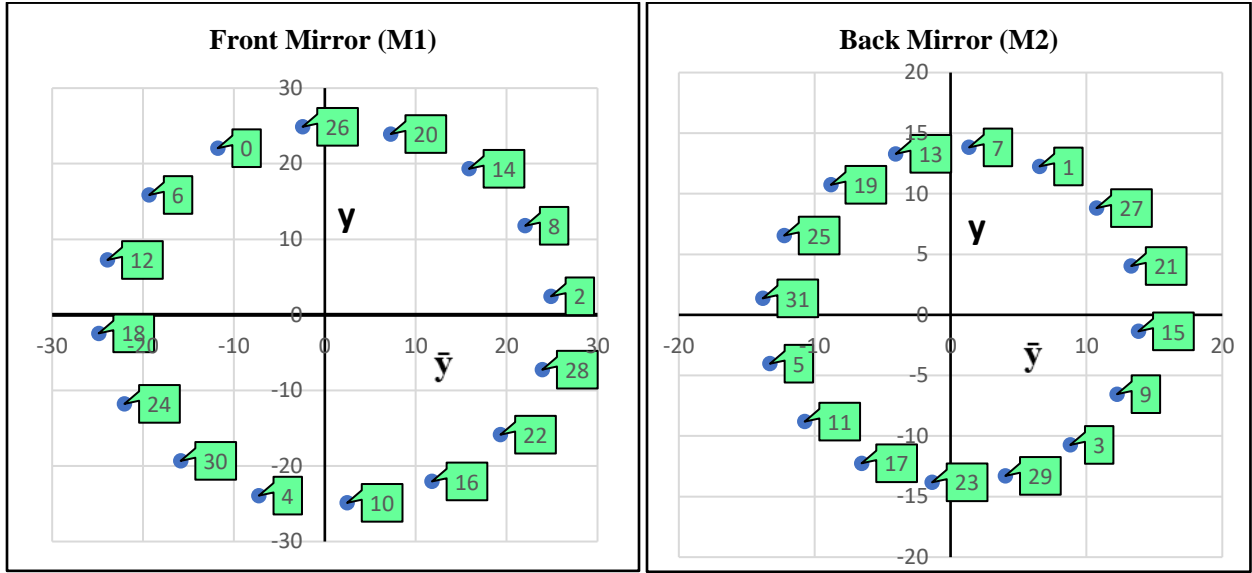


Figure 6.28 Interlace concave-plano $y\bar{y}$ diagram MPC intercepts M1, M2.

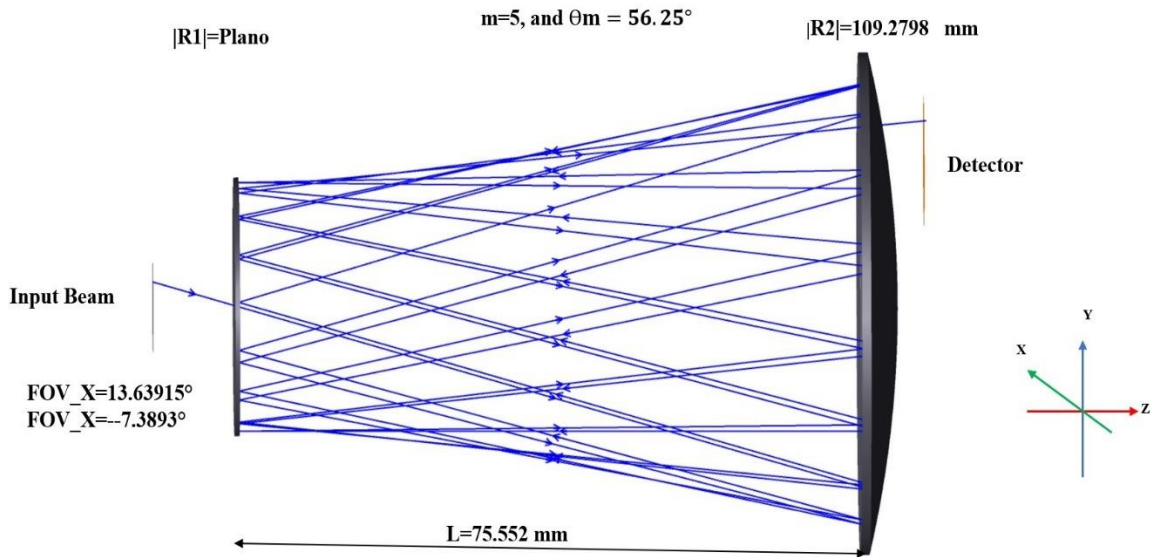


Figure 6.29 Concave-plano ray tracing simulation [7].

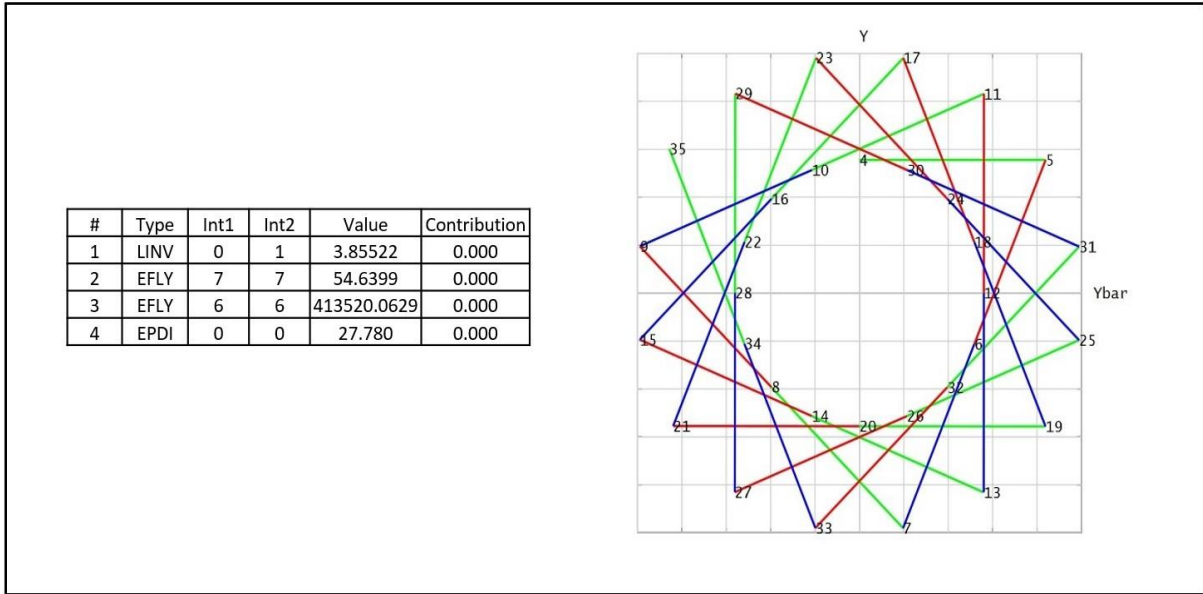


Figure 6.30 An image of concave-Plano ray tracing simulation data [7].

6.9.3 Concave-convex $y\bar{y}$ Diagram Design with different Radii of Curvatures of MPC Design

Similarly, in this design we use interlaced design where $(m=5)$, $N=31$ but off axes input beam, concave-convex and $r_{01} = 25 \text{ mm}$, $r_{02} = 7.58 \text{ mm}$. The equations 48 and 53 will take care of geometrical optics convention signs. We noticed from Figure 6.8.3.1 that the concave-convex solution, the segments alternately bend towards and away from the origin indicating the positive and negative powered mirror. We also noticed from Figure 6.8.3.1 that the design has two circles present M1 beam intercepts $r_{01} = \sqrt{\bar{y}_{even}^2 + y_{even}^2}$ and M2 beam intercepts $r_{02} = \sqrt{\bar{y}_{odd}^2 + y_{evenodd}^2}$ as expected. The first order design of concave-convex $y\bar{y}$ diagram MPCs is shown in table 6.18, table 6.19, the repeated $y\bar{y}$ diagram values are shown in Figure6.31, Figure6.32, the ZEMAX design data are shown in Figure 6.33, Figure 6.34 and an image of programmed Excel file is attached on Appendix D. respectively.

Table 6.18 Description of first order interlaced concave-plano $y\bar{y}$ diagram MPC.

Properties	Allocated Values	Calculated Values	Brief Description
m	5		
r_{01}	25		
r_{02}	7.58		
Number of bounces(N)		31	$N=OAL/L$
Length (L)		75.552 mm	Cavity length $t1 = \frac{1}{Lg} \begin{bmatrix} y0 & \bar{y}0 \\ y1 & \bar{y}1 \end{bmatrix}$
$\Theta m(\text{rad})$		0.981748	$\Theta m = \frac{2\pi m}{N+1}$
\bar{y}_0, \bar{y}_1		-11.7849, 3.5731	$\bar{y}_n = r_n \sin\left(\Theta m * \left(n - \frac{1}{2}\right)\right)$
y_0, y_0		22.04803, 6.68496	$y_n = r_n \cos\left(\Theta m * \left(n - \frac{1}{2}\right)\right)$
EPD		15.16	$EPD=2 * \sqrt{\bar{y}^2 + y^2}$
Lg		2.085497	Lg $= \left(2 r_0^2 \sin\left(\frac{\Theta m}{2}\right) \cos\left(\frac{\Theta m}{2}\right)\right)$ $* \left(\frac{1}{L}\right)$
$\bar{U}(\text{rad})$		0.203	$\bar{U} = \frac{\bar{y}i + 1 - \bar{y}i}{t1}$
$U(\text{rad})$		-0.203	$U = \frac{yi + 1 - yi}{t1}$
R1		90.85259	$\Phi 1 = \frac{1}{Lg} \begin{bmatrix} u0 & \bar{u}0 \\ u1 & \bar{u}1 \end{bmatrix}$
R2		90.773	$\Phi 2 = \frac{1}{Lg} \begin{bmatrix} u1 & \bar{u}1 \\ u2 & \bar{u}2 \end{bmatrix}$
$g1g2$ (Stability)		0.3086	$0 \leq g1g2 \leq 1$
FOV(X-direction)		11.49044°	FOV=atan (\bar{U})
FOV(Y-direction)		-11.49405°	FOV=atan (U)

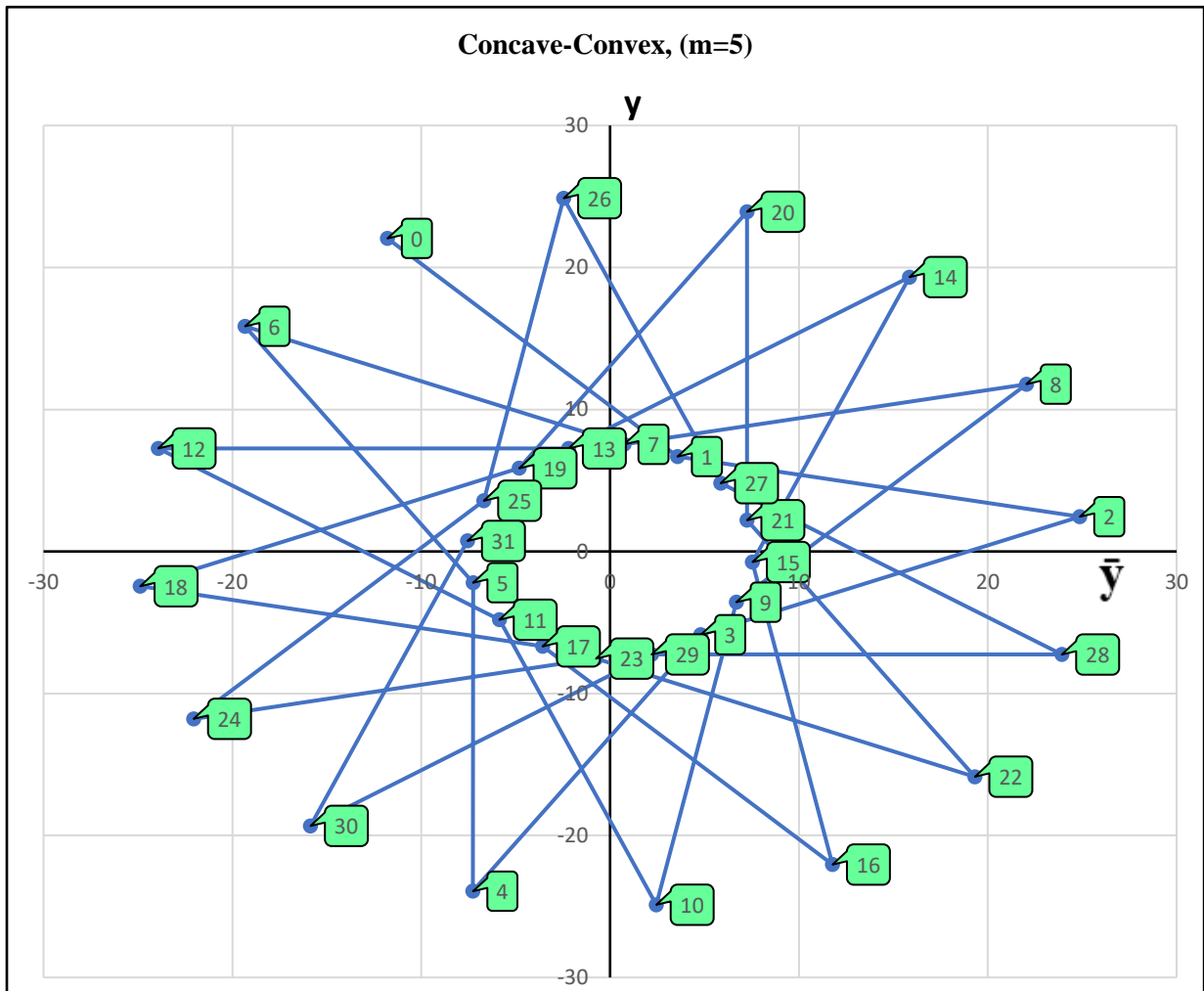


Figure 6.31 Concave-convex ray tracing simulation.

Table 6.19 Concave-convex interlaced $y\bar{y}$ diagram MPC design.

N	\bar{y}	y
0	-11.784918	22.04803
2	24.8796181	2.450429
4	-7.2571169	-23.9235
6	-19.325261	15.85983
8	22.048031	11.78492
10	2.4504285	-24.8796
12	-23.923508	7.257117
14	15.8598321	19.32526
16	11.7849184	-22.048
18	-24.87961	-2.45043
20	7.2571161	23.92351
22	19.32526	-15.8598
24	-22.04803	-11.7849
26	-2.450428	24.87962
28	23.92350	-7.25712
30	-15.8598	-19.3253

N	\bar{y}	y
1	3.573187	6.684963
3	4.808701	-5.85942
5	-7.25361	-2.20036
7	0.74297	7.5435
9	6.684963	-3.57319
11	-5.85942	-4.8087
13	-2.20036	7.253608
15	7.5435	-0.74297
17	-3.57319	-6.68496
19	-4.8087	5.859419
21	7.253608	2.200358
23	-0.74297	-7.5435
25	-6.68496	3.573187
27	5.859419	4.808701
29	2.200358	-7.25361
31	-7.5435	0.74297

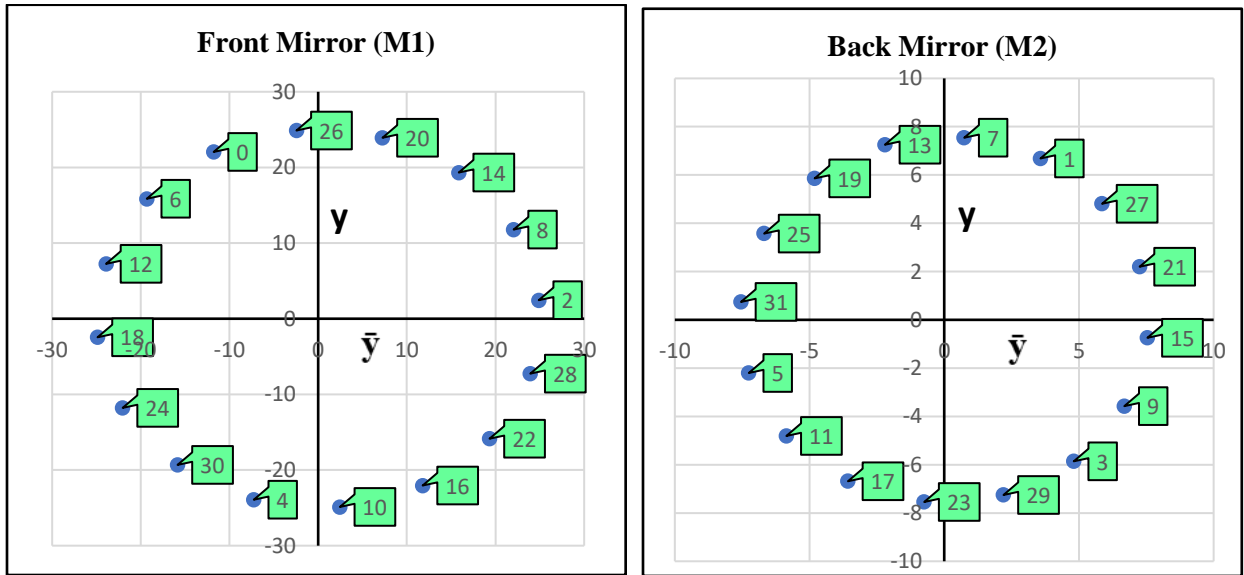


Figure 6.32 Interlace concave-convex $y\bar{y}$ diagram MPC intercepts M1, M2.

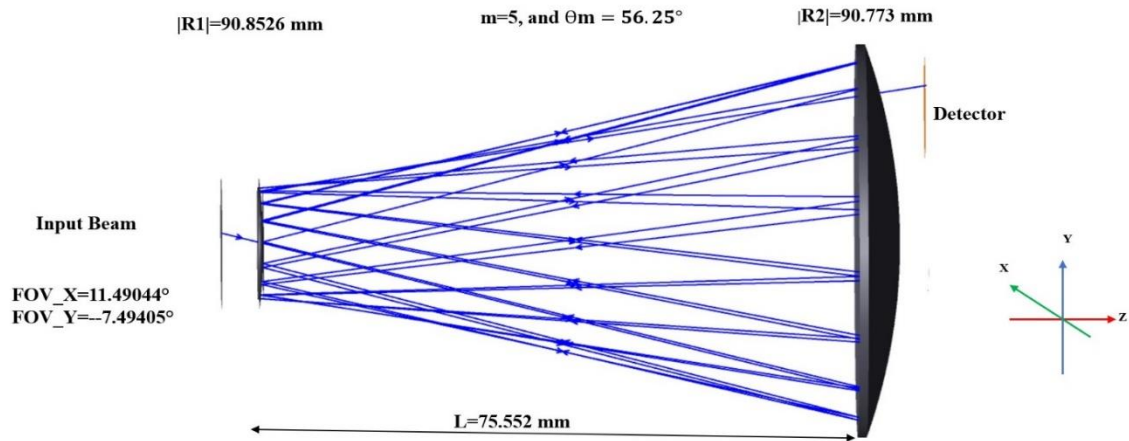


Figure 6.33 Concave-convex ray tracing simulation [7].

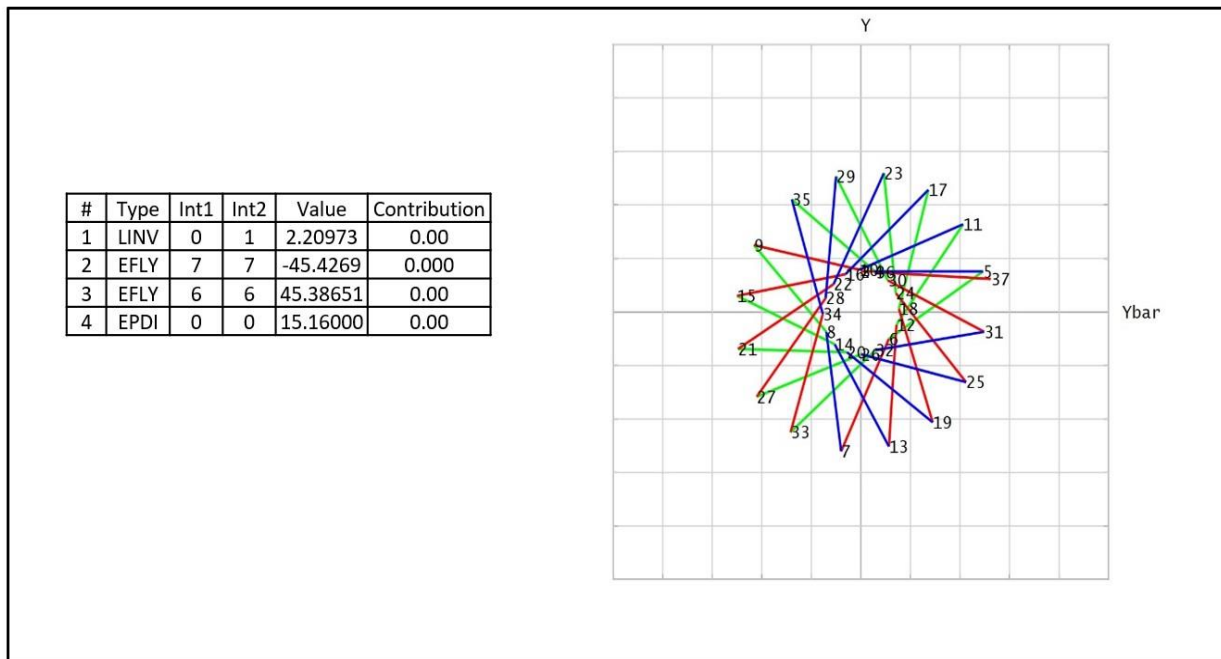


Figure 6.34 An image of concave-convex ray tracing simulation data [7].

Finally, we compared the previous section designs, in the other words, same system requirements; the cavity length and number of intercepts, but we manipulated the r_{01} & r_{02} and $m = 5$. That led to concave-concave, concave-convex and concave-plano cases, with different FOVs.

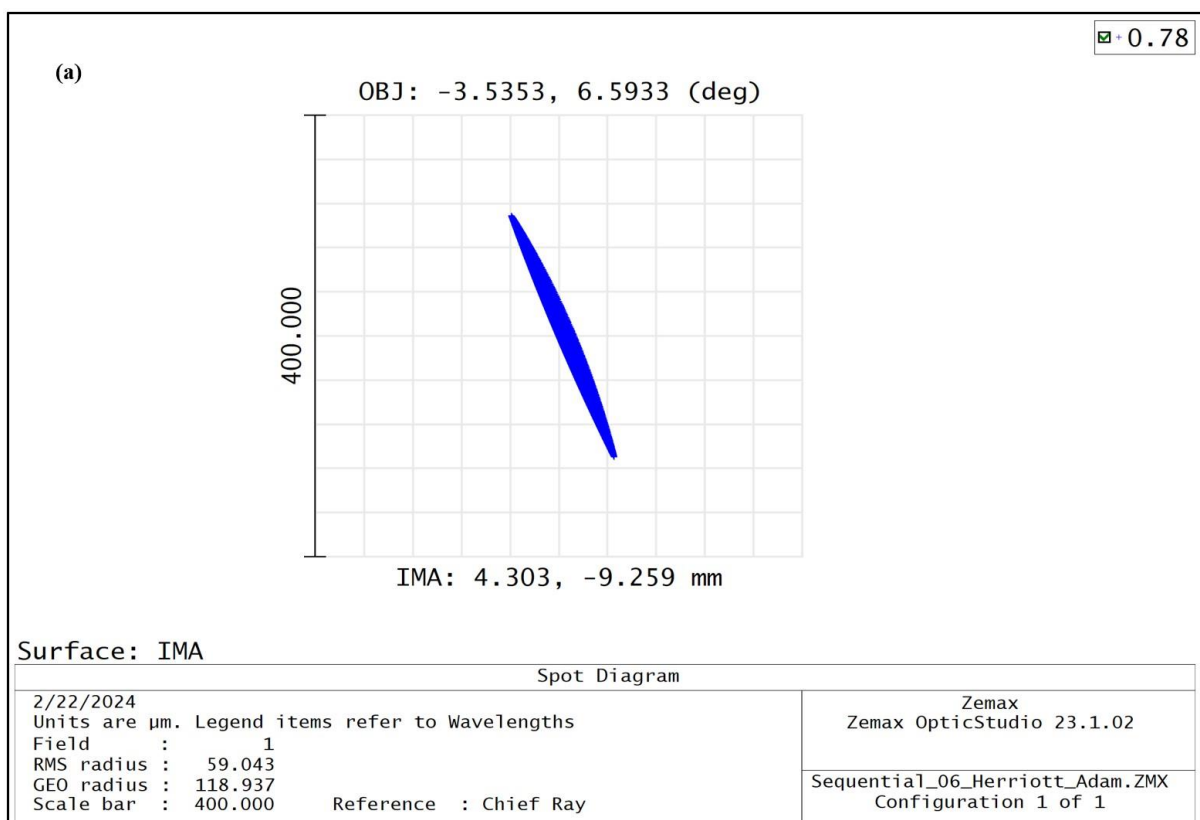
Table 6.20 Four different designs of gut ray MPCs including ROCs and FOVs using the $y\bar{y}$ diagram.

m	θ_m	R1	R2	r_{02}	r_{01}	x-angle	y-angle
3	33.75°	257.6 (Concave)	3459.62 (Concave)	25	21.25	10.08°	-2.72°
5	56.25°	218.09 (Concave)	143.14 (Concave)	25	21.25	16.1°	-2.51°
5	56.25°	90.86 (Convex)	90.86 (Concave)	25	7.58	11.49°	-11.49°
5	56.25°	109.28 (Concave)	Infinity (Plano)	25	13.89	13.64°	-7.39°

Chapter 7.

7.1 MPC off-Axis Astigmatism Aberration Background

The off-axis incidence input beam inside the MPC will lead to Astigmatism. By checking the Zemax design spot diagram, wavefront map and wavefront function for the design in section.5.6 as shown in Figure 7.1, it is obvious that the most dominant aberration in the system is Astigmatism.



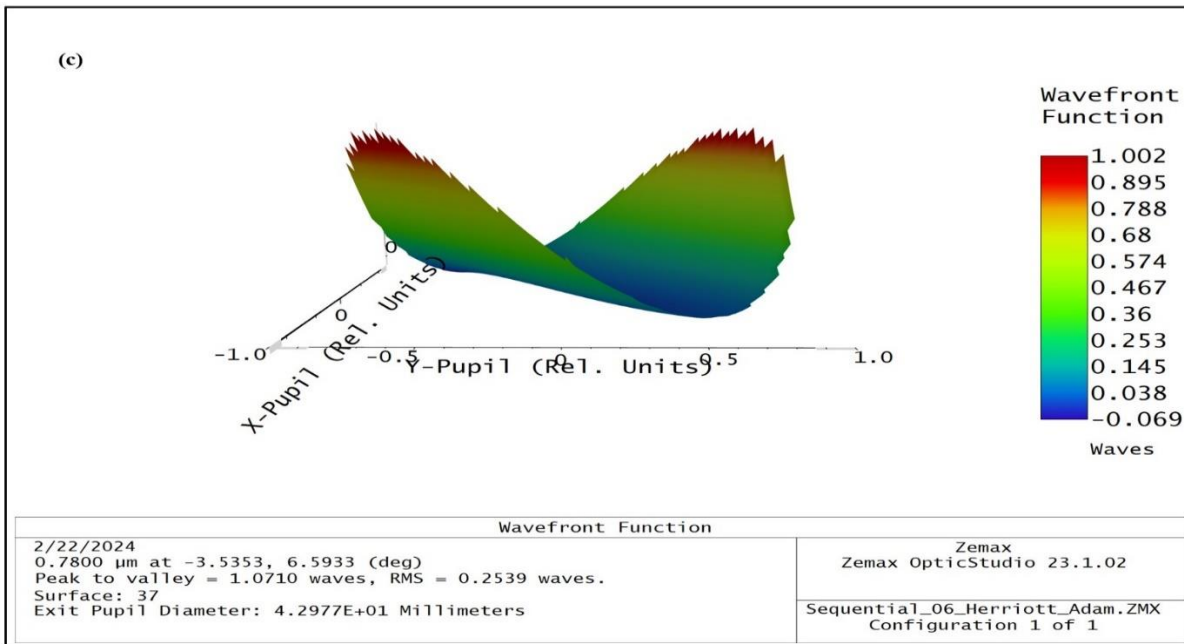
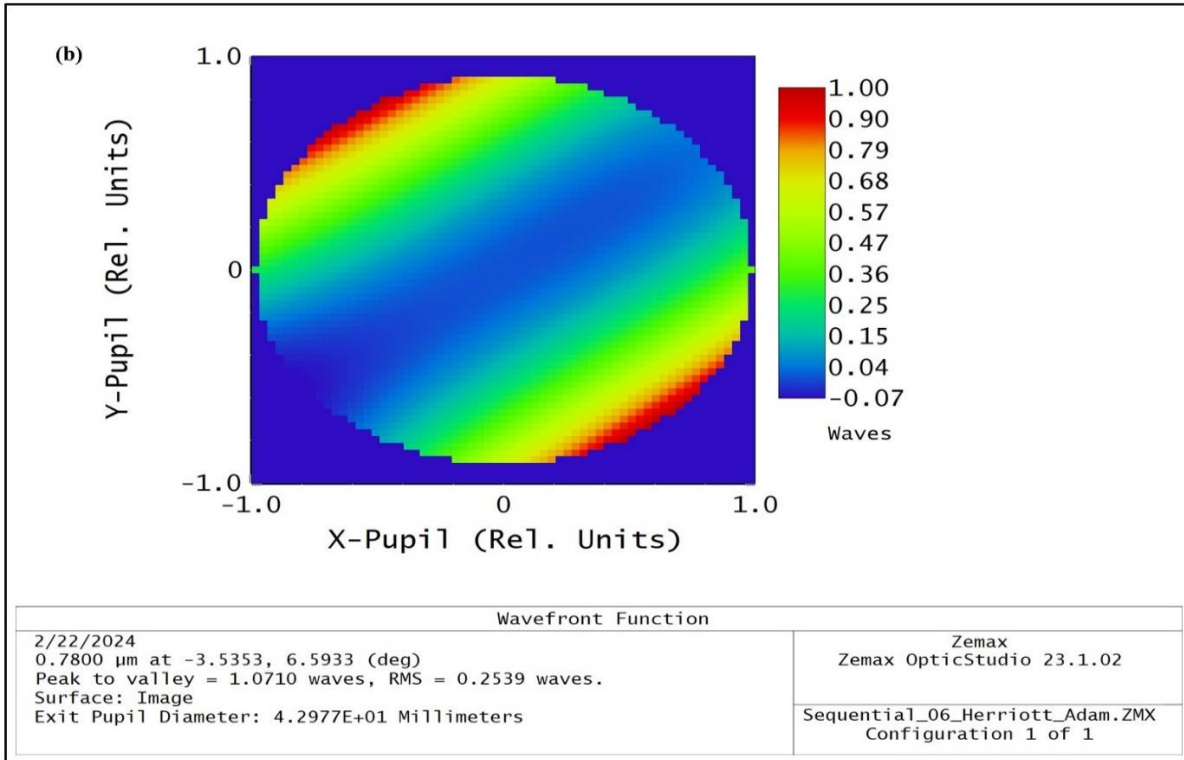


Figure 7.1 a) Spot diagram b) Wavefront function c) Wavefront map of Zemax design in section 5.6 [7].

In this section, we present Astigmatism aberration background and in the following sections, we demonstrate a novel approach of numerical calculation of Astigmatism Zernike fringe polynomials: terms Z_5 and Z_6 for an MPC.

Astigmatism is seen as a different focus position along the chief ray for tangential (y-direction) and sagittal (x-direction) respectively. Astigmatism occurs because the two orthogonal directions experience different geometrical optical power (Φ) as shown in Figure 7.2.

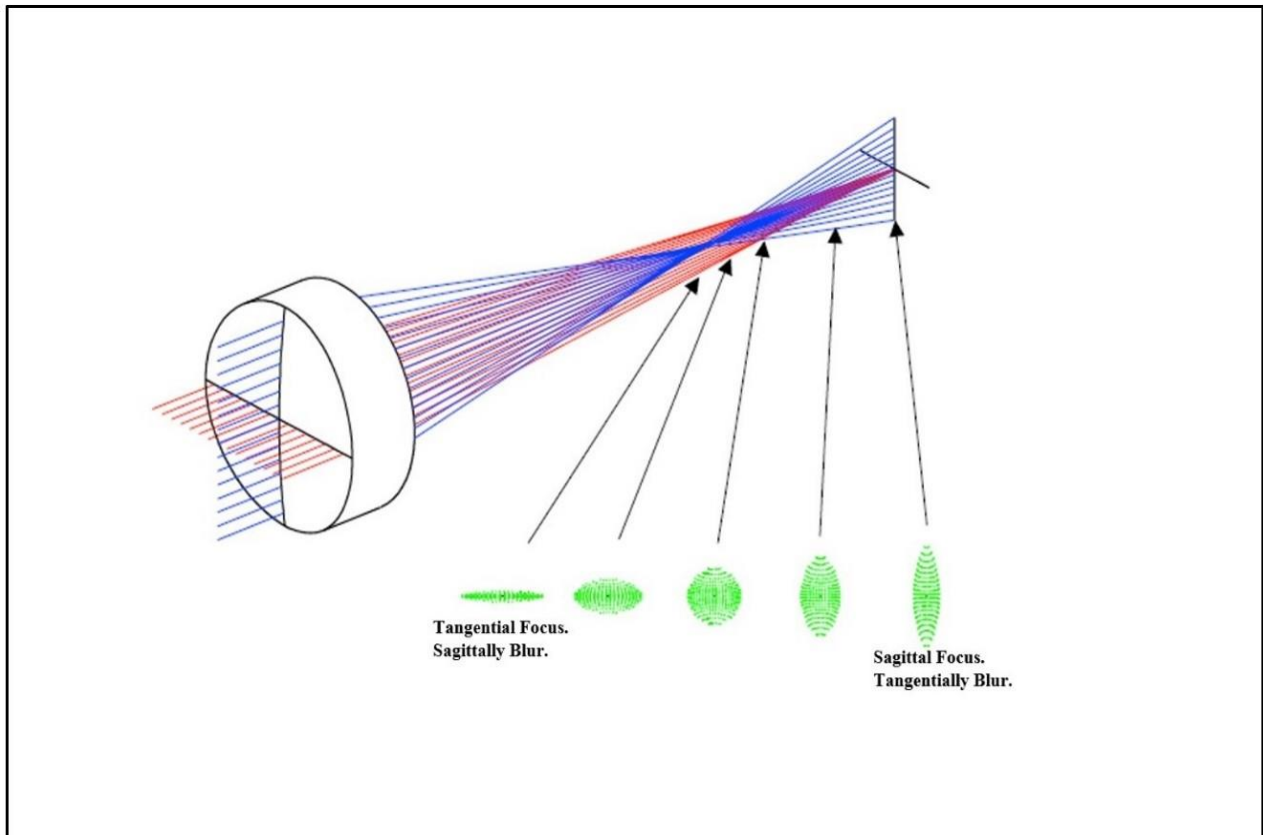


Figure 7.2 Astigmatism 3-D plot and corresponding spot diagram [6] [40] [41].

From Chapters 5 and 6, we demonstrated that the optical power for concave mirror is [6][32]:

$$|\Phi| = \left| \frac{2}{R} \right| = \left| \frac{1}{EFL} \right| = 2C. \quad (7.1)$$

Coddington's extended and modified equation 7.1 explicitly includes the off-axis angle. Oblique or slanted power (Φ_{OB}) is added for each single reflection [6][32][40] [41]:

$$|\Phi_{OB}| = |2C\cos(\bar{U})|. \quad (7.2)$$

The reason these power differences occur between on-axis and off-axis object points is that the ray experience different effective surface curvature as the field increases. Coddington present two equations for tangential power Φ_t and sagittal Φ_s as shown in equations 7.3 and 7.4 [6]:

$$|\Phi_t| = \left| \frac{\Phi_{OB}}{\cos^2(\bar{U})} \right| \quad (7.3)$$

$$|\Phi_s| = |\Phi_{OB}|. \quad (7.4)$$

Thus, we see that the Astigmatism is dependent quadratically on the chief ray angle.

7.2 Off-Axis MPC Seidel and Zernike Polynomials Astigmatism Aberration Background

Seidel polynomials are used to describe aberration for rotationally symmetric optical systems. We briefly discussed in Chapters 5, 6 that the advantage of using a symmetric, or collimated $y\bar{y}$ diagram is calculating an accurate aberration value. In the following section we use a collimated incident beam $y\bar{y}$ diagram to calculate an accurate value for Seidel Astigmatism value, then we decompose the result in x-direction and y-direction to obtain Zernike fringe polynomials: terms Z_5 and Z_6 .

Seidel introduced Astigmatism wavefront coefficient (W_{222}):

$$W_{222} = \left(\frac{S_m}{2\lambda} \right), \quad (7.5)$$

where Seidel coefficient (S_m) equal to [6]:

$$S_m = -\sum_0^N B_s^2 * (u_{N+1} - u_N) * y. \quad (7.6)$$

And the chief ray incidence angle (B_s^2) equal to:

$$B_s = n_{(refractive\ index)}(\bar{u} + \bar{y}c) \quad (7.7)$$

where, $n_{(refractive\ index)} = 1$ for air.

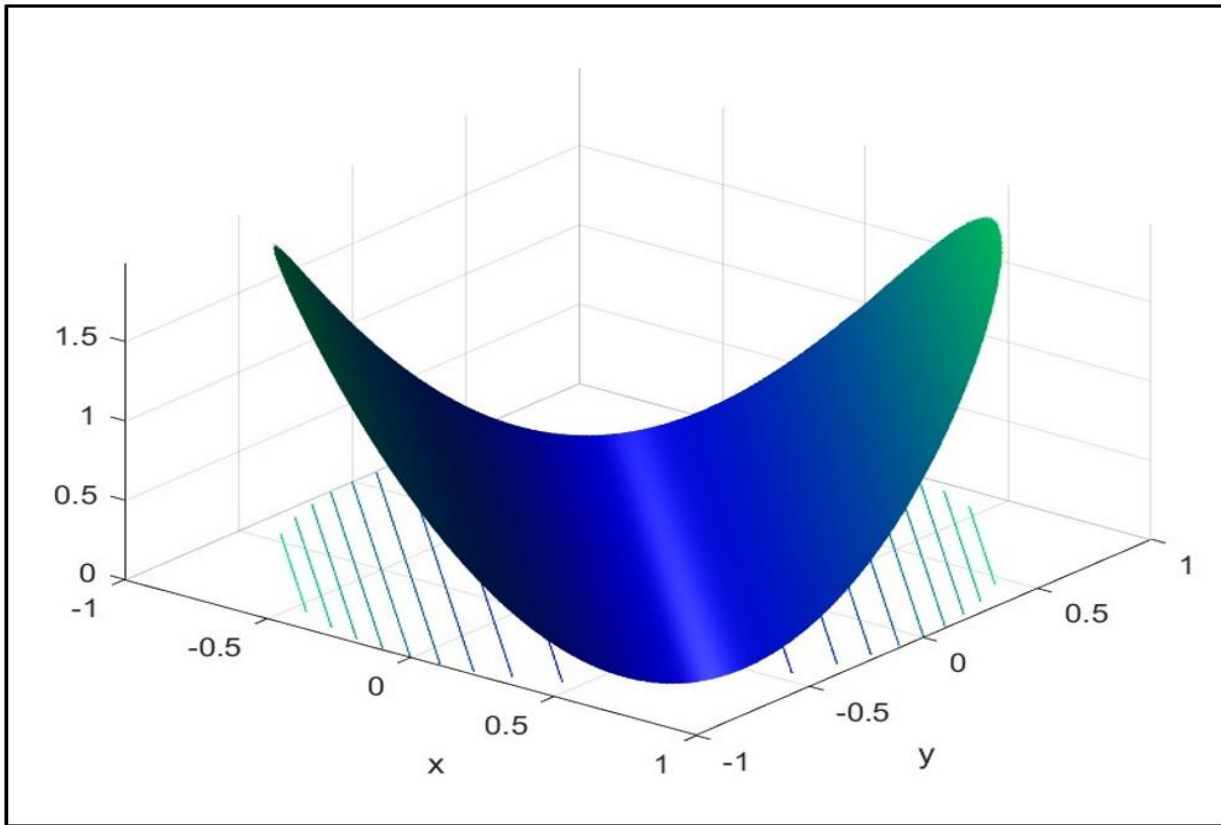


Figure 7.3 Astigmatism 3-D plot using Seidel W222 for circular exit pupil aperture [12].

Zernike's polynomials are orthonormal polynomials on a unit circle that are often used in optics as their forms tend to match common aberration terms (Seidel) and most optics have circular apertures. They are used to describe wavefronts from symmetric and non-symmetric optical systems. Calculating the Zernike coefficients using the Fringe (also called the "University of Arizona") polynomials is a common approach in optical design, fabrication and testing. As built

optical design performance can be obtained by inserting the measured 37 Zernike coefficients from an interferometer into a Zemax design model. The Zernike's coefficients of Astigmatism for x-direction (Z5) and y-direction (Z6) in units of waves as shown equations 7.9, to 7.10:

$$Z5 = \sum_0^N(\rho^2 \cos(2\Phi_z)) \quad (7.9)$$

$$Z6 = \sum_0^N(\rho^2 \sin(2\Phi_z)), \quad (7.10)$$

where Φ_z , ρ are the polar coordinates describing the wavefront, measured counterclockwise from the local x axis and the radial coordinate normalized.

7.3 Off-Axis MPC Astigmatism Aberration using $y\bar{y}$ Diagram Calculation

We can now employ our novel approach $y\bar{y}$ diagram to calculate the sagittal (Z5) and tangential(Z6) Zernike's coefficients through the MPC. Zernike's (Φ_z) rotation angle rotates in counterclockwise; thus, we follow Zernike's sign conventions. The approach is as follows. We note that the gut ray of the injected collimated laser beam (a skew ray) intercepts the mirror at a compound angle – both in x and y. Seidel calculations are made assuming the field of view is in one plane, typically the y-z plane. Reflections of all rays are in a single plane with the local normal of the reflecting surface, so we will replace the standard y-z plane angle of incidence with the compound angle of incidence: replacing Seidel's B with $\sqrt{A^2 + B^2}$. This takes care of the Seidel chief ray. To determine the marginal ray values needed for our calculation, we simply scale down the current collimated input marginal ray values to gut ray values, in other words, we calculate normalization factor (α) . Then, we need to account for the fact that the compound angle of incidence is rotating by Θ_m every reflection. So, unlike typical Seidel calculations where we add up the contribution from every surface, we decompose the calculated Seidel into an X and Y

components – Z5 and Z6. It is these values that can then be summed up for all the surfaces and then combined to get a “total Astigmatism.”

We first review the original design from Chapter 5 with identical concave mirrors.

To adapt the off-axis MPC to Seidel’s equations the following procedures will be needed it:

1. Use the $y\bar{y}$ diagram with the collimated input or rotate the $y\bar{y}$ diagram to make in collimated input form; (\bar{u}_r, ur) .
2. Calculate the gut ray incidence angle in x-direction and y-direction (Ar, Br) for rotated field of views, $Ar = u_r + yr/R$ & $Br = \bar{u}_r + \bar{y}r/R$.

3. Calculate the magnitude of incidence angles to obtain symmetric incidence angle,

$$B = \sqrt{Ar^2 + Br^2} \quad \& \quad B^2 = Ar^2 + Br^2.$$

4. Calculate the normalization factor for the gut ray entrance pupil diameter (EPDg) and collimated ray entrance pupil diameter (EPDr) $\alpha = EPDg/EPDr$.

5. Calculate normalized Sm(symmetric) $= \alpha^2 B^2 * (u_{rN+1} - u_{rN}) * yr$

6. Calculate new W222(symmetric) $= \left(\frac{Sm(symmetric)}{2\lambda} \right)$.

7. Decompose the W222(symmetric) to cosine and sine functions,

$$Z5 = W222(symmetric) * \frac{\cos(2*\theta_m*N)}{2} \quad \& \quad Z6 = W222(symmetric) * \frac{\sin(2*\theta_m*N)}{2}$$

We recap the created new equations for Z5, Z6 decomposition for MPC from Eqn.7.11 to eqn.7.18 to avoid ambiguity:

$$W222(symmetric) = \left(\frac{Sm(symmetric)}{2\lambda} \right) \tag{7.11}$$

$$Sm(symmetric) = -\sum_0^N \alpha^2 * B^2 * (u_{rN+1} - u_{rN}) * yr \tag{7.12}$$

$$Ar = u_r + yr/R \tag{7.13}$$

$$Br = \bar{u}_r + \bar{y}r/R \tag{7.14}$$

$$B^2 = Ar^2 + Br^2 \quad (7.15)$$

$$\alpha = \frac{EPDg}{EPDr} = \frac{XPDg}{XPDr} \quad (7.16)$$

$$Z5 = \sum_0^N W222(\text{symmetric}) * \frac{\cos(2 * \theta_m * N)}{2} \quad (7.17)$$

$$Z6 = \sum_0^N W222(\text{symmetric}) * \frac{\sin(2 * \theta_m * N)}{2}. \quad (7.18)$$

The step-by-step Z5 and Z6 calculation diagram is shown in Figure 7.4, and Table 7.2. The first order data are shown in Table 7.1

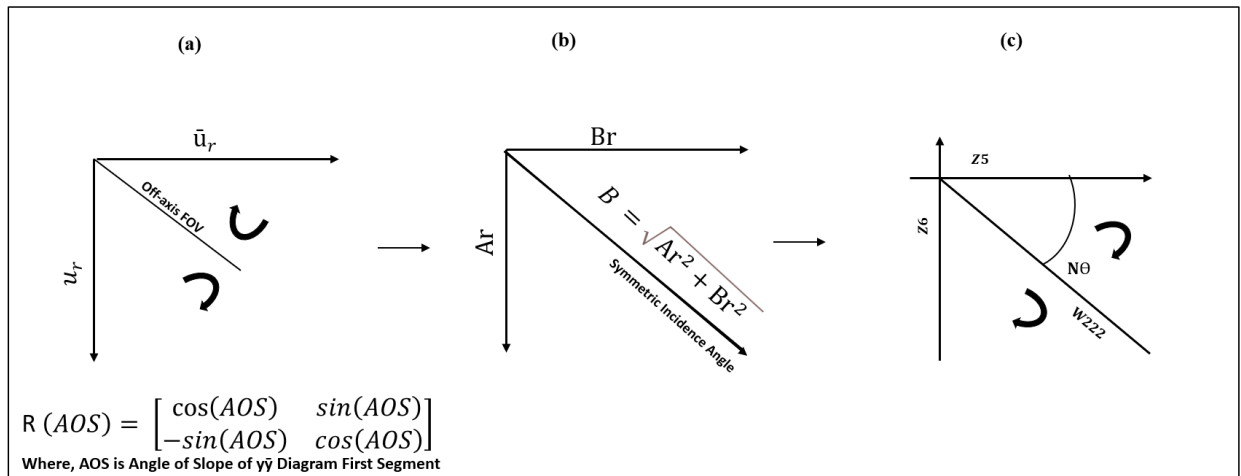


Figure 7.4 Column (a) Rotated Field of view (b) symmetric field of view magnitude (c) decomposition of W222.

Table 7.1 Description of first order step-by-step Zernike's coefficient calculation for the first bounce on M2.

Properties	Allocated Values	Calculated Values	Brief Description
m	5		
r ₀		10.414	
Number of bounces(N)		31	N=OAL/L
Length (L)		75.552 mm	Cavity length $t1 = \frac{1}{Lg} \begin{bmatrix} y0 & \bar{y}0 \\ y1 & \bar{y}1 \end{bmatrix}$
θ _m (rad) First Intercept		0.981748	θ _c = N * θ _m $\theta_m = \frac{2\pi m}{N+1}$ n=0 to N=31
\bar{y}_0		10.414	$\bar{y}_n = r_0 \cos(n\theta_m)$
y ₀		0	$y_n = r_0 \sin(n\theta_m)$
α		0.108	$\frac{EPDg}{EPDr} = \frac{XPDg}{XPDr}$
\bar{U}_{r1} (rad) First Intercept		-0.129953558	$\bar{U}_1 = \frac{\bar{y}_1 - \bar{y}_0}{t1}$ n=0 to N=31
U _{r1} (rad) First Intercept		2.35117E-17	$U_1 = \frac{y_1 - y_0}{t1}$ n=0 to N=31
C First Intercept		0.005882436 (Concave)	$\Phi_1 = \frac{1}{Lg} \begin{bmatrix} u0 & \bar{u}0 \\ u1 & \bar{u}1 \end{bmatrix}$ $R=2EFL=\frac{1}{C}$ n=0 to N=31
Ar ₁ (rad) First Intercept		-0.05403	$Ar = u_r + yr/R$ n=0 to N=31
Br ₁ (rad) First Intercept		0.101075943	$Bs = n(\bar{u} + \bar{y}c)$ n=0 to N=31

AOI (B^2) Angle of incident		0.01313	$B^2 = Ar^2 + Br^2$ $n=0$ to $N=31$
Sm1(symmetrical)		-0.000154	Sm(symmetrical) $= - \sum_0^N \alpha^2 * B^2$ $* (u_{rN+1} - u_{rN}) * yr$ $n=0$ to $N=31$
W222(um) First Intercept		-0.09906	$W222 = \left(\frac{Sm(symmetrical)}{2\lambda} \right)$ $n=0$ to $N=31$
Z5 First Intercept		0.0159883	Z5 $= \sum_0^N W222(symmetrical)$ $* \frac{\cos(2 * \theta_m * N)}{2}$ $n=0$ to $N=31$
Z6 First Intercept		-0.0385992	Z6 $= \sum_0^N W222(symmetrical)$ $* \frac{\sin(2 * \theta_m * N)}{2}$ $n=0$ to $N=31$

As expected from the geometry, the skew ray angle of incidence is the same on every mirror. But because the marginal ray is changing, the Seidel contribution at each surface is different. After the above procedures we compared the Z5, Z6 data with Zemax Zernike's Z5 and Z6 coefficients after each single intercept for proof of concept. We noticed that the Z5 calculated data is slightly lower than Zemax Z5 data and the Z6 calculated data are slightly higher than the Z6 data. Then, we compared calculated total Zernike Astigmatism, or the root sum square (RSS) as shown in Eqn.7.19, with the Zemax data and found that the results are essentially identical. The comparison data are shown in Figure 7.5, Figure 7.6, Figure 7.7 and Table 7.3:

$$\text{Total Astigmatism} = \text{RSS} = \sqrt{Z5^2 + Z6^2} \quad (7.19)$$

Table 7.2 Step-by- step Z5 and Z6 calculation.

Step-by-Step	Brief Description
$(\bar{u}_r, ur), (\bar{y}_r, yr),$	Rotate the gut ray to obtain collimated $y\bar{y}$ diagram
$Ar = u_r + yr/R \ \& \ Br = \bar{u}_r + \bar{y}_r/R.$	Calculate the incidence angles for rotated $y\bar{y}$ diagram
$\alpha^2 = (EPDg/EPDr)^2$	Calculate the normalization factor for the gut ray entrance pupil ($EPDg$) and the collimated $y\bar{y}$ diagram entrance pupil diameter ($EPDr$)
$B = \sqrt{Ar^2 + Br^2} \ \& \ B^2 = Ar^2 + Br^2$	Calculate the magnitude of incidence angle to obtain compound angle of incident
$Sm = \alpha^2 B^2 * (u_{rN+1} - u_{rN}) * yr$	Calculate normalized Seidel coefficients
$W222 = \frac{Sm}{2\lambda}$	Calculate normalized W222
$Z5 = W222 * \frac{\cos(2 * \Theta_m * N)}{2}$	Decompose The W222
$Z6 = W222 * \frac{\sin(2 * \Theta_m * N)}{2}$	Decompose The W222
Total Astigmatism = $\sqrt{Z5^2 + Z6^2}$	Calculate total Astigmatism

Table 7.3 Comparison between calculated Zernike's coefficients and ray tracing data.

N	Calculated(Z5)	Z5 (Zemax)	Calculated(Z6)	Z6 (Zemax)
1	0.0189543	0.0192441	-0.0457598	-0.0457985
2	0.0193869	0.0190673	-0.0453272	-0.0451643
3	-0.0157687	-0.0161864	-0.0307652	-0.0314361
4	-0.0157687	-0.0142027	-0.0890800	-0.0902706
5	-0.0108111	-0.0100833	-0.0890800	-0.0873772
6	-0.0289333	-0.0291751	-0.0689043	-0.0699118
7	-0.0530688	-0.0495003	-0.1271725	-0.1303873
8	-0.0389180	-0.0360546	-0.1271725	-0.1288990
9	-0.0443332	-0.0432079	-0.1140988	-0.1153684
10	-0.0889298	-0.0831051	-0.1586954	-0.1645902
11	-0.0652520	-0.0590322	-0.1685031	-0.1723523
12	-0.0652520	-0.0612299	-0.1631370	-0.1652211
13	-0.1191278	-0.1111522	-0.1854531	-0.1941885
14	-0.0922209	-0.0813022	-0.2123600	-0.2190917
15	-0.0919867	-0.0836126	-0.2117948	-0.2158265
16	-0.1415168	-0.1314241	-0.2117948	-0.2229289
17	-0.1225624	-0.1057196	-0.2575546	-0.2680781
18	-0.1221298	-0.1082497	-0.2571220	-0.2644089
19	-0.1572855	-0.1445041	-0.2425600	-0.2553113
20	-0.1572855	-0.1337721	-0.3008748	-0.3162163
21	-0.1523279	-0.1319698	-0.2988213	-0.3103980
22	-0.1704501	-0.1535181	-0.2806991	-0.2945345
23	-0.1945855	-0.1643974	-0.3389673	-0.3599953
24	-0.1804347	-0.1524870	-0.3389673	-0.3554324
25	-0.1858500	-0.1626149	-0.3258936	-0.3411134
26	-0.2304466	-0.1942569	-0.3704902	-0.3975006
27	-0.2067688	-0.1697771	-0.3802979	-0.4020280
28	-0.2067688	-0.1749723	-0.3749318	-0.3928489
29	-0.2606446	-0.2193160	-0.3972479	-0.4296636
30	-0.2337376	-0.1860647	-0.4241548	-0.4516989
31	-0.2335035	-0.1860647	-0.4235896	-0.4516989

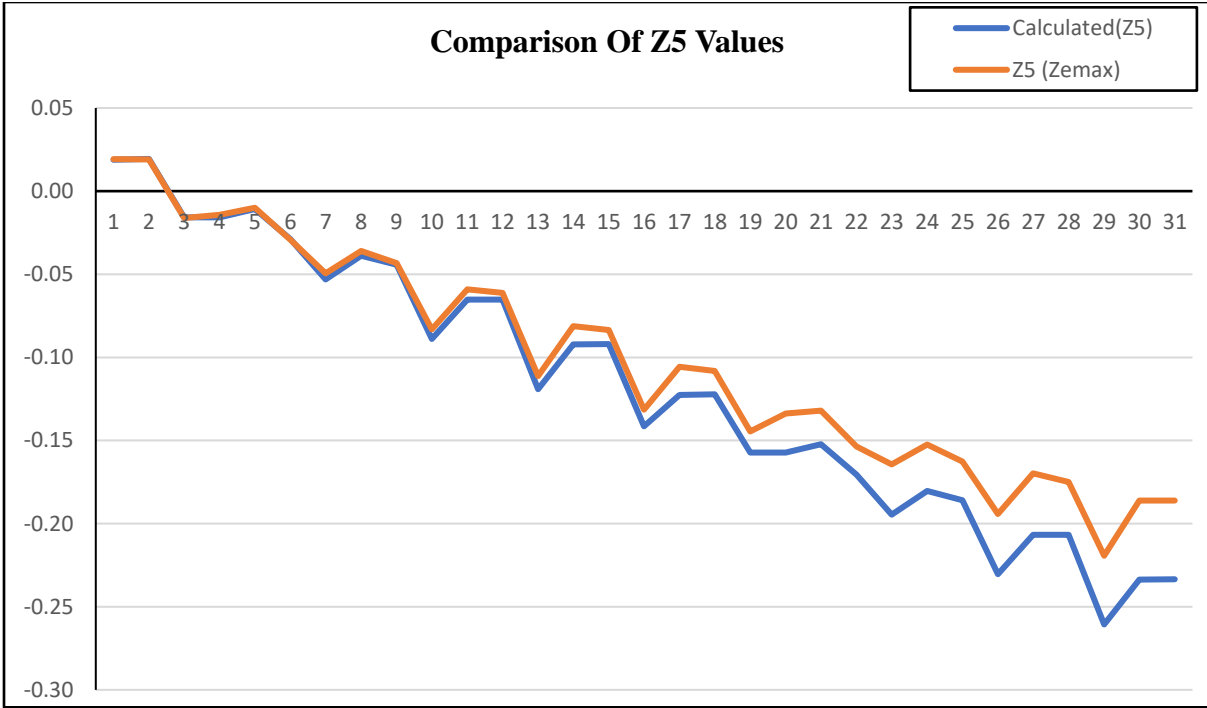


Figure 7.5 Z5 comparison between calculated Zernike's coefficients and ray tracing data.

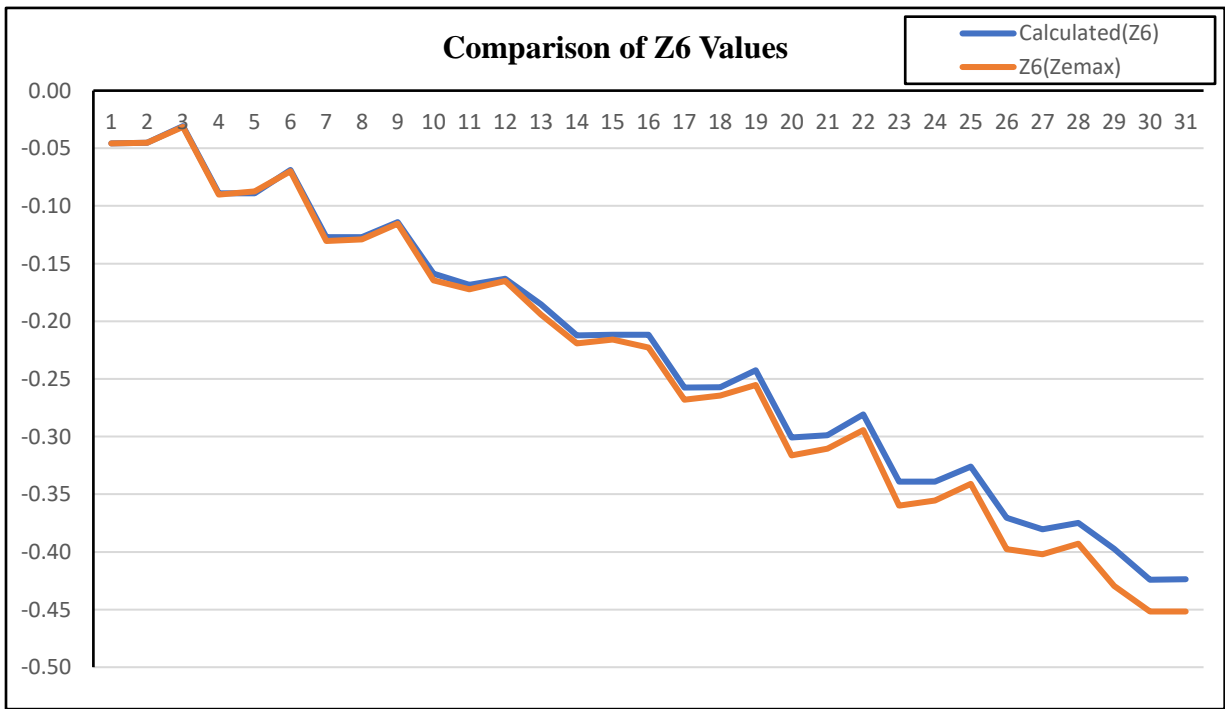


Figure 7.6 Z6 comparison between calculated Zernike's coefficients and ray tracing data.

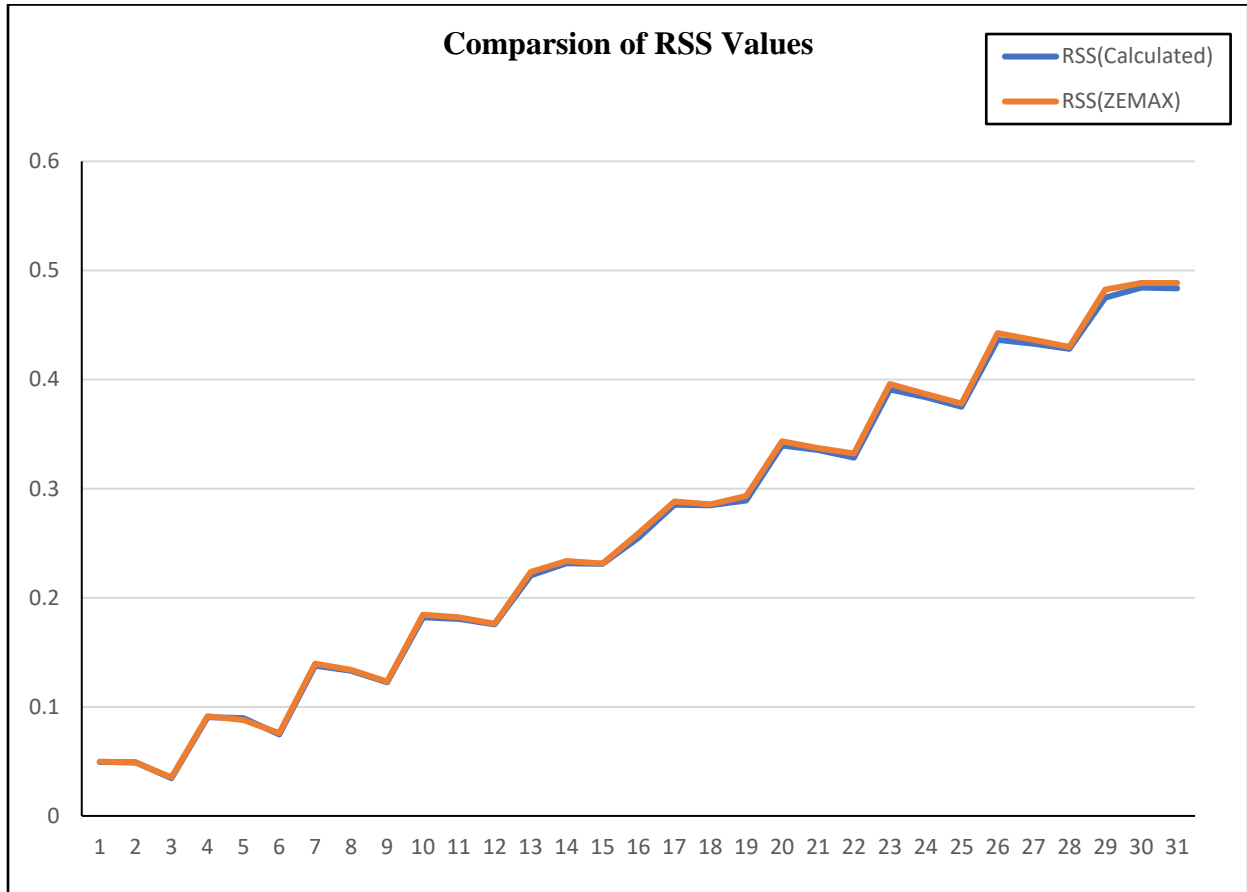


Figure 7.7 RSS comparison between calculated Zernike’s coefficients and ray tracing data.

Thus, we can now use this procedure to rapidly evaluate the total Astigmatism for a basic Herriott-like MPC with different “m” values to find the one with the least astigmatism, as shown in 7.4.

Table 7.4 Comparison between calculated Zernike's coefficients for m1,3 and 5.

m	Z5	Z6	RSS
1	-0.000816	-0.000186	0.0008368
3	-0.05252	-0.040699	0.0664438
5	-0.233504	-0.423589	0.4836858

We noticed that by increasing the clocking angle Θ_m , in another words, increasing m and decreasing the mirrors RoCs the total Astigmatism will be increased.

Chapter 8.

8.1 Summary and Conclusions

In this dissertation, we present Hybrid Gaussian Beam Decomposition which employs more than one size gaussian beamlet and a quantified equation for square aperture for any GBD approach. The goal of the approach is to increase the accuracy of the model's representation for sharp edged field distributions by using narrower gaussian beamlets at the edges, but reducing the necessary computation by employing broader gaussian beamlets where the field distribution is slowly varying. We show comparisons for a simple analytically derivable solution –square aperture diffraction in the far field and near field – calculated using standard FFT approaches, standard GBD and the new hybrid GBD method introduced here. We show how the HGBD achieves better matching to the FFT based approaches for the higher spatial frequency effects with a reduction in the required ray tracing effort.

We also demonstrate a new technique for designing Herriot MPCs, a novel, rapid and more intuitive approach using the $y\bar{y}$ diagram. The method was shown to be easily modified, leading to designs with different RoC's. All equations needed for programming were presented, as well as a step-by-step approach. By employing standard $y\bar{y}$ relations, the mirror radii are calculated, providing all the parameters necessary for entering the solution into a lens design program.

Furthermore, we coupled both gaussian beam analysis into the design and third order aberration analysis for astigmatism to evaluate the quality of the probe beam.

8.2 Future Work

The research presented here is only a first order design of MPC and an initial characterizing of dominant 3rd order astigmatism aberration. More work can still be done to optimize the real ray design. We discussed and demonstrated in Chapter 7 a new numerical approach to calculate 3rd order aberrations such as stigmatism, but we didn't present optimization (correction) methodology for 3rd aberrations. Astigmatism, spherical and coma will contribute to overall MPC performance and could be calculated with same methodology in Chapter 7. Further research can explore evaluating or optimizing an MPC to minimize aberrations. This could include the addition of Asphericity to the mirrors – paraboloidal, ellipsoidal, hyperboloidal mirrors.

However, initially, there are several variables that could be evaluated in an optimization. It was shown in Chapter 7, that the amount of astigmatism for a specific design varied with the selected m . This is not unexpected since this changes the radius of the mirrors and the clocking angle will change the Seidel astigmatism calculation at each surface and the clocking angle will affect how the aberrations decompose. This can also include the addition of varying the radius of curvature of the two mirrors. A further variable in the aberration of a design that could be investigated is the adjustment of K_m with an arbitrary constant. This would allow one to alter how the decomposition of aberration into Z_5 and Z_6 terms, changing the summed total astigmatism.

All of these things are now readily and rapidly achievable with this new $y\bar{y}$ framework for designing MPC's. To try to achieve this optimization in Zemax or CodeV would be

extremely complex. For one thing, the designer would have to create constraints in the optical design merit function that ensure that the beam footprints fall on a circle, that the intercepts do not overlap. That would require many lines of code – at least 31 for a 31-bounce design just to ensure the first constraint. Additionally, optimizations tend to find what are known as the “local minimum.” The optical design code evaluates the design against the defined merit function, then perturbs each variable to determine the sensitivity of the merit function to that variable. This matrix is solved to find the design that improves the Merit function value. It is as if you are standing in a field at night looking for the lowest point with a flashlight that only works when you point it straight down and it only illuminates a small area around your feet. You see the local slope of the terrain, take a step in that direction and repeat. This will lead you to a low portion of the field, but not necessarily the lowest depending on where you start. Changing the m value would not be a local move, so an optical design code would likely never make that step during an optimization. Zemax and CodeV do have what are known as “global optimization” modes, but the changes made when changing m are very discrete, so finding them may take a prohibitively long time. And the difficulty would still be in building a complete merit function that is valid for all m values. The $y\bar{y}$ approach avoids all of these complexities and provides a method which produces designs that automatically meet all specifications.

References

- [1] D. Herriott, H. Kogelnik and R. Kompfner, "Off-axis Path in Spherical Mirror Interferometer," *Applied Optics*, vol. 3, no. 4, pp. 523-526, (1964).
- [2] P. Mudgett and *et al.*, "Laser Spectroscopy Multi-Gas Monitor: Results of a Year Long Technology Demonstration on ISS," *ICES*, pp. 2015-243, (2015).
- [3] J. R. Pierce, *Theory and Design of Electron Beams*, New York: Van Nostrand, New York, (1954), pp. 194-197.
- [4] W. J. Smith, *Modern Optical Engineering*, 3, Ed., The McGraw Hill companies, Inc, 2000.
- [5] R. R. Shannon, *The Art and Science of Optical Design*, Cambridge: Cambridge University Press, (1997).
- [6] J. M. Geary, *Introduction to Lens Design*, Virginia: Willmann Bell, Inc, (2002).
- [7] *OpticStudio Physical Optics User Manual*, Zemax license "Act-1050511-1-1433766350-ANSYS-1-1433818441," Ansys academic research optics..
- [8] *ASAP Optical Software User Manual*..
- [9] E. Delano, "First-Order Design and the $y\bar{y}$ Diagram," *Applied Optics*, vol. 2, no. 12, pp. 1251-1256, (1963).
- [10] T. C. Poon and J. P. Liu, "Modern Digital Holography with MATLAB," Cambridge University press, (2014).
- [11] G. Nehmetallah, R. Aylo and L. Williams, *Analog and Digital Holography with MATLAB*, Washington : SPIE, Bellingham,, (2015).

- [12] D. Voelz, *Computational Fourier Optics a MATLAB Tutorial*, Washington: SPIE press, Bellingham, (2011).
- [13] J. Arnaud, , "Representation of Gaussian beam by complex Rays," *Applied Optics*, vol. 24, no. 4, pp. 538-543, (1985).
- [14] A. W. Greynolds, "Fat Rays Revisited: A Synthesis of Physical and Geometrical Optics with GauBlets," in *International optical design conference*,, (2014).
- [15] J. E. Harvey, R. G. Irvin and R. N. Pfisterer, "Modeling physical Optics Phenomena by Complex Ray Tracing,," *Optical Engineering*, vol. 54, no. 3, pp. 035-105, (2015).
- [16] S. A. Miller, J. Pond and B. Michel , "Retracing Meets Maxwell's Equations: Integrating Micro- and Macro-optical design," in *German International conference Photonik*, (2005).
- [17] N. G. Worku, "Decomposition of a Field with Smooth Wavefront into a Set of Gaussian beams with Non-zero Curvatures," *The Optical Society of America*, vol. 35, no. 7, pp. 1091-1102, (2018).
- [18] N. G. Worku and H. Gross, "Propagation of Truncated Gaussian Beams and Their Application in Modeling Sharp-edge Diffraction," vol. 36, no. 5, pp. 859-868.
- [19] N. G. Worku and H. Gross, "Gaussian Pulsed Beam Decomposition for Propagation of Ultrashort Pluses Through Optical System," vol. 37, no. 1, pp. 98-107, (2020).
- [20] R. Herloski, S. Marshall and R. Antos, "'Gaussian beam ray-equivalent modeling and optical design," *Applied Optics*, vol. 22, p. 1168–1174, (1983).
- [21] P. D. Colbourne, "Generally astigmatic Gaussian beam representation and optimization using skew rays," *Classical Optics, OSA Tech. Digest, Optica Publishing Group*,, p. IW3A.4, (2014)..

- [22] H. Kogelnik,, "On the propagation of Gaussian beams of light through lenslike media including those with a loss or gain variation," *Applied Optics*, vol. 4, p. 1562–1569, (1965).
- [23] J. Arnaud, "Representation of Gaussian beams by complex rays," *Applied Optics*, vol. 24, p. 538–543, (1985).
- [24] D. Kessler and R. V. Shack, "ȳ Diagram, a powerful optical design method for laser systems," *Applied Optics*., pp. 2692-2707, .(1992).
- [25] J. G. Pohly , L. E. Christensen and K. Mansour,, "Orion LAM Laser Absorption Spectrometer for Human Spaceflight – Flight Unit Build and Test Results," *ICES*, pp. 2020-360.
- [26] C. Matty and *et al.*, "Tunable Laser Adsorption Absorption Spectroscopy for Human Spaceflight," *ICES*-, pp. 2019-358, (2019).
- [27] D. C. Scott , R. L. Herman, C. R. Webster and R. D. Ma, "Airborne laser infrared absorption spectrometer (ALIAS-II) for in situ atmospheric measurements of N2O, CH4, CO, HCL and NO2 from balloon or remotely piloted aircraf," *Applied Optics*, vol. 38, no. 21, pp. 4609-4622, (1999).
- [28] i. Esquivias and *et al.*, "Evaluation of the Radiation Hardness of GaSb-based Laser Diodes for Space Applications," *IEEE RADECS Proceedings*, (2011).
- [29] p. Werle and F. Slemr, "Signal-to-noise Ratio Analysis in Laser Absorption Spectrometers using Optical Multiphases Cells," *Applied Optics*, vol. 30, no. 4, pp. 430-434, (1991).
- [30] A. E. Siegman, SIEGMAN Lasers, California: University Science Books Sausalito, (1986)..

- [31] P. W. Milonni and J. H. Eberly, *Laser Physics Book*, New Jersey : Wiley, Hoboken, (2010).
- [32] M. J. Mouroulis,, *Geometrical Optics and Optical Design*, New York: Oxford University press, Oxford, (1997).
- [33] F. L. Pedrotti and . L. S. Pedrotti, *Introduction to Optics*, 4th ed., New Jersey: Prentice Hall, Englewood Cliffs, (1993).
- [34] B. E. A. Saleh and M. C. Teich, *Fundamentals of Photonics*” 2ed Edition, NY: Wiley – Inter-science,, (1991)..
- [35] J. W. Goodman, *Introduction to Fourier Optics*,4th ed, New York : W.H. Freeman and company, (2017).
- [36] C. S. Williams, *Introduction to the Optical Transfer Function*, Bellingham, Washington: USA: SPIE, (2002).
- [37] A. Sennaroglu and J. G. Fujimoto,, "Design Criteria for Herriott-type multi-pass Cavities for Ultrashort Pulse Lasers," *Optics Express*, vol. 11, pp. 1106-1113, (2003).
- [38] K. A. Menard, "Simple Multi-Lens Intracavity Gaussian Laser Beam Simulation using Complex Rays," *Optical Engineering*, vol. 62, no. 8, p. 085104, (2023).
- [39] R. Alsalamah and P. J. Reardon, "Simplified Physical Model of Interferometric Radius of Curvature Test using yybar Diagram," *Optical Engineering*, vol. 58, no. 9, p. 095104, (2019).
- [40] H. Gross, F. Blechinger and B. Achnert,, *Handbook of optical systems*, vol. 4, Survey of Optical Instruments (Wiley), (2008)..
- [41] J. M. Geary, *Optical Testing*, Virginia: Willmann Bell, Inc., (2012)..

Appendix A.

Chapter 3 MATLAB simulation code for Figure 3.2.1 Column (a) normalized 3D irradiance at $Z=0$ showing ripples and roll off slope, column (b) normalized field magnitude cross section at $Z=0$.

% 2 D Gaussian Beam circles apertures OF=2 at Z=0

```
clear all; close all; clc;

lambda=0.5*10^-6;           %wavelength in m
k=2*pi/lambda;             %wavenumber
d0=0;
d1=0;                       %propagation distance(Z=0)
w0=0.0018181818;          % beam waist (9.09090909*10^-4& 0.00136363636& 0.0018181818)
L1=0.025;                  %source and observation plane side length
M=250;
dx1=L1/M;
x1=-L1/2:dx1:L1/2-dx1;
y1=x1;
[X1,Y1]=meshgrid(x1,y1);

%Initial y-ybar calculations for one beamlet

Lg=lambda/pi;              %Lagrange invariant
y0=w0;                     %Initial y value & initial waist w0
y0bar=0;                   %initial ybar value
w_beamlet=sqrt(y0^2+y0bar^2); % waist initial value
u0bar=Lg/y0;
u0=0;
theta=Lg/w0

%beamlet propagation after d1

y1bar=(d1*Lg)/y0;          %y*ubar-ybar*u=lambda/pi=Lg
y11=w0;                    %w^2=sqrt(y^2+ybar^2) & sqrt(w1^2-y1bar^2);
u1bar=(y1bar-y0bar)/d1;
zr=pi*w0^2/lambda;         %Rayleigh range
w1=sqrt(y1bar^2+y11^2);     %new waist w^2=w0^2*(1+(z/zr)^2)
w2=-w1;
u1=(y11-y0)/d1;
R1=(y11^2+y1bar^2)/(y11*u1+y1bar*u1bar); %Beam radius R=(y^2+ybar^2)/(yu+ybar.ubar)
Z=(y11*u1+y1bar*u1bar)/(u1bar^2+u1^2)

%composition

G=((w0/w)*exp(1i*k*d0)*exp(-1i*atan(d0/zr)))*...
(exp(-1*((X1-0).^2+(Y1-0).^2)/w0^2))...
```

```

+exp(-1*((X1-0).^2+(Y1-0.001818182).^2)/w0^2)...
+exp(-1*((X1-0).^2+(Y1+0.001818182).^2)/w0^2)...
+exp(-1*((X1-0).^2+(Y1-0.003636364).^2)/w0^2)...
+exp(-1*((X1-0).^2+(Y1+0.003636364).^2)/w0^2)...
+exp(-1*((X1-0).^2+(Y1-0.005454545).^2)/w0^2)...
+exp(-1*((X1-0).^2+(Y1+0.005454545).^2)/w0^2)...
+exp(-1*((X1-0).^2+(Y1-0.007272727).^2)/w0^2)...
+exp(-1*((X1-0).^2+(Y1+0.007272727).^2)/w0^2)...
+exp(-1*((X1-0).^2+(Y1-0.009090909).^2)/w0^2)...
+exp(-1*((X1-0).^2+(Y1+0.009090909).^2)/w0^2)...
+exp(-1*((X1-0.001818182).^2+(Y1+0).^2)/w0^2)...
+exp(-1*((X1+0.001818182).^2+(Y1+0).^2)/w0^2)...
+exp(-1*((X1-0.003636364).^2+(Y1+0).^2)/w0^2)...
+exp(-1*((X1+0.003636364).^2+(Y1+0).^2)/w0^2)...
+exp(-1*((X1-0.005454545).^2+(Y1+0).^2)/w0^2)...
+exp(-1*((X1+0.005454545).^2+(Y1+0).^2)/w0^2)...
+exp(-1*((X1-0.007272727).^2+(Y1+0).^2)/w0^2)...
+exp(-1*((X1+0.007272727).^2+(Y1+0).^2)/w0^2)...

```

```

I1=abs(G).^2; % Absolute irradiance
figure(1);
imagesc(x1,y1,I1); %Display absolute irradiance
axis square; axis xy;
xlabel('x (m) '); ylabel('y (m) ');
title(['d1=',num2str(d1),'m']);
colormap('jet');colorbar;
figure(2) %Irradiance profile
plot(x1,I1(M/2+1,:));
xlabel('x (m)'); ylabel('Irradiance');
title(['d1=',num2str(d1),'m']);
figure(3) %Plot absolute field magnitude
plot(x1,abs(G(M/2+1,:)));
xlabel('x (m)'); ylabel('Magnitude');
title(['d1=',num2str(d1),'m']);
figure(4) %Plot absolute field phase
plot(x1,unwrap(angle(G(M/2+1,:))));
xlabel('x (m)'); ylabel('phase (rad)');
title(['d1=',num2str(d1),'m']);
figure(5)
mesh(x1,y1,I1);
axis square; axis xy;
title('11X11 beamlets array & 2.00 Overlap Factor')
colormap('jet') ;
colorbar;

```

Chapter 3 MATLAB simulation code for Figure 3.2.1 Column (c) $1/e^2$ map radii of 11x11

beamlets.

% 2 D Gaussian Beam circles apertures OF=1

```
figure(1);
viscircles([0 0],9.09090909*10^-4,'Color','black')
viscircles([0,-0.001818182],9.09090909*10^-4,'Color','black')
viscircles([0,0.001818182],9.09090909*10^-4,'Color','black')
viscircles([0,-0.003636364],9.09090909*10^-4,'Color','black')
viscircles([0,0.003636364],9.09090909*10^-4,'Color','black')
viscircles([0,-0.005454545],9.09090909*10^-4,'Color','black')
viscircles([0,0.005454545],9.09090909*10^-4,'Color','black')
viscircles([0,-0.007272727],9.09090909*10^-4,'Color','black')
viscircles([0,0.007272727],9.09090909*10^-4,'Color','black')
viscircles([0,-0.0091],9.09090909*10^-4,'Color','black')
viscircles([0,0.0091],9.09090909*10^-4,'Color','black')
viscircles([-0.001818182,0],9.09090909*10^-4,'Color','black')
viscircles([0.001818182,0],9.09090909*10^-4,'Color','black')
viscircles([-0.003636364,0],9.09090909*10^-4,'Color','black')
viscircles([0.003636364,0],9.09090909*10^-4,'Color','black')
viscircles([-0.005454545,0],9.09090909*10^-4,'Color','black')
viscircles([0.005454545,0],9.09090909*10^-4,'Color','black')
viscircles([-0.007272727,0],9.09090909*10^-4,'Color','black')
viscircles([0.007272727,0],9.09090909*10^-4,'Color','black')
viscircles([-0.0091,0],9.09090909*10^-4,'Color','black')
viscircles([0.0091,0],9.09090909*10^-4,'Color','black')
xlabel('x (m)', 'fontsize', 12, 'fontweight', 'bold'); ylabel('y (m)', 'fontsize', 12, 'fontweight', 'bold');
title('2D Overlap factor=1.00', 'fontsize', 12, 'fontweight', 'bold');
```

Appendix B.

Chapter 4 MATLAB simulation code for Section 4.1, GBD and Eq.4.3

```
clear all; close all; clc;
```

```
lambda=0.5*10^-6;           % Wavelength in (m)
k=2*pi/lambda;             % Wavenumber
d1=2000;                   % Propagation distance
w0=0.001;                 % Beam waist=1mm or 0.0013 for overlap factor 1,1.5, or 2
L1=0.5;                   % source and observation plane side length
M=250;
dx1=L1/M;
x1=-L1/2:dx1:L1/2-dx1;
y1=x1;
[X1,Y1]=meshgrid(x1,y1);
L2=lambda*d1/dx1;
dx2=lambda*d1/L1;
x2=-L2/2:dx2:L2/2-dx2;
y2=x2;
[X2,Y2]=meshgrid(x2,y2);
L3=2*0.5;
```

```
%Initial y-ybar calculations for one beamlet
```

```
Lg=lambda/pi;             % Lagrange invariant
y0=w0;                   % Initial y value & initial waist w0
y0bar=0;                 % Initial ybar value
w_beamlet=sqrt(y0^2+y0bar^2); % waist initial value
u0bar=Lg/y0;
u0=0;
theta=Lg/w0
```

```
%Beamlet propagation after d1
```

```
y1bar=(d1*Lg)/y0;        % y*ubar-ybar*u=lambda/pi=Lg
y11=w0;                  % w^2=sqrt(y^2+ybar^2)&sqrt(w1^2-y1bar^2)
u1bar=(y1bar-y0bar)/d1;
zr=pi*w0^2/lambda;      % Rayleigh range
w1=sqrt(y1bar^2+y11^2);  % new waist w^2=w0^2*(1+(z/zr)^2)
w2=-w1;
u1=(y11-y0)/d1;
R1=(y11^2+y1bar^2)/(y11*u1+y1bar*u1bar); % Beam radius R=(y^2+ybar^2)/(yu+ybar.ubar)
```

$$Z=(y11*u1+y1bar*u1bar)/(u1bar^2+u1^2)$$

%composition

```
ay=-7*0.00133:0.00133:7*0.00133;
```

```
ax=-7*0.00133:0.00133:7*0.00133;
```

```
G_sum=0;
```

```
G_vec=zeros(M,M);
```

```
for ii=1:length(ay)
```

```
    for jj=1:length(ax)
```

```
        G=((w0/w1) * exp(1i*k*d1)*exp(-1i*atan(d1/zr))).*...
```

```
        (exp(-1*((X2-ay(ii)).^2+(Y2-ax(jj)).^2)/(w1)^2).*exp(1i*k*((X2-ay(ii)).^2+(Y2-ax(jj)).^2)./(2*R1)));
```

```
        G_sum=G_sum+G;
```

```
        G_vec(:,j)=G_sum;
```

```
    end
```

```
end
```

```
I1=abs(G_vec).^2; %Absolute irradiance
```

```
figure(1)
```

```
imagesc(x2,y2,nthroot(I1,3)); %Display absolute irradiance & stretch image contrast
```

```
axis square; axis xy;
```

```
colormap('gray'); xlabel('x (m) '); ylabel('y (m)');
```

```
title(['d1=',num2str(d1),'m stretched contrast']);
```

```
colorbar;
```

```
figure(2)
```

```
imagesc(x2,y2,I1); %Display absolute irradiance
```

```
axis square; axis xy;
```

```
colormap('gray'); xlabel('x (m) '); ylabel('y (m)');
```

```
title(['d1=',num2str(d1),'m']);
```

```
colorbar;
```

%Plot irradiance profile

```
figure(3)
```

```
plot(x2,I1(M/2+1,:));
```

```
xlabel('x (m)'); ylabel('Irradiance');
```

```
title(['d1=',num2str(d1),'m']);
```

%Plot absolute field magnitude

```
figure(4)
```

```
plot(x2,abs(G_vec(M/2+1,:)));
```

```
xlabel('x (m)'); ylabel('Magnitude');
```

```
title(['d1=',num2str(d1),'m']);
```

%plot absolute field phase

```

figure(5)
plot(x2,unwrap(angle(G_vec(M/2+1,:))));
xlabel('x (m)'); ylabel('phase (rad)');
title(['d1=',num2str(d1),'m']);

```

```

figure(6)
mesh(X2,Y2,I1);
xlabel('x1');
ylabel('Intensity');
grid on; colorbar;

```

%Section 4.2, HGBD

```

clear all; close all; clc;
B=21.25/20;
lambda=0.5*10^-6; %Wavelength in (m)
k=2*pi/lambda; %Wavenumber
d1=50; %Propagation distance (50&2000)
w0=0.0021428571;
w00=0.00125;
w000=0.00190;
L1=0.08; %For 50 (m) L1=0.08, for 2000 L1=0.5;
M=250;
dx1=L1/M;
x1=-L1/2:dx1:L1/2-dx1;
y1=x1;
[X1,Y1]=meshgrid(x1,y1);
L2=lambda*d1/dx1;
dx2=lambda*d1/L1;

x2=-L2/2:dx2:L2/2-dx2;
y2=x2;
[X2,Y2]=meshgrid(x2,y2);

%Initial y-ybar calculations for one beamlet

Lg=lambda/pi; %Lagrange invariant
y0=w0; %Initial y value & initial waist w0
y00=w00;
y000=w000;
y0bar=0; %Initial ybar value
y00bar=0;
y000bar=0;
u0bar=Lg/y0;
u00bar=Lg/y00;
u000bar=Lg/y000;
u0=0;
u00=0;
u000=0;
theta=Lg/w0
theta_00=Lg/w00

```

theta_000=Lg/w000

%Beamlet propagation after d1 (m)

```
y1bar=(d1*Lg)/y0; %y*ubar-ybar*u=lambda/pi=Lg
y1bar_00=(d1*Lg)/y00;
y1bar_000=(d1*Lg)/y000;
y11=w0; %w^2=sqrt(y^2+ybar^2) & sqrt(w1^2-y1bar^2);
y11_00=w00;
y11_000=w000;
u1bar=(y1bar-y0bar)/d1;
u1bar_00=(y1bar_00-y00bar)/d1;
u1bar_000=(y1bar_000-y000bar)/d1;
zr=pi*w0^2/lambda; %Rayleigh range
zr_00=pi*w00^2/lambda;
zr_000=pi*w000^2/lambda;
w1=sqrt(y1bar^2+y11^2); %New waist w^2=w0^2*(1+(z/zr)^2)
w1_00=sqrt(y1bar_00^2+y11_00^2);
w1_000=sqrt(y1bar_000^2+y11_000^2);
u1=(y11-y0)/d1;
u1_00=(y11_00-y00)/d1;
u1_000=(y11_000-y000)/d1;
R1=(y11^2+y1bar^2)/(y11*u1+y1bar*u1bar); %Beam radius R=(y^2+ybar^2)/(yu+ybar.ubar)
R1_00=(y11_00^2+y1bar_00^2)/(y11_00*u1_00+y1bar_00*u1bar_00);
R1_000=(y11_000^2+y1bar_000^2)/(y11_000*u1_000+y1bar_000*u1bar_000);
z_00=(y11_00*u1_00+y1bar_00*u1bar_00)/(u1bar_00^2+u1_00^2)
z_000=(y11_000*u1_000+y1bar_000*u1bar_000)/(u1bar_000^2+u1_000^2)
A=((w0/w1)*exp(1i*k*d1)*exp(-1i*atan(d1/zr)));
A_00=((w00/w1_00)*exp(1i*k*d1)*exp(-1i*atan(d1/zr_00)));
A_000=((w000/w1_000)*exp(1i*k*d1)*exp(-1i*atan(d1/zr_000)));
```

%Composition

```
G= (A).*(exp(-1*((X2-0).^2+(Y2-0).^2)/(w1^2)).*exp(1i*k*((X2-0).^2+(Y2-0).^2)/(2*R1)))+...
+(A).*(exp(-1*((X2-0.0021428*B).^2+(Y2+0).^2)/(w1^2)).*exp(1i*k*((X2-0.0021428*B).^2+(Y2-0).^2)/(2*R1)))+...
+(A).*(exp(-1*((X2+0.0021428*B).^2+(Y2+0).^2)/(w1^2)).*exp(1i*k*((X2+0.0021428*B).^2+(Y2-0).^2)/(2*R1)))+...
+(A).*(exp(-1*((X2-0.00428*B).^2+(Y2+0).^2)/(w1^2)).*exp(1i*k*((X2-0.00428*B).^2+(Y2-0).^2)/(2*R1)))+...
+(A).*(exp(-1*((X2+0.00428*B).^2+(Y2+0).^2)/(w1^2)).*exp(1i*k*((X2+0.00428*B).^2+(Y2-0).^2)/(2*R1)))+...
+(A).*(exp(-1*((X2-0.006428*B).^2+(Y2+0).^2)/(w1^2)).*exp(1i*k*((X2-0.006428*B).^2+(Y2-0).^2)/(2*R1)))+...
+(A).*(exp(-1*((X2+0.006428*B).^2+(Y2+0).^2)/(w1^2)).*exp(1i*k*((X2+0.006428*B).^2+(Y2-0).^2)/(2*R1)))+...
+(A_00*0.25).*(exp(-1*((X2-0.0073*B).^2+(Y2+0).^2)/(w1_00^2)).*exp(1i*k*((X2-0.0073*B).^2+(Y2-0).^2)/(2*R1_00)))+...
```

```

+(A_00*0.25).*(exp(-
1*((X2+0.0073*B).^2+(Y2+0).^2)/(w1_00^2)).*exp(1i*k*((X2+0.0073*B).^2+(Y2-
0).^2)/(2*R1_00)))...
+(A_00).*(exp(-1*((X2-0.00855*B).^2+(Y2+0).^2)/(w1_00^2)).*exp(1i*k*((X2-
0.00855*B).^2+(Y2-0).^2)/(2*R1_00)))...
+(A_00).*(exp(-
1*((X2+0.00855*B).^2+(Y2+0).^2)/(w1_00^2)).*exp(1i*k*((X2+0.00855*B).^2+(Y2-
0).^2)/(2*R1_00)))...
+(A_000*0.19).*(exp(-1*((X2-0.00672*B).^2+(Y2+0).^2)/(w1_000^2)).*exp(1i*k*((X2-
0.00672*B).^2+(Y2-0).^2)/(2*R1_000)))...
+(A_000*0.19).*(exp(-
1*((X2+0.00672*B).^2+(Y2+0).^2)/(w1_000^2)).*exp(1i*k*((X2+0.00672*B).^2+(Y2-
0).^2)/(2*R1_000)))...
+(A).*(exp(-1*((X2+0).^2+(Y2-0.0021428*B).^2)/(w1^2)).*exp(1i*k*((X2-0).^2+(Y2-
0.0021428*B).^2)/(2*R1)))...%

```

```

I1=abs(G).^2; % Absolute irradiance
figure(1)
imagesc(x2,y2,nthroot(I1,3)); %Display absolute irradiance & stretch image
contrast axis square; axis xy;
colormap('gray'); xlabel('x (m) '); ylabel('y (m)');
title(['d1=',num2str(d1),'m stretched contrast']);
colorbar;
figure(2)
imagesc(x2,y2,I1); %Display absolute irradiance
axis square; axis xy;
colormap('gray'); xlabel('x (m) '); ylabel('y (m)');
title(['d1=',num2str(d1),'m']);
colorbar;

```

%Irradiance profile

```

figure(3)
plot(x2,I1(M/2+1,:));
xlabel('x (m)'); ylabel('Irradiance');
title(['d1=',num2str(d1),'m']);

```

%Plot absolute field magnitude

```

figure(4)
plot(x2,abs(G(M/2+1,:)));
xlabel('x (m)'); ylabel('Magnitude');
title(['d1=',num2str(d1),'m']);

```

%Plot absolute field phase

```

figure(5)
plot(x2,unwrap(angle(G(M/2+1,:))));
xlabel('x (m)'); ylabel('phase (rad)');
title(['d1=',num2str(d1),'m']);
figure(6)
mesh(X2,Y2,I1);
xlabel('x2');
ylabel('Intensity');

```

Appendix C.

Chapter 5 Programmed Excel file for HCMPC Design Approach 32 Intercepts.

The screenshot displays an Excel spreadsheet with the following structure and data:

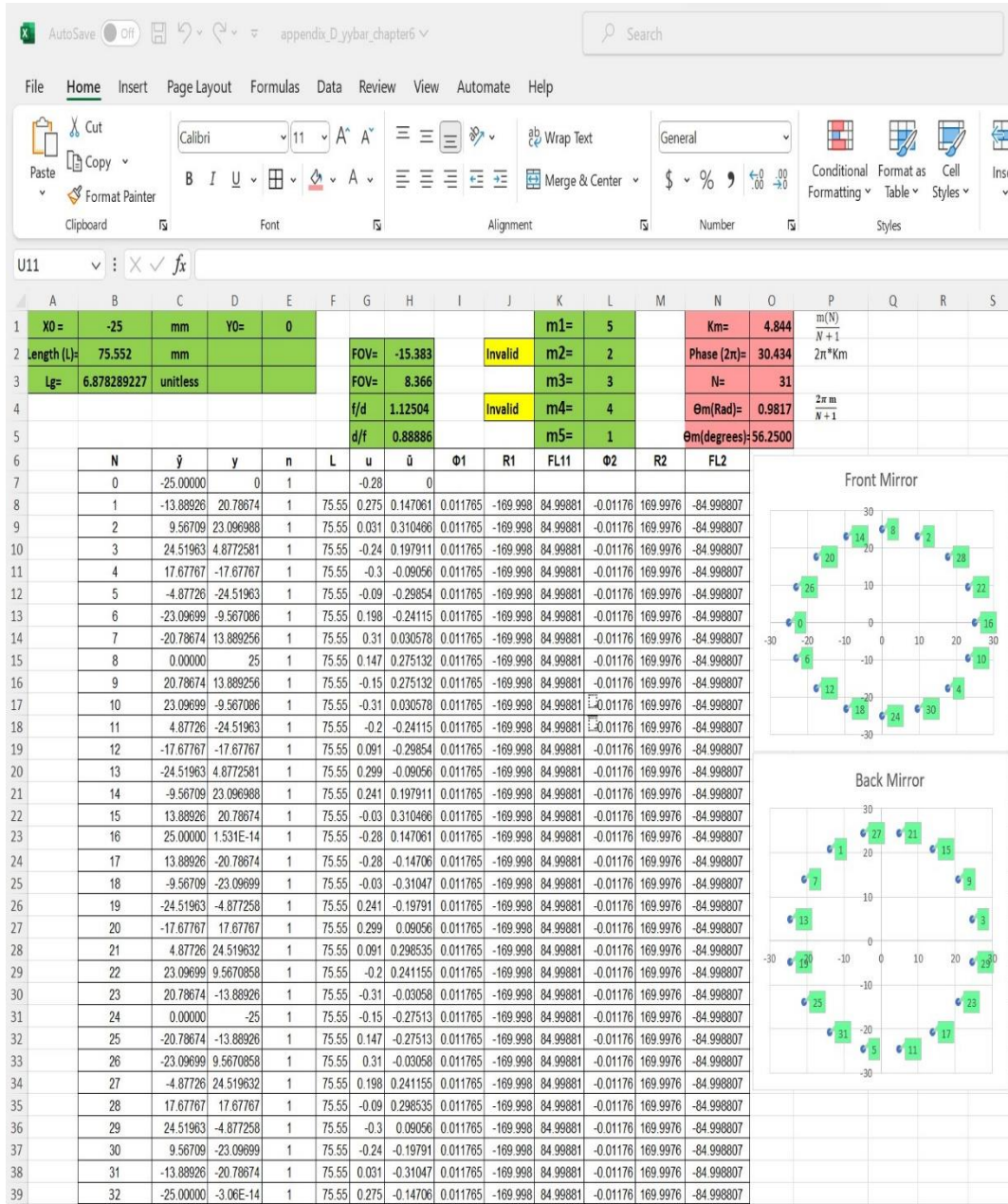
	A	B	C	D	E	F	G	H	I	J	K	L
1			Formulas	Notes	Zemax Notes				Formulas	Notes	Zemax Notes	
3	Raduis:	169.9982891		mm			Raduis:	170.0022		mm		
4	Length:	75.5523		mm			Length:	75.5523		mm		
5	Gparam:	0.555570233	G=1-L/R	no units			Gparam:	0.555580457	G=1-L/R	no units		
6	theta(rad)=	0.981747704	COSθ=1-L/2f=1-L/R	Radian			theta(rad)=	0.981735408	COSθ=1-L/2f=1-L/R	Radian		
7	theta(deg)=	56.25		Degrees			theta(deg)=	56.24929546		Degrees		
8	Xo:	-10.414	initial x coordinates	mm	Decenter X Coordinate		Xo:	10.414	initial x coordinates	mm	Decenter X Coordinate	
9	Yo:	0		mm			Yo:	0		mm		
10	Term1	0.534511136	SQRT(L/4f-L)	mm			Term1	0.534503231	SQRT(L/4f-L)	mm		
11	Xaimed	-5.785708407	X'=XCOS(θ)-YOSIN(θ)	Rotation matrix								
12	Yaimed	-8.658924543	Y'=XOSIN(θ)+YOCOS(θ)	Rotation matrix								
13	Xslope=	0.06125944	Radian		3.509907371		Xslope=	-3.5098266				
14	Yslope=	-0.114608351	Radian		-6.566574828		Yslope=	0				
15	Xn=		XOCosθ+SQRT(L/4f-L)(XO+2fXo')Sinnθ									
16												
17			v(odd)	xn	yn							
18			1	-5.785708407	-8.658924543							
19			3	10.21389791	-2.031670613							
20			5	-2.031670613	10.21389791							
21			7	-8.658924543	-5.785708407							
22			9	8.658924543	-5.785708407							
23			11	2.031670613	10.21389791							
24			13	-10.21389791	-2.031670613							
25			15	5.785708407	-8.658924543							
26			17	5.785708407	8.658924543							
27			19	-10.21389791	2.031670613							
28			21	2.031670613	-10.21389791							
29			23	8.658924543	5.785708407							
30			25	-8.658924543	5.785708407							
31			27	-2.031670613	-10.21389791							
32			29	10.21389791	2.031670613							
33			31	-5.785708407	8.658924543							
34			33	-5.785708407	-8.658924543							
35			35	10.21389791	-2.031670613							
36			37	-2.031670613	10.21389791							
37			39	-8.658924543	-5.785708407							
38			43	2.031670613	10.21389791							
39			45	-10.21389791	-2.031670613							
40			47	5.785708407	-8.658924543							
41												
42												
43												
44												
45												
46												
47												
48												
49												
50												

	v(even)	xn	yn
	0	-10.414	0
	2	3.985265265	-9.621281452
	4	7.363810019	7.363810019
	6	-9.621281452	3.985265265
	8	-2.26381E-14	-10.414
	10	9.621281452	3.985265265
	12	-7.363810019	7.363810019
	14	-3.985265265	-9.621281452
	16	10.414	-4.33773E-14
	18	-3.985265265	9.621281452
	20	-7.363810019	-7.363810019
	22	9.621281452	-3.985265265
	24	6.60154E-14	10.414
	26	-9.621281452	-3.985265265
	28	7.363810019	-7.363810019
	30	3.985265265	9.621281452
	32	-10.414	8.67546E-14
	34	3.985265265	-9.621281452
	36	7.363810019	7.363810019
	38	-9.621281452	3.985265265
	40	-7.23948E-14	-10.414
	42	9.621281452	3.985265265
	46	-3.985265265	-9.621281452
	48	10.414	-1.30132E-13

2vθ=2μm & m=5	v=	16
	θ=	0.981748
	COS(θ)	0.55557
	d=	75.5523
	R=	169.9983

Appendix D.

Chapter 6 Programmed Excel file for $y\bar{y}$ diagram gut ray design of MPC.



Chapter 6 Programmed Excel file for $y\bar{y}$ diagram collimated ray design of MPC.

AutoSave Off appendix_D_yybar_chapter6_collimated Search

File Home Insert Page Layout Formulas Data Review View Automate Help

Clipboard Font Alignment Number

P51

	A	B	C	D	E	F	G	H	I	J	K	L	M	N	O
1	X0=	25	mm	Y0=	0					m1=	5	Km=	2.906		
2	Length (L)=	75.552	mm				FOV=	0	Invalid	m2=	2	Phase (2π)=	18.261		
3	Lg=	4.5959259	unitless				FOV=	10.8745592		m3=	3	N=	31		
4	EPD=	47.847017					f/L	2.96662401	Invalid	m4=	4	θm(Rad)=	0.5890		
5							L/f	0.33706078		m5=	1	θm(degrees)=	33.75		
6		N	\bar{y}	y	n	L	u	\bar{u}	$\Phi 1$	EFL	RoC				
7		0	-7.25712	23.92351	1.000	75.552	0.000000	0.192109							
8		1	7.25712	23.92351	1.000	75.552	-0.107	0.159733	0.004461	224.14949	448.299				
9		2	19.32526	15.85983	1.000	75.552	-0.177	0.073517	0.004461	224.14949	448.299				
10		3	24.87962	2.45043	1.000	75.552	-0.188	-0.037479	0.004461	224.14949	448.299				
11		4	22.04803	-11.78492	1.000	75.552	-0.136	-0.135842	0.004461	224.14949	448.299				
12		5	11.78492	-22.04803	1.000	75.552	-0.037	-0.188418	0.004461	224.14949	448.299				
13		6	-2.45043	-24.87962	1.000	75.552	0.074	-0.177486	0.004461	224.14949	448.299				
14		7	-15.85983	-19.32526	1.000	75.552	0.160	-0.106730	0.004461	224.14949	448.299				
15		8	-23.92351	-7.25712	1.000	75.552	0.192	0.000000	0.004461	224.14949	448.299				
16		9	-23.92351	7.25712	1.000	75.552	0.160	0.106730	0.004461	224.14949	448.299				
17		10	-15.85983	19.32526	1.000	75.552	0.074	0.177486	0.004461	224.14949	448.299				
18		11	-2.45043	24.87962	1.000	75.552	-0.037	0.188418	0.004461	224.14949	448.299				
19		12	11.78492	22.04803	1.000	75.552	-0.136	0.135842	0.004461	224.14949	448.299				
20		13	22.04803	11.78492	1.000	75.552	-0.188	0.037479	0.004461	224.14949	448.299				
21		14	24.87962	-2.45043	1.000	75.552	-0.177	-0.073517	0.004461	224.14949	448.299				
22		15	19.32526	-15.85983	1.000	75.552	-0.107	-0.159733	0.004461	224.14949	448.299				
23		16	7.25712	-23.92351	1.000	75.552	0.000	-0.192109	0.004461	224.14949	448.299				
24		17	-7.25712	-23.92351	1.000	75.552	0.107	-0.159733	0.004461	224.14949	448.299				
25		18	-19.32526	-15.85983	1.000	75.552	0.177	-0.073517	0.004461	224.14949	448.299				
26		19	-24.87962	-2.45043	1.000	75.552	0.188	0.037479	0.004461	224.14949	448.299				
27		20	-22.04803	11.78492	1.000	75.552	0.136	0.135842	0.004461	224.14949	448.299				
28		21	-11.78492	22.04803	1.000	75.552	0.037	0.188418	0.004461	224.14949	448.299				
29		22	2.45043	24.87962	1.000	75.552	-0.074	0.177486	0.004461	224.14949	448.299				
30		23	15.85983	19.32526	1.000	75.552	-0.160	0.106730	0.004461	224.14949	448.299				
31		24	23.92351	7.25712	1.000	75.552	-0.192	0.000000	0.004461	224.14949	448.299				
32		25	23.92351	-7.25712	1.000	75.552	-0.160	-0.106730	0.004461	224.14949	448.299				
33		26	15.85983	-19.32526	1.000	75.552	-0.074	-0.177486	0.004461	224.14949	448.299				
34		27	2.45043	-24.87962	1.000	75.552	0.037	-0.188418	0.004461	224.14949	448.299				
35		28	-11.78492	-22.04803	1.000	75.552	0.136	-0.135842	0.004461	224.14949	448.299				
36		29	-22.04803	-11.78492	1.000	75.552	0.188	-0.037479	0.004461	224.14949	448.299				
37		30	-24.87962	2.45043	1.000	75.552	0.177	0.073517	0.004461	224.14949	448.299				
38		31	-19.32526	15.85983	1.000	75.552	0.107	0.159733	0.004461	224.14949	448.299				

Front Mirror (M1)

Back Mirrors (M2)

Chapter 6 Programmed Excel file for $\bar{y}\bar{y}$ diagram different radii of curvatures MPC.

AutoSave Off appendix_D_chapter6_two_radii Search

File Home Insert Page Layout Formulas Data Review View Automate Help

Clipboard: Paste, Cut, Copy, Format Painter

Font: Calibri, 11, Bold, Italic, Underline, Paragraph, Font Color, Text Color

Alignment: Merge & Center, Text Alignment, Orientation

Number: General, Currency, Percentage, Decimals

V44

	A	B	C	D	E	F	G	H	I	J	K	L	M	N	O	P
1	r01=	25	mm	r02=	7.58	FOV=	11.490444		m1=	5	Km=	4.844				
2	length (L)	75.552	mm			FOV=	-11.49406	Invalid	m2=	2	Phase (2 π)=	30.434				
3	Lg=	2.0855	unitless			g1	1.8323556		m3=	3	N=	31				
4						g2	0.1684489	Invalid	m4=	4	Θ m(Rad)=	0.9817				
5						Stability	0.3086583		m5=	1	Θ m(degrees)=	56.2500				
6		N	\bar{y}	y	n	L	\bar{u}	u	Φ 1	EFL	ROC					
7		0	-11.7849	22.048	1.000	75.552	0.203	-0.203								
8		1	3.57319	6.68496	1.000	75.552	0.282	-0.056	-0.02203	-45.384	-90.7688919	R1				
9		2	24.8796	2.45043	1.000	75.552	-0.266	-0.110	0.02201	45.428	90.85671285	R2				
10		3	4.8087	-5.85942	1.000	75.552	-0.160	-0.239	-0.02203	-45.384	-90.7688919					
11		4	-7.25712	-23.9235	1.000	75.552	0.000	0.288	0.02201	45.428	90.85671285					
12		5	-7.25361	-2.20036	1.000	75.552	-0.160	0.239	-0.02203	-45.384	-90.7688919					
13		6	-19.3253	15.8598	1.000	75.552	0.266	-0.110	0.02201	45.428	90.85671285					
14		7	0.74297	7.5435	1.000	75.552	0.282	0.056	-0.02203	-45.384	-90.7688919					
15		8	22.048	11.7849	1.000	75.552	-0.203	-0.203	0.02201	45.428						
16		9	6.68496	-3.57319	1.000	75.552	-0.056	-0.282	-0.02203	-45.384						
17		10	2.45043	-24.8796	1.000	75.552	-0.110	0.266	0.02201	45.428						
18		11	-5.85942	-4.8087	1.000	75.552	-0.239	0.160	-0.02203	-45.384						
19		12	-23.9235	7.25712	1.000	75.552	0.288	0.000	0.02201	45.428						
20		13	-2.20036	7.25361	1.000	75.552	0.239	0.160	-0.02203	-45.384						
21		14	15.8598	19.3253	1.000	75.552	-0.110	-0.266	0.02201	45.428						
22		15	7.5435	-0.74297	1.000	75.552	0.056	-0.282	-0.02203	-45.384						
23		16	11.7849	-22.048	1.000	75.552	-0.203	0.203	0.02201	45.428						
24		17	-3.57319	-6.68496	1.000	75.552	-0.282	0.056	-0.02203	-45.384						
25		18	-24.8796	-2.45043	1.000	75.552	0.266	0.110	0.02201	45.428						
26		19	-4.8087	5.85942	1.000	75.552	0.160	0.239	-0.02203	-45.384						
27		20	7.25712	23.9235	1.000	75.552	0.000	-0.288	0.02201	45.428						
28		21	7.25361	-2.20036	1.000	75.552	0.160	-0.239	-0.02203	-45.384						
29		22	19.3253	-15.8598	1.000	75.552	-0.266	0.110	0.02201	45.428						
30		23	-0.74297	-7.5435	1.000	75.552	-0.282	-0.056	-0.02203	-45.384						
31		24	-22.048	-11.7849	1.000	75.552	0.203	0.203	0.02201	45.428						
32		25	-6.68496	3.57319	1.000	75.552	0.056	0.282	-0.02203	-45.384						
33		26	-2.45043	24.8796	1.000	75.552	0.110	-0.266	0.02201	45.428						
34		27	5.85942	4.8087	1.000	75.552	0.239	-0.160	-0.02203	-45.384						
35		28	23.9235	-7.25712	1.000	75.552	-0.288	0.000	0.02201	45.428						
36		29	2.20036	-7.25361	1.000	75.552	-0.239	-0.160	-0.02203	-45.384						
37		30	-15.8598	-19.3253	1.000	75.552	0.110	0.266	0.02201	45.428						
38		31	-7.5435	0.74297	1.000	75.552	-0.056	0.282	-0.02203	-45.384						

Front & Back $\bar{y}\bar{y}$

Appendix E.

Chapter 7 Programmed Excel file for Zernike's Coefficients Calculations.

The screenshot displays an Excel spreadsheet titled 'appendix_E_ABBERRATION'. The interface includes the standard Microsoft Office ribbon (File, Home, Insert, Page Layout, Formulas, Data, Review, View, Automate, Help) and a formula bar showing 'A150'. The spreadsheet is organized into several sections:

- Header Section (Rows 2-5):** Contains input parameters for Zernike coefficient calculations. Key values include:
 - SLOPE: -1.0708
 - SLOPE AM: 61.076
 - EPD: 1.1635
 - Scale Factor: 0.1088810
 - Angle between: 0.80747704 RAD
 - Angle between: 56.25 deg
- Main Data Table (Rows 6-32):** A large table with columns for Zernike modes (N, L, m) and their coefficients (C1 to C22). The table is populated with numerical values for each mode, representing the calculated Zernike coefficients.
- Comparison Graphs (Rows 6-32):** Two line graphs are positioned to the right of the main data table. Both graphs are titled 'Comparison Of Z Values' and plot 'Z' values against a mode index (1 to 32). The graphs compare 'Calculated Z' (blue line) and 'Z (Zernike)' (orange line), showing a strong correlation between the two data series.